Annual Report 2005

Address:	Prof. Dr. Burkard Hillebrands Fachbereich Physik Technische Universität Kaiserslautern Erwin-Schrödinger-Straße 56 67663 Kaiserslautern, Germany Tel.: +49-(0)631-205-4228 Fax.:+49-(0)631-205-4095
Postal address:	Postfach 3049 67653 Kaiserslautern, Germany
Internet:	http://www.physik.uni-kl.de/hillebrands/
E-Mail:	hilleb@physik.uni-kl.de

Our Group

From left to right:

Helmut Schultheiß, Andreas Beck, Markus Weber, Dieter Weller,
Dirk Hoffmann, Thomas Schneider, Steffen Blomeier,
Dr. Jaroslav Hamrle, Dr. Britta Leven, Sibylle Müller,
Christian Bayer, Patricia Martín Pimentel, Dr. Alexander Serga,
Dr. Galina Khlyap, Dr. Patrizio Candeloro, Hans Nembach,
Sebastian Hermsdörfer, Prof. Dr. Yasuo Ando (guest),
Prof. Dr. Gennadiy Melkov (guest), Prof. Dr. Andrei Slavin (guest),
Prof. Dr. Burkard Hillebrands

Contents

Chapter 1: Introduction

Dear Colleagues and Friends,

with this report we present our results obtained in the last 12 months, covering the period of November 2004 to October 2005.

Highlights of the last year were the space resolved study of the dynamics in small magnetic rings, progress in spin wave logic, all-optical techniques to study magnetization dynamics and switching, investigations on quasi-solitons in wide waveguides, and progress in magnetic patterning of exchange coupled systems using ion irradiation. We have pushed forward our experimental techniques, in particular in Brillouin light scattering spectroscopy. The micro-focus Brillouin light scattering setup enables us now to investigate dynamics over a very wide frequency range with a spatial resolution of 300 nm and with application of microwave signals using waveguide structures. A first success has been achieved in setting up a phase sensitive Brillouin light scattering spectrometer - now the amplitude and the phase of spin waves can be measured independently.

Again we had a very lively list of visitors and guests such as, among others, Prof. Boris Kalinikos (St. Petersburg, Russia), Prof. Gennadiy Melkov (Kiev, Ukraine), Prof. Andrei N. Slavin (Univ. of Rochester, Michigan, U.S.A.), and Prof. J. Darrell Comins (Johannesburg, South Africa).

Newly arrived in our group have two new postdocs, Jaroslav Hamrle and Patrizio Candeloro. After finishing his Ph.D. at the Université Paris Sud, Jaroslav has spend a postdoc year in Japan in the group of Prof. Yoshichika Otani in RIKEN/Wako. He will work on time resolved magneto-optic investigations and Brillouin light scattering. Patrizio arrived from Italy and received his education at the University in Perugia and at the synchrotron facility in Trieste. He works on finite size exchange bias systems funded through the EU network NEXBIAS. Vladislav Demidov has left our group and accepted a post-doc position in the group of Sergej Demokritov in Münster/Germany. Mikhail Kostylev has left as well to accept a prestigious stipend in Australia.

It was our special pleasure to have with us this year Prof. Yasuo Ando from the Tohoku University in Sendai, Japan. He spends a sabbatical in our lab, at the same time promoting a joint research project on new materials and functions for spin engineering, and also investigating the German academic system.

I myself had a very busy year, since I accepted to serve for the IEEE-Magnetics Society as a Distinguished Lecturer to promote magnetism and also the goals of the Society. I gave a total of 27 lectures in the reporting period in countries such as Great Britain, Japan, Poland, and the U.S.A., and a few more are to come.

Quite some of our work is embedded in the German priority program (“Schwerpunktprogramm”) entitled “Ultrafast magnetization processes”, and in the Research Unit (“Forschergruppe”) entitled “New materials with high spin polarization”, both funded by the Deutsche Forschungsgemeinschaft. As in the recent years we are largely engaged in international training through participation in three research training networks funded by the European Community. They are “Ultrafast Magnetization Processes in Advanced Devices” (ULTRASWITCH), “New Exchange Bias Systems for Advanced Magnetic Devices” (NEXBIAS), and “Ultrasmooth Magnetic Layers for Advanced Devices” (ULTRASMOOTH). In a research oriented European project we address ultrafast phenomena in magnetic logic.

Locally we acknowledge support by the state funded priority center “Materials for Micro and Nanosystems”, and, since last year, by the “Center for Nanostructure Technology and Molecular Biological Technology”, which is operated by our university providing the technology for patterning down to the deep submicron scale.

Our work would not have been possible without valuable collaborations with people all over the world. They are too many to list them here all. In particular we would like to thank, in alphabetical order, Yasuo Ando, Christian Back, Dima Berkow, Harry Bernas, John Chapman, Claude Chappert, Darrell Comins, Günter Dumpich, Hajo Elmers, Claudia Felser, Claude Fermon, Jacques Ferré, Paulo Freitas, Heinz Hilgers, Andreas Hütten, Gerhard Jakob, Boris Kalinikos, Mikhail Kostylev, Natalia Kreines, Norbert Laube, Wolfram Maaß, Jan Marien, Roland Mattheis, Andrezj Maziewski, Jacques Miltat, Alexandra Mougin, Fabrizio Nizzoli, Josep Nogues, Carl Patton, Günter Reiss, Konrad Samwer, John R. Sandercock, Gerd Schönhense, Andrei Slavin, Bob Stamps, André Thiaville and Stefan Visnovsky for their interactions with us and their strong input to our work. Collaborations within the Fachbereich Physik at the University of Kaiserslautern (Martin Aeschlimann, Sebastian Eggert, Michael Fleischhauer, Wolfgang Hübner, Volker Schünemann, Herbert Urbassek and their groups), the Institut für Oberflächen- und Schichtanalytik as well as the Nano+Bio Center have been very stimulating. I am especially grateful to Heinz Busch and Udo Grabowy and their start up company NTTF GmbH for the close contact. I am much obliged to Stefan Sattel and his team from the TZO GmbH for providing convenient general conditions for our work in Rheinbreitbach.

I would also like to thank all our sponsors, which are the Deutsche Forschungsgemeinschaft, the Bundesministerium für Bildung, und Forschung, the Humboldt Foundation, the Deutscher Akademischer Austauschdienst, the European Community, INTAS, NEDO, the State of Rheinland-Pfalz and the University of Kaiserslautern. My special thanks go to Andreas Beck and Sibylle Müller for their help in preparing this report and to Hubert Gerber from Photo-Repro-Druck, TU Kaiserslautern.

It is my special pleasure to greet all former group members. May this report help to stay in touch with each other.

If you are interested in our work I would be happy to hear from you. If you have any questions, comments, suggestions, or any kind of criticism, please contact us.

With all my best wishes for Christmas, and a Happy New Year,

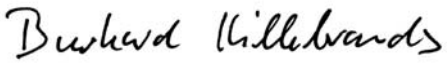

Kaiserslautern, November 2005

Chapter 2: Personnel

2.1 Members of the group

Group leader:

Prof. Dr. Burkard Hillebrands

Senior scientists:

Dr. Britta Leven	since 07/05

Postdocs and long-term guest scientists:

Prof. Dr. Yasuo Ando	since 02/05
Dr. Patrizio Candeloro	since 02/05
Dr. Vladislav Demidov	until 02/05
Dr. Viktor Gittsovich	until 12/04
Dr. Jaroslav Hamrle	since 10/05
Dr. Galina Khlyap	
Dr. Mikhail Kostylev	until 06/05
Dr. Britta Leven	until 06/05
Dr. Run Wei Li	until 01/05
Dr. Alexander Serga	

PhD students:

Dipl.-Phys. Christian Bayer	
Dipl.-Phys. Andreas Beck	
Dipl.-Phys. Steffen Blomeier	
Dipl.-Phys. Dirk Hoffmann	since 02/05
Dipl.-Phys. Lisa Kleinen (Rheinbreitbach)	
Dipl.-Phys. Patricia Martin Pimentel	
Dipl.-Phys. Hans Nembach	
Dipl.-Phys. Maciej Oskar Liedke	
Dipl.-Phys. Markus Weber	

Diploma Students:

Sebastian Hermsdörfer	since 03/05
Dirk Hoffmann	until 01/05
Thomas Schneider	since 11/04
Helmut Schultheiß	until 10/05

Engineers and Technicians

Jörg Elmer (Rheinbreitbach)	until 12/04
Bernd Pfaff	
Dipl.-Ing. (FH) Dieter Weller	

Secretaries:

Sibylle Müller
Heike Schuster (Forschungsschwerpunkt MINAS)

2.2 Visiting scientists, postdoctoral fellows and exchange students

Dr. Michael Krämer, Colorado State University
Fort Collins, USA — 15.11.04 - 15.01.05

Michael, who did his Ph.D. with Carl Patton in Fort Collins, joint us for a short period to work on linear and nonlinear spin wave dynamics with emphasis on damping.

Prof. Gennadiy Melkov, National Taras Shevchenko
University of Kiev, Ukraine — 13.12.04 - 19.12.04, 16.10.05 - 28.10.05

Gennadiy visited the group to participate in the experiments devoted to the nonlinear interactions of spin waves under parametric excitations. He also works on the theoretical aspects of Bose-Einstein condensation of magnons in ferrite garnet films.

Carlos Martinez Boubeta, INESC Lisboa, Portugal — 12.12.04 - 22.12.04

Carlos was involved in the fabrication and testing of novel spin momentum transfer devices to be studied by Brillouin light scattering spectroscopy as part of his ULTRASWITCH young researcher training programme. He received training in Brillouin light scattering spectroscopy.

Prof. Boris Kalinikos, Electrotechnical University St. Petersburg,
St. Petersburg, Russia — 01.06.05 - 01.07.05

Boris spent a research stay in our lab. He was working on a publication of Möbius solitons. Also he was involved in ongoing research on symmetry breaking nonlinear modes in magnetic rings. We greatly appreciate the discussions with Boris on nonlinear phenomena and parametric amplification of spin waves.

Dr. Boriss Marhov, Westfälische Wilhelms-Universität Münster — 04.04.05 - 27.05.05

Boriss has been trained to prepare samples by molecular beam epitaxy and their characterization by different methods. He was involved in the in-situ surface characterization of the grown layers and their surface treatment by using a plasma beam source. He obtained the knowledge for his further work in the EU founded ULTRASMOOTH project at the University of Münster in the group of Sergej Demokritov.

Prof. Andrei Slavin, University of Rochester, Michigan, U.S.A. 16.05.05 - 16.06.05, 23.09.05 - 15.11.05

Andrei spent the major part of his sabbatical leave with our group. His stay was supported by our Graduate School ("Graduiertenkolleg"). He was delivering a course of lectures on the nonlinear dynamics of spin waves in magnetic films and on generation of microwave spin waves by spin-polarized current. During the second part of his visit he was working on the theory of Bose condensation of spin waves in ferrite films.

Prof. Darrell Comins, Department of Physics,
University of the Witwatersrand, Johannesburg, South Africa 04.09.05 - 11.09.05

Darrell made a short visit to finalize work on elastic properties of tungsten carbide films, where mode crossing effects were identified using a new Monte Carlo approach together with a Green's function technique to fit the measured mode dispersion.

2.3 Guest seminars

Dr. Marco Pratzer 08.11.2004	Johannes Gutenberg Universität Mainz *Scanning tunneling spectroscopy applied to ferromagnetic monolayers* Sonderseminar
Dr. Vasily Moshnyaga 02.12.2004	Universität Göttingen *Metal-Isolator transition and magnetoresistance in Manganite thin films: Lattice strain and disorder effects* Sonderseminar Graduiertenkolleg
Dr. Patrizio Candeloro 06.12.2004	University of Brescia, Italy *Nanofabrication techniques for gas sensor technology* Sonderseminar
Dr. Ralf Meckenstock 27.01.2005	Ruhr-Universität Bochum *Anisotropy of magnetic parameters, Gilbert damping and g-factor in magnetic heterostructures detected by conventional and locally resolved ferromagnetic resonance (FMR)* MINAS-Kolloquium
Dr. Thomas Gerrits 27.01.2005	NIST, Boulder, Colorado, USA *Local and non-local magnetization dynamics and spin accumulation in normal metals, probed by magneto-optics and inductive techniques* Sonderseminar
Dr. Mathias Klaeui 14.02.2005	Universität Konstanz *Quasi-particle behaviour of geometrically confined domain walls and switching by current induced domain wall propagation* Sonderseminar
Dr. Boriss Mahrov 25.04.2005	University of Münster *Dye sentizied photovoltaics* Sonderseminar
Prof. Yasuo Ando 02.05.2005	Tohoku University, Sendai, Japan *Recent development of MRAM (magnetic random access memory) and related phenomena* Physikalisches Kolloquium
Prof. Andrei Slavin 23.05.2005	University of Rochester, Michigan, USA *Nonlinear microwave dynamics in magnetic nano-structures driven by a spin-polarized current* Sonderseminar
Prof. Yasuo Ando 30.05.2005	Tohoku University, Sendai, Japan *Recent progress in tunnel magnetoresistance effect* Sonderseminar

Prof. Claudia Felser 30.05.2005	Johannes Gutenberg Universität Mainz *New materials with high spin polarization: properties of CO_2 YZ Heusler compounds* Physikalisches Kolloquium
Prof. Boris Kalinikos 13.06.2005	Electrotechnical University, St. Petersburg Russia *Nonlinear dynamics of spin waves in magnetic films* Sonderseminar
Prof. Andrei Slavin 20.10.2005	Oakland University, Rochester, USA *Nonlinear dynamics in an array of current-driven magnetic nano-contacts* Graduiertenkolleg
Prof. Gennadiy Melkov 20.10.2005	National Taras Shevchenko University of Kiev, Ukraine *Bose-condensation of magnons in YIG films under the action of an external electromagnetic pumping field* Graduiertenkolleg

2.4 Visits of group members at other laboratories

Andreas Beck	IPHT Jena 06.12.-10.12.04 Host: Dr. R. Mattheis
Andreas Beck	IPHT Jena 07.02.-11.02.05 Host: Dr. R. Mattheis
Alexander A. Serga	Taras Shevchenko National University of Kiev, Uraine 18.06.-26.06.2005 Host: Prof. Dr. G. Melkov
Patricia Martín Pimentel	Sensitec-Naomi Mainz 15.08.-30.09.05 Host: Dr. H. Grimm

2.5 Group member photo gallery

Prof.Dr. Yasuo Ando
Guest scientist

Christian Bayer
Ph.D. student

Andreas Beck
Ph.D. student

Steffen Blomeier
Ph.D. student

Dr. Patrizio Candeloro
Postdoc

Dr. Vladislav Demidov
Postdoc

Jörg Elmer
Technician

Dr. Viktor Gittsovich
Guest scientist

Dr. Jaroslav Hamrle
Postdoc

Sebastian Hermsdörfer
Diploma student

Prof. Dr. Burkard Hillebrands
Group leader

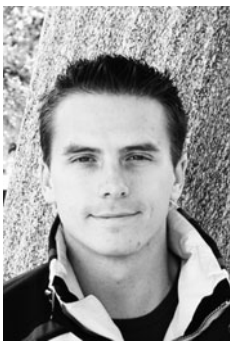

Dirk Hoffmann
Ph.D. student

Dr. Galina Khlyap
Guest scientist

Lisa Kleinen
Ph.D. student

Dr. Mikhail Kostylev
Senior scientist

Dr. Britta Leven
Senior scientist

Dr. Runwei Li
Postdoc

Maciej Oskar Liedke
Ph.D. student

Patricia Martín Pimentel
Ph.D. student

Sibylle Müller
Secretary

Hans Nembach
Ph.D. student

Bernd Pfaff
Technician

Thomas Schneider
Diploma student

Helmut Schultheiß
Diploma student

Heike Schuster
Secretary

Dr. Alexander Serga
Senior scientist

Markus Weber
Ph.D. student

Dieter Weller
Mechanical engineer

Chapter 3: Research Topics

The field of magnetism in films and multilayers is still a strongly developing area in modern solid state physics. This is caused both by the challenging developments in the discovery and understanding of the basic physical phenomena, and by the strong impact into industrial applications in the areas of sensors and information storage technology. New mechanisms like interlayer exchange coupling, the giant magnetoresistance effect, the room-temperature tunneling magnetoresistance effect, and, since very recently, spin current phenomena were discovered all within the last one and a half decade. Applications based on these effects were developed, like the magnetic read head based on the giant magnetoresistance effect found in nearly every hard disk drive sold nowadays. The combination with microelectronics, the so-called field of magneto-electronics is strongly expanding and bridging the gap between conventional magnetism and semiconductor physics in view of potential applications in sensor devices and magnetic random access memories, as well as new fields such as magnetic logic.

Most of our research projects are in this field. A main focus is on spin dynamics. We study the eigen-frequency spectrum of excitations of the magnetization on the frequency scale using the Brillouin light scattering technique, and the temporal evolution by time resolved magneto-optic methods. We investigate high frequency properties like spin waves, time dependent magnetization effects, and fast magnetic switching. Recently, our focus shifted strongly towards transport phenomena using linear and nonlinear spin waves.

A key issue is the fabrication of high-quality epitaxial film and multilayer systems and devices using molecular beam epitaxy as prototype systems to study fundamental problems.

In the field of applications we address problems of fast magnetic switching and the exchange bias effect. We transfer our results into actual devices by working closely together with industrial partners.

Magnetic films are very attractive and versatile nonlinear media. Considering spin waves in films as one example of nonlinear waves we study nonlinear effects which are of a great importance for nonlinear science in general.

As a second working area we develop and investigate carbon films for medical applications in the framework of the Institute for Thin Film Technology in Rheinbreitbach.

Overview on projects

1) Epitaxial magnetic films and multilayers: growth, structure and magnetic properties

The preparation of samples with highest possible structural quality and characterization is very important to be able to study magnetic phenomena with the required precision. We achieve this by using molecular beam epitaxy employing the standard *in-situ* methods for chemical and structural analysis. They comprise Auger spectroscopy for chemical analysis, low and high energy electron diffraction, and *in-situ* scanning tunneling and atomic force microscopy. To characterize the magnetic properties we perform *in-situ* Brillouin light scattering spectroscopy and magneto-optic Kerr effect magnetometry. *Ex-situ*, the samples are investigated using Brillouin light scattering spectroscopy, vector Kerr magnetometry, vibrating sample magnetometry, and more. Scientific subjects are magnetic anisotropies induced at interfaces and by controlled

defects, and interlayer coupling effects between magnetic films in multilayers. Special attention is paid to the interplay between the morphology at the interfaces (atomic defects, steps, roughness and interdiffusion) and the magnetic properties.

2) Surface smoothing

It is very important to fabricate films and multilayers with maximum degree of smoothness. Undesirable roughness, for example, results in a reduced figure of merit in magnetoelectronic devices. We develop a technology to smooth surfaces of films after their preparation. For this purpose we use low-energy beams of argon ions. Mono-energetic, low-energy ions allow for a very controllable smoothing process of the surface without creation of an essential number of defects.

3) Dynamic magnetic properties of laterally patterned nanostructures

We investigate the basic magnetic properties of systems patterned on the micrometer to nanometer scale. In particular we focus on the domain structure and the change in the spin wave mode spectrum due to lateral confinement effects. We have developed a Brillouin light scattering setup, operating in a Fourier microscope like mode, to obtain sub-micrometer scale spatial information about the distribution of dynamic excitations in small magnetic objects. We also developed a micro-focus Brillouin light scattering system to investigate single magnetic elements. Using these methods we have observed lateral quantization of spin waves in magnetic stripes and rectangular elements. Main results are the observation of quantized modes and of edge modes existing in areas with a large internal field gradient, and static and dynamic coupling effects between magnetic objects. The experiments are accompanied by numerical simulations. A new area is the spin-wave tunneling effect and applications to spin wave logic.

4) Nonlinear properties of high-amplitude spin waves

Spin waves with high precession angles are an interesting object for the investigation of general effects of nonlinear wave propagation in dispersive, anisotropic, and dissipative media. Contrary to nonlinear optical pulses, the spectrum of spin waves can be easily manipulated, by, e.g., changing the orientation and the value of the applied magnetic field. In addition spin waves are much slower than light pulses making their observation easier.

Using the time-resolved Brillouin light scattering technique developed in our lab, we measure the intensity distribution of spin waves propagating in a magnetic film with spatial and temporal resolution. Central problems are: the amplification of spin waves in the linear and nonlinear intensity regimes, the formation of instabilities (e.g. self-focusing), the propagation of nonlinear excitations (solitons, magnetic “bullets”) and excitations in nonlinear media with a nontrivial topology such as rings. An important development of these studies is the investigation of self-generation of solitons and bullets in loops with an electronic feedback, the development of a spin wave soliton “laser”, and the discovery of symmetry-breaking spin wave modes like the “Möbius” solitons.

5) Fast magnetic switching

For memory devices it is of special importance how fast and secure magnetic domains can be written and the magnetization of a single magnetic object can be reversed. The corresponding time scale is in the picosecond to nanosecond regime. In order to investigate these phenomena a time-resolved scanning magneto-optic Kerr microscope has been constructed. The time

evolution of the magnetization is sensed stroboscopically. The magnetization dynamics, spin wave propagation effects and in particular the switching behavior of thin magnetic films and nanostructures are investigated.

6) Magnetic nanopatterning

Ion irradiation is an excellent tool to locally modify magnetic properties on the sub-micrometer scale, without substantially affecting the surface topography. This effect is used to magnetically pattern ultrathin films and multilayers using resist masks patterned by electron beam lithography. The major difference between this technique and conventional lithographic techniques is that the environment of the nanostructures can also be magnetic (paramagnetic, antiferromagnetic). A focus is on coupled magnetic systems, such as exchange bias bilayers and exchange coupled trilayers.

7) Exchange bias systems

The investigation of exchange bias systems is of fundamental as well as technological importance. The effect is a shift of the hysteresis loop along the field axis, and it appears in multilayers of coupled ferromagnetic and antiferromagnetic films. In particular we study structurally well characterized epitaxial bilayers. The role of defects and interfacial mixing is investigated using ion irradiation in order to artificially create disorder. Ion irradiation techniques are also applied to modify the magnitude and direction of the exchange bias field. TEM studies are carried out to investigate the structural and magnetic properties as well as their dependency on the irradiation with He^+ and Ga^+ ions. A picosecond all-optical pump-probe setup was developed to study thermal activated unpinning of the exchange coupling at the FM/AF interface. This is of high technological interest, especially for magnetic sensor and storage applications.

8) Biofunctionalized surfaces for medical applications

Amorphous thin carbon films are known to be very biocompatible, and they can be prepared by various deposition techniques to qualify for miscellaneous applications in the biological and medical field. At the Institute for Thin Film Technology we develop in close collaboration with our spin off company NTTF GmbH biocompatible and biofunctionalized surfaces for medical implants, surgical instruments and cellbiological equipment. Currently we are working on carbon coatings for endwelling catheters and cell culture dishes (both made of temperature sensitive polymers) as well as on the development of diffusion barrier coatings on polymers.

Chapter 4: Equipment

A) Preparation and characterization of thin films and multilayers

1. multi–chamber molecular beam epitaxy system (Pink GmbH) comprising
   a. deposition chamber
      (electron beam and Knudsen sources, RHEED, LEED, Auger)
   b. scanning tunneling and atomic force microscopy chamber
      (*in-situ* STM/AFM, Park Scientific)
   c. Brillouin light scattering and Kerr magnetometry chamber
      (magnetic field 1.2 T, temperature range 80 – 400 K)
   d. load lock chamber
   e. preparation chamber
      (optical coating, heating station 2300°C)
   f. transfer chamber
   g. atom beam reactor chamber with *in-situ* four point probe resistance measurement stage
2. two-chamber UHV multideposition system
   a. deposition chamber
      (electron beam and Knudsen sources, LEED, Auger)
   b. ion beam sputtering chamber with ion beam oxidation module and mask system
3. two-magnetron sputtering system for hard coatings
4. atomic force microscope (Solver, NT-MDT)
5. clean room facility with flow box, spin coater, etc.

B) Magnetic characterization

1. vibrating sample magnetometer with alternating gradient magnetometer option
   (magnetic field 1.6 T, room temperature)
2. vector Kerr magnetometer
   (longitudinal and transverse Kerr effect, magnetic field 1.2 T, temperature range 2 – 350 K, automated sample positioning)
3. time-resolved vector Kerr magnetometer (10 ps time resolution and microwave setup for generation of short field pulses)
4. scanning Kerr microscope with time resolution
5. picosecond all-optical pump-probe setup (adjustable delay up to 6 ns; ps-laser Lumera Lasers GmbH)
6. magnetic force microscope with magnet (NT-MDT)
7. two Brillouin light scattering spectrometers, computer controlled and fully automated (magnetic field 2.2 T) with stages for
   a. low temperature measurements (2 – 350 K)

   b. space-time resolved measurements for spin wave intensity mapping (resolution 50 µm, 0.83 ns)
   c. micro-focus measurements (focus diameter 0.3 µm)
   d. *in-situ* measurements
   e. elastic measurements
8. microwave setup (up to 32 GHz) comprising a network analyzer, microwave amplifiers, modulators, pulse generators, etc.
9. magnetotransport setups (magnetic field 1.5 T, temperature range 20 – 400 K)

C) Equipment at the Institute for Thin Film Technologies (IDST), Rheinbreitach

1. Preparation of thin films:
   a. chemical vapor deposition (CVD) facility
   b. physical vapor deposition (PVD) facility
   c. plasma enhanced CVD (PECVD) facilities with an inductively coupled rf-plasma beam source and several magnetrons of different sizes
2. Surface and thin film analysis:
   a. profilometer: measurement of coating thickness and roughness determination of intrinsic stress and Young modulus
   b. Ball on Disk: measurement of friction coefficient analysis of surface friction
   c. Revetest: determination of adhesive strength analysis of microcracks
   d. microindention: determination of plastic and elastic microhardness (Vickers)
   e. optical contact angle measurement: determination of solid surface free energy and surface tension evaluation of hydrophobicity and hydrophilicity
   f. reflection- and transmission-spectroscopy (UV-VIS): optical measurements with wavelength range from 185 nm to 915 nm (resolution 1 nm), determination of absorption coefficient and optical gap (Tauc)
   g. (environmental) scanning electron microscopy (ESEM)[1]: comprehensive structural microanalysis of conducting, isolating, anorganic, organic and wet samples
   h. energy dispersive X-ray microanalysis (EDX)[1]: non-destructive fast analysis of elements
   i. neutron activation analysis (NAA)[2]: qualitative und quantitative analysis of main and trace components
   j. elastic recoil detection analysis (ERDA)[2]: analysis of trace elements with depth resolution analysis of hydrogen content
   k. Rutherford Backscattering (RBS)[2]: analysis of trace elements with depth resolution
   l. synchrotron-X-ray-fluorescence (SYXRF)[2]: non-destructive analysis of elements

[1] in cooperation with NTTF GmbH, Rheinbreitbach

[2] (accelarator enhanced analysis in cooperation with the accelarator laboratories of the Universities of Munich, Bonn and Cologne

Chapter 5: Transfer of Technology

1. Magnetism

With our facilities within the Department of Physics at the University of Kaiserslautern we offer consultance and transfer of technology in the areas of thin film magnetism, magnetic film structures and devices, magnetic sensors, and in corresponding problems of metrology.

We are equipped to perform magnetic, transport, elastic and structural measurements of films and multilayer systems.

This is in detail:

- magnetometry using vibrating sample magnetometry, Kerr magnetometry, Brillouin light scattering spectroscopy
- magnetic anisotropies, optionally with high spatial resolution
- magneto-transport properties
- test of homogeneity of magnetic parameters
- exchange stiffness constants in magnetic films
- elastic constants
- surface topography

2. Institut für Dünnschichttechnologie (IDST) - Transferstelle der Technischen Universität Kaiserslautern, Rheinbreitbach

(Institute for Thin Film Technology - Center for Technology Transfer of the University of Kaiserslautern, Rheinbreitbach)

As part of technology transfer the Institute of Thin Film Technology (IDST) offers among other activities

- consultance in tribological problems
- development of product specific coatings
- optimization of coatings especially for medical applications
- coating of polymers and temperature sensitive materials
- coating of samples and small scale production series
- management for R&D-projects

The institute is located in Rheinbreitbach about 20 km south of Bonn in the Center for Surface Technologies (TZO) to support the economy in the northern part of the Rheinland-Pfalz State.

Address:

Institut für Dünnschichttechnologie
Maarweg 30-32
53619 Rheinbreitbach, Germany

Scientific director:

Prof. Dr. B. Hillebrands phone: +49 631 205 4228
e-mail: hilleb@physik.uni-kl.de

Contact:

Lisa Kleinen phone: +49 2224 900 693
fax: +49 2224 900 694
e-mail: kleinen@physik.uni-kl.de

Please contact us for more information.

Chapter 6: Experimental Results

A. Dynamic Magnetic Phenomena

6.1 Space resolved dynamics in small magnetic rings

H. Schultheiß, H.T. Nembach, M.C. Weber, S. Blomeier, P.A. Beck, P. Candeloro, C. Bayer, B. Leven, and B. Hillebrands[1]

Within the last decade, the investigation of spin dynamics in small magnetic elements with rectangular geometries led to the discovery of quantized spin waves [1]. These phenomena have been successfully described within the framework of a reduced dimensionality of the investigated microstructures and the existence of spin wave wells due to an inhomogeneous internal field distribution [2]. Recently, quantized spin waves have also been found in small permalloy elements with a ring-like geometry by broadband FMR studies [3].

For the ring geometry, two primary magnetic domain state configurations exist, the so called "vortex" state and the "onion" state. In the vortex state, both the magnetization and the internal magnetic field do not have any radial component and create a flux closure state with rotational symmetry. The onion state, however, exhibits a broken rotational symmetry (see Fig. 1a) and, correspondingly, magnetic surface charges generating a strongly inhomogeneous internal magnetic field (see Fig. 1b). In particular, the local magnetic properties, including the internal field, at $\alpha = 90°$ and 270° (see Pos. 1 in Fig. 1a) and at $\alpha = 0°$ and 180° (see Pos. 2 in Fig. 1a) differ significantly

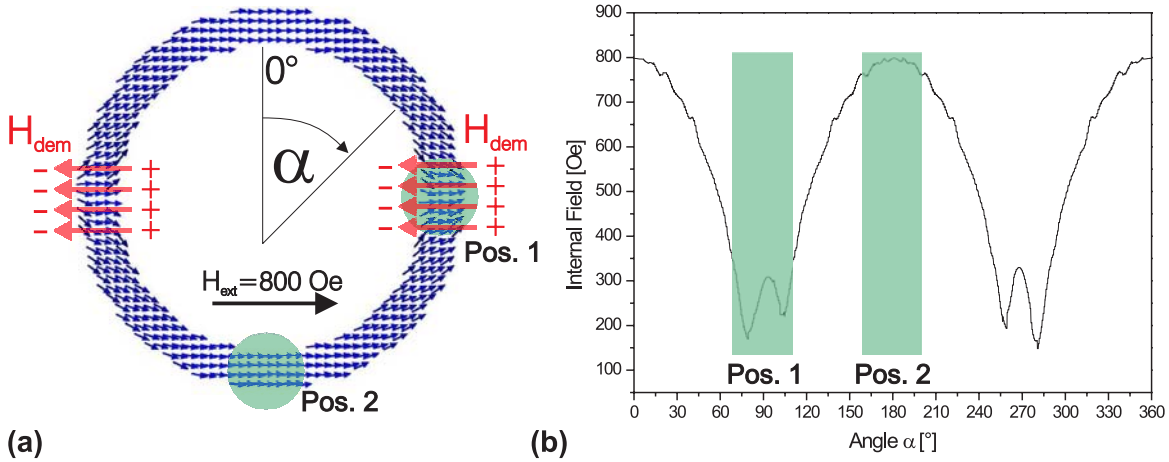

Fig. 1: (a) Micromagnetic simulation of the ring structure in the onion state for an applied field of 800 Oe. A demagnetizing field H_{dem} is generated by effective magnetic surface charges within the pole regions (Pos. 1) leading to a strong reduction of the internal field. (b) Magnitude of the internal magnetic field along the ring perimeter as a function of the angle α defined in (a). Areas exist with absence of surface charges, such as at Pos. 2. Here the magnitude of the internal field equals the externally applied field of 800 Oe. Micro-BLS studies have been performed on the gray shaded areas of the ring structure.

[1] In collaboration with J. Podbielski, F. Giesen, and D. Grundler, Institut für Angewandte Physik und Zentrum für Mikrostrukturforschung, Universität Hamburg, Germany.

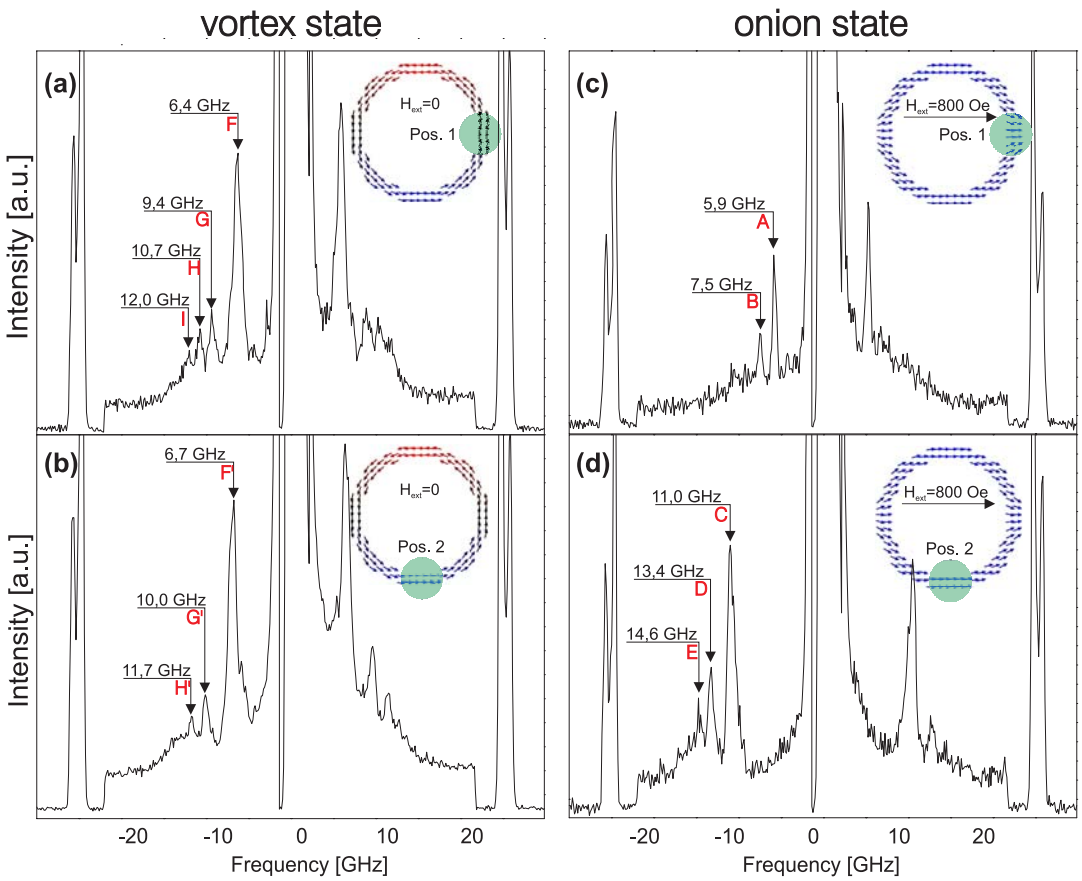

Fig. 2: Micro-BLS spectra of the ring structure in the vortex (left column) and onion state (right column). The upper panels ((a), (c)) of each column display the results at Pos. 1, whereas the lower panels ((b), (d)) represent spectra recorded for Pos. 2 of the measured single ring structure.

from each other. Due to such inhomogeneities different types of quantized spin waves can be expected for the onion state at these particular ring segments. In this report, we present the results of experimental investigations on such homogeneous and inhomogeneous ring structures. For this purpose, Brillouin light scattering microscopy (micro-BLS) studies were performed on permalloy rings with an outer diameter of 2 µm, a width of 230 nm and a thickness of 15 nm, which have been prepared by electron beam lithography by J. Podbielski at the Institut für Angewandte Physik und Zentrum für Mikrostrukturforschung at the University of Hamburg. The micro-BLS technique can be used to determine the dynamic properties of such structures in the frequency regime with a spatial resolution near 300 nm. Such a high spatial resolution allows for local measurements at different regions of the ring structure. Details of the employed micro-BLS setup can be found elsewhere [4, 5].

The key results of these measurements are presented in Fig. 2. In the left column of Fig. 2, spin wave spectra measured from a single ring magnetized in the vortex state are shown for two positions marked as Pos. 1 and Pos. 2 (see insets of panels (a), (b)). Due to the rotational symmetry of the vortex state the measured spectra are nearly identical. Up to four modes can clearly be resolved (listed are the frequencies at Pos. 1 with frequencies at Pos. 2 in brackets; resonances at Pos. 2 are indicated with a prime). A single strong resonance is found at 6.4 (6.7) GHz (F, F') and two (three) satellite modes (G, G', H, H', I) with lower intensity at higher frequencies can be observed. The differences between the spin wave frequencies deduced from spectra (a) and (b) are most probably

caused by small deviations from a perfect ring structure as a result of the preparation process. The corresponding spin wave spectra recorded for the onion state are completely different. Again, measurements at the two positions (Pos. 1 and Pos. 2, see inset Fig. 2c and 2d) have been performed. In the spectrum obtained at the pole segment $\alpha = -90°$ (see panel (c)), only two weak resonances at 5.9 and 7.5 GHz (A, B) can be observed, whereas at $\alpha = 180°$ the spin wave spectrum has a very similar structure compared to that of the vortex state (see panel (d)). A single strong resonance at 11 GHz (C) and weaker satellite modes (D, E) are visible.

Moreover, analyzing the spectra measured for the onion state configuration in more detail yields a frequency shift of the spin wave modes at Pos. 2 compared to those recorded for Pos. 1. This shift to higher frequencies can be understood as a result of the inhomogeneity of the internal magnetic field, which has been deduced from micromagnetic simulations using the OOMMF code [6] for the permalloy ring structures (see Fig. 1). The chosen simulation parameters, such as dimensions and material properties, match those of the experimentally investigated mesoscopic rings. At Pos. 2, the internal field is equal to the externally applied magnetic field of 800 Oe, whereas at Pos. 1 the internal field is reduced due to the demagnetizing field caused by the effective surface charges at the poles of the onion state. Hence, the reduction of the internal magnetic field is directly correlated to a reduction of the spin wave frequencies at this particular position compared to the region of a high internal field acting on the spins at Pos. 2.

The similarity between the spin wave spectra at Pos. 2 of both the vortex and the onion state is not surprising due to the same local magnetization configuration at this particular position. For the onion as well as the vortex state the magnetization is aligned along the ring perimeter, however, subject to different internal magnetic fields. Therefore, it is reasonable to assume that in both cases the localization conditions and the character of the spin waves are comparable. In order to

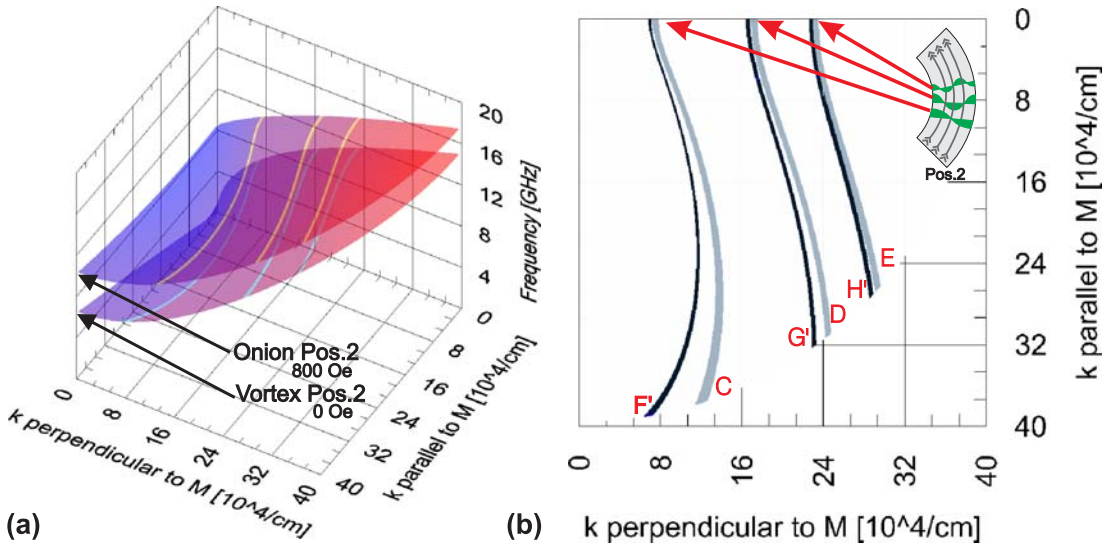

Fig. 3: (a) Spin wave manifolds, i.e., spin wave frequencies versus in-plane wavevectors k, for a 15 nm thin permalloy film calculated for magnetic fields of 0 Oe and 800 Oe, respectively. The measured spin wave frequencies at Pos. 2 of Fig. 2b, d are highlighted by solid lines in the dispersion surfaces. (b) Projection of the three-dimensional dispersion surfaces onto the wavevector plane. The frequency lines marked by C,D,E,F',G',H' correspond to the measured resonances of Fig. 2b, d. Only for the situation of $k_{\mathrm{parallel}} = 0\,\mathrm{cm}^{-1}$ the observed spin wave modes for both the onion and vortex state have coincident wavevectors, yielding strong evidence for spin waves confined by the inner and outer perimeter of the ring, i.e., perpendicular to the magnetization. Hence, the observed modes at Pos. 2 of the ring are quantized in radial direction, displayed by the schematic mode profiles in the inset.

check the assumption of identical quantization conditions, the spin wave dispersion manifold for a 15 nm thin continuous permalloy film was calculated for magnetic fields of 0 Oe and 800 Oe (see Fig. 3a). The measured spin wave frequencies at Pos. 2 of both the onion and the vortex state are highlighted by lines within the respective dispersion surfaces. As can be seen from the projection onto the wavevector plane in Fig. 3b, this calculation yields identical values for the wavevectors perpendicular to the magnetization for both domain states. This implies that at Pos. 2 within the ring segment the spin waves are quantized in radial direction and the satellite modes at higher frequencies correspond to radial modes with a higher quantization number. Thus, spin wave confinement due the existing geometric boundary conditions in the examined ring structure leads to discrete spin wave frequencies. This situation is comparable to the case of longitudinally magnetized mesoscopic stripes, where laterally standing spin waves of Damon-Eshbach surface mode type have been found by our group by conventional Brillouin light scattering spectroscopy [7].

In addition, inhomogeneities of the internal magnetic field can also lead to spin wave quantization, which has already been shown by Jorzick et al. for transversally magnetized permalloy stripes [2]. The magnetization pattern within the pole region (Pos. 1) of the onion state, where the spins point perpendicular to the ring perimeter, can be approximated by the magnetization distribution of a transversally magnetized stripe. Hence, we expect spin wave quantization predominantly caused by the inhomogeneities of the internal magnetic field within Pos. 1. This quantization condition differs significantly from that found at Pos. 2. Thus, again considering the spin wave dispersions for the internal fields of 170 Oe and 800 Oe, calculated for Pos. 1 and 2 of the the onion state (see Fig. 1b), we cannot expect any coincidence of possible wavevectors corresponding to the measured spin wave frequencies for both regions. Indeed, there are no crossings of the frequency lines in the projection of the calculated spin wave surfaces (see Fig. 4a) onto the wavevector plane for

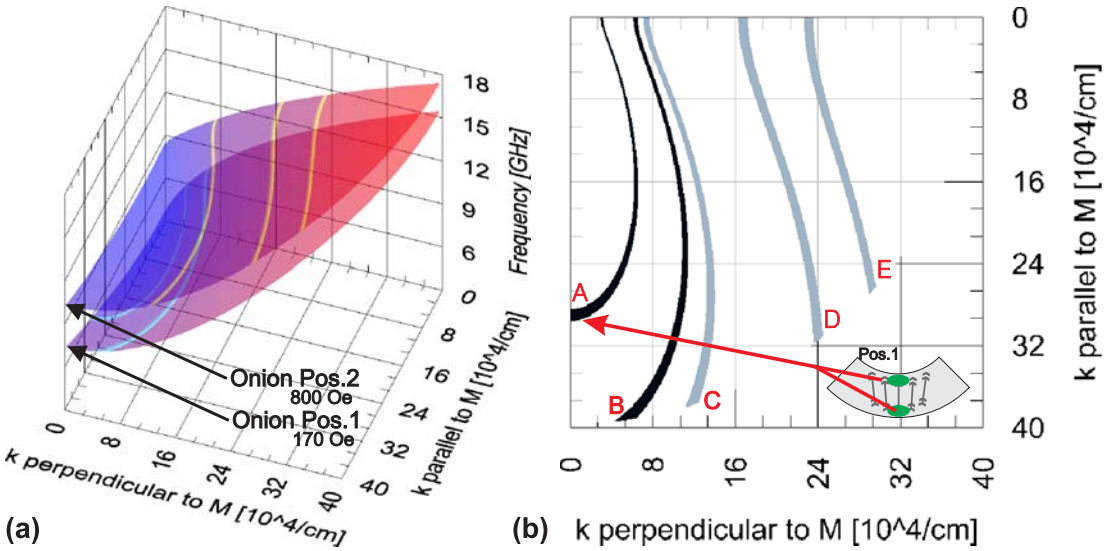

Fig. 4: (a) Spin wave manifolds calculated for magnetic fields of 170 Oe and 800 Oe, respectively. The measured spin wave frequencies in the onion state at Pos. 1 and 2 of Fig. 2c, 2d are highlighted by solid lines in the dispersion surfaces. (b) Projection of the dispersion surfaces onto the wavevector plane. The frequency lines marked by A,B,C,D,E correspond to the measured onion state resonances of Fig. 2c, 2d. No crossings of the lines appear for any direction of the spin wave wavevector with respect to the magnetization. Thus, no spin wave quantization due to geometric boundaries can be expected, however, localization in effective spin wave wells (see inset) due to the inhomogeneous internal field distribution in radial direction within the pole region is reasonable.

any direction with respect to the magnetization (see Fig. 4b). This implies that the quantization conditions and the spin wave character at Pos. 1 differ considerably from those at Pos. 2. Therefore, the origin of mode localization within the pole regions most probably lies in the existence of effective spin wave wells due to inhomogeneities of the internal magnetic field in radial direction.

In summary, the space resolved investigation of spin waves localized to micron-sized ring segments due to two different quantization mechanisms have been investigated. The coexistence of two fundamental quantized spin waves has been found.

Support by the Schwerpunktsprogramm 1133 of the Deutsche Forschungsgemeinschaft and the EU-RTN ULTRASWITCH is gratefully acknowledged. M.C.W. acknowledges support by the Graduiertenkolleg 792 of the Deutsche Forschungsgemeinschaft and C.B. support by the Studienstiftung des Deutschen Volkes.

References

[1] S.O. Demokritov, Physics Reports, **348**, 441-489 (2001).
[2] J. Jorzick, S.O. Demokritov, B. Hillebrands, D. Berkov, N.L. Gorn, K. Guslienko, A.N. Slavin, Phys. Rev. Lett. **88**, 047204 (2002).
[3] F. Giesen, J. Podbielski, T. Korn, D. Grundler, Appl. Phys. Lett. **86**, 112510 (2005).
[4] V.E. Demidov, S.O. Demokritov, B. Hillebrands, M. Laufenberg, P.P. Freitas, Appl. Phys. Lett. **85**, 2866 (2004).
[5] V.E. Demidov, S.O. Demokritov, B. Hillebrands, *Brillouin light scattering measurements of single micrometer sized magnetic elements*, Annual Report 2003, Chapter 6.2.
[6] M.J. Donahue, D.G. Porter, Report NISTIR 6376, National Institute of Standards and Technology, Gaithersburg, MD (Sept 1999).
[7] J. Jorzick, S.O. Demokritov, C. Mathieu, B. Hillebrands, B. Bartenlian, C. Chappert, F. Rousseaux, A. Slavin, Phys. Rev. B **60**, 15194 (1999).

6.2 Calculation of the spin wave spectrum in a thin film with a periodic perturbation

C. Bayer, M.P. Kostylev, H. Schultheiß, and B. Hillebrands[1]

In this report we present a general method to calculate the spin-wave spectrum in an infinite film with a periodic perturbation. This perturbation can be a periodic modification of any parameter which influences the frequency of a spin wave like the saturation magnetization M_S, the damping constant α, an anisotropy field H_{ani}, the film thickness L, or the internal field H_i. We will concentrate for simplicity on the latter although this method is applicable to all the cases. This method is based on the Green's function approach [1] and on Bloch's theorem.

Figure 1 shows the definition of the coordinate system with the film in the *yz* plane. The dotted lines indicate the different values H_1 and H_2 of the internal field H_i in z direction. The problem is periodic along the y direction with a period of $T = t_1 + t_2$. The k-vector of the spin wave is also directed in y direction and the problem is translational invariant in z direction.

We assume an internal field H_i which models a periodically modulated exchange bias field as currently used in experiments [2]:

$$H_i(y) = \begin{cases} H_1 & \text{for } nT < y < nT + t_1 \quad \text{with an integer } n \\ H_2 & \text{else} \end{cases} \quad . \tag{1}$$

To calculate the spectrum of the spin-wave excitations in this periodic structure one starts from the Landau-Lifshitz equation without damping

$$\frac{\partial \mathbf{M}}{\partial t} = -|\gamma| \mathbf{M} \times \mathbf{H}_{\text{eff}} \quad . \tag{2}$$

The magnetization consists of the static part M_S and small dynamic parts $m_x(y,t)$ and $m_y(y,t)$,

$$\mathbf{M}(y) = \begin{pmatrix} m_x(y) e^{i\omega t} \\ m_y(y) e^{i\omega t} \\ M_S \end{pmatrix} = \begin{pmatrix} \tilde{m}_x(y) e^{iky} e^{i\omega t} \\ \tilde{m}_y(y) e^{iky} e^{i\omega t} \\ M_S \end{pmatrix} \quad . \tag{3}$$

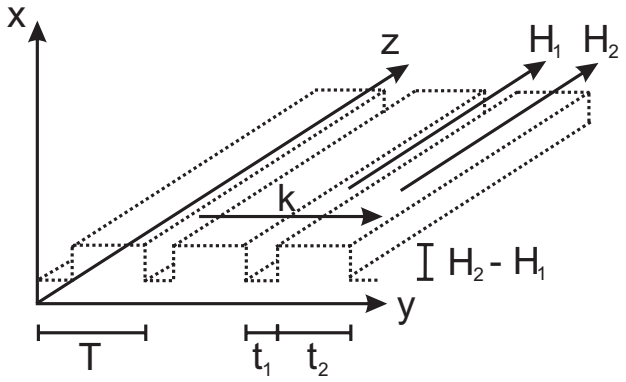

Fig. 1: Definition of the coordinate system with the film in the *yz* plane. The dotted lines indicate the different values H_1 and H_2 of the field in z direction. The problem is periodic along the y direction with period $T = t_1 + t_2$. The k vector of the spin wave is also directed in y-direction.

[1] In collaboration with J. Faßbender, Institut für Ionenstrahlphysik und Materialforschung, Forschungszentrum Rossendorf, 01314 Dresden, Germany; S.O. Demokritov, Institut für Angewandte Physik, Westfälische Wilhelms-Universität Münster, Corrensstr. 2-4, 48149 Münster, Germany; and B. Reuscher, Institut für Oberflächen und Schichtanalytik GmbH, Erwin-Schrödinger-Straße 56, 67663 Kaiserslautern, Germany.

As the problem is periodic with the period T, Bloch's theorem was applied and the dynamic magnetization can be expressed with the periodic functions $\tilde{m}_x(y,k) = \tilde{m}_x(y+T,k)$ and $\tilde{m}_y(y,k) = \tilde{m}_y(y+T,k)$ multiplied by e^{iky}. The Bloch wave vector $k \in [-\frac{\pi}{T}, \frac{\pi}{T}]$ is limited to the first Brillouin zone. Note that $\tilde{m}_x(y,k)$ and $\tilde{m}_y(y,k)$ depend implicitly on k. The effective field

$$\mathbf{H}_{\text{eff}}(y,t) = \mathbf{H}_{\text{i}}(y) + \mathbf{H}_{\text{dip}}(y,t) = \begin{pmatrix} 0 \\ 0 \\ H_{\text{i}}(y) \end{pmatrix} + \begin{pmatrix} h_x(y,t) \\ h_y(y,t) \\ 0 \end{pmatrix} \tag{4}$$

is the sum of the static field Eq. (1) and the dipolar field $\mathbf{H}_{\text{dip}}(x)$. The contribution of the exchange interaction to the effective field is neglected as only spin waves with large wavelengths are considered. The dipolar field can be expressed as

$$\mathbf{H}_{\text{dip}}(y,t) = 4\pi \int_{-\infty}^{+\infty} \mathbf{M}(y',t)\hat{\mathbf{G}}(y,y')dy' \tag{5}$$

with the dipolar Green's function for a thin film with translational symmetry in z direction [1]

$$\hat{\mathbf{G}}(y,y') = \begin{pmatrix} G_{xx} & 0 & 0 \\ 0 & G_{yy} & 0 \\ 0 & 0 & 0 \end{pmatrix} \quad , \tag{6}$$

$$G_{xx}(y,y') = \frac{1}{2\pi L} \ln\left[\frac{(y-y')^2}{(y-y')^2+L^2}\right] \quad \text{and} \quad G_{yy}(y,y') = -\delta(y-y') - G_{xx}(y,y') \quad . \tag{7}$$

Using the expression for the magnetization Eq. (3) the dynamic dipolar field

$$h_x(y) = 4\pi \int_{-\infty}^{+\infty} m_x(y')G_{xx}(y,y')dy' \tag{8}$$

can be also formulated in the reduced zone scheme $h_x(y) = \tilde{h}_x(y,k)e^{iky}$,

$$\tilde{h}_x(y,k) = 4\pi \int_0^T \tilde{m}_x(y',k)\tilde{G}_{xx}(y,y',k)dy' \tag{9}$$

with the Green's function in the reduced zone scheme

$$\tilde{G}_{xx}(y,y',k) = e^{-iky} \sum_{j=-\infty}^{\infty} G_{xx}(y,y')e^{ik(y'+jT)} \quad . \tag{10}$$

Thus, the Landau-Lifshitz equation can be reduced in linear approximation to the spin-wave eigenequations

$$i\omega\tilde{m}_x(y,k) = -|\gamma|H_{\text{i}}\tilde{m}_y(y,k) + |\gamma|M_{\text{S}}\tilde{h}_y(y,k) \quad , \tag{11}$$

$$i\omega\tilde{m}_y(y,k) = +|\gamma|H_{\text{i}}\tilde{m}_x(y,k) - |\gamma|M_{\text{S}}\tilde{h}_x(y,k) \quad . \tag{12}$$

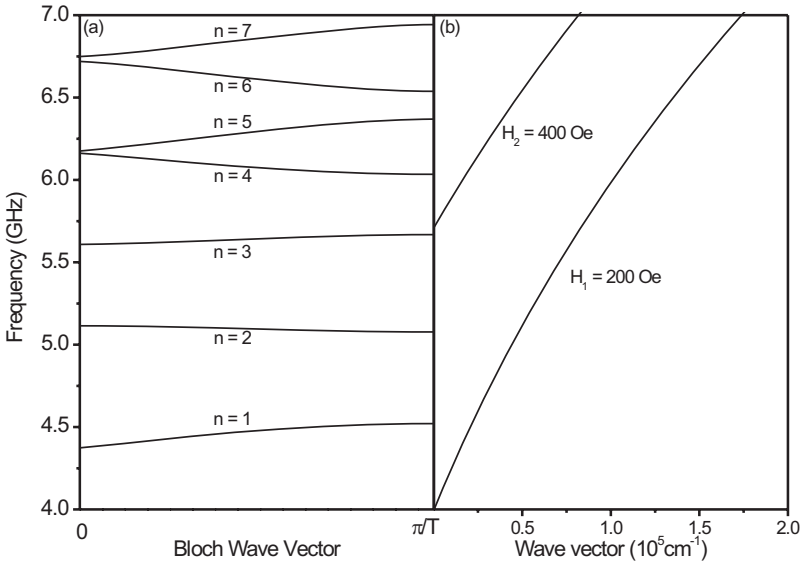

Fig. 2: (a) Frequencies of the spin-wave modes as a function of the Bloch wave vector k. n denotes the number of the band. (b) Dispersion relations of Damon-Eshbach modes in an infinite film for the fields $H_1 = 200\,\mathrm{Oe}$ and $H_2 = 400\,\mathrm{Oe}$.

These equations are solved numerically on a grid with N points and a mesh size $a = T/N$. The lattice points are $y_n = \frac{a}{2} + n \cdot a$, $n \in \{0, ..., N-1\}$. It is assumed that the magnetization is constant within each cell. So the eigenequations can be formulated as a matrix equation

$$\mathrm{i}\omega \begin{pmatrix} \tilde{m}_x(y_1,k) \\ \vdots \\ \tilde{m}_x(y_N,k) \\ \tilde{m}_y(y_1,k) \\ \vdots \\ \tilde{m}_y(y_N,k) \end{pmatrix} = \begin{pmatrix} \hat{\mathbf{A}} & \hat{\mathbf{B}} \\ \hat{\mathbf{C}} & \hat{\mathbf{D}} \end{pmatrix} \cdot \begin{pmatrix} \tilde{m}_x(y_1,k) \\ \vdots \\ \tilde{m}_x(y_N,k) \\ \tilde{m}_y(y_1,k) \\ \vdots \\ \tilde{m}_y(y_N,k) \end{pmatrix} \quad , \tag{13}$$

with the 4 $N \times N$ matrices $\hat{\mathbf{A}}_{nm} = \hat{\mathbf{D}}_{nm} = 0$,

$$\hat{\mathbf{B}}_{nm} = -\gamma H_\mathrm{i}(y_m)\delta_{nm} - |\gamma| 4\pi M_\mathrm{S}\delta_{nm} - |\gamma| 4\pi M_\mathrm{S} e^{-\mathrm{i}k(y_n - y_m)} \sum_{j=-\infty}^{\infty} \int_{y_n-\frac{a}{2}}^{y_n+\frac{a}{2}} \int_{y_m-\frac{a}{2}}^{y_m+\frac{a}{2}} G_{xx}(y,y')\,dy'\,dy e^{\mathrm{i}kjT} \quad , \tag{14}$$

$$\hat{\mathbf{C}}_{nm} = +|\gamma| H_\mathrm{i}(y_m)\delta_{nm} + |\gamma| 4\pi M_\mathrm{S} e^{-\mathrm{i}k(y_n - y_m)} \sum_{j=-\infty}^{\infty} \int_{y_n-\frac{a}{2}}^{y_n+\frac{a}{2}} \int_{y_m-\frac{a}{2}}^{y_m+\frac{a}{2}} G_{xx}(y,y')\,dy'\,dy e^{\mathrm{i}kjT} \quad . \tag{15}$$

The inner integrals in Eq. (14) and Eq. (15) come from the fact that one assumes the magnetization to be constant within each cell and they can be evaluated analytically. The outer integral takes the average of the field acting on each cell and is evaluated numerically. The sum over j is truncated at $j = \pm 10$ with good accuracy.

The calculations are carried out for the parameters $H_1 = 200\,\mathrm{Oe}$, $H_2 = 400\,\mathrm{Oe}$, $t_1 = t_2 = 1\,\mu\mathrm{m}$, $4\pi M_\mathrm{s} = 9000\,\mathrm{Oe}$, and $L = 6\,\mathrm{nm}$ [2]. Figure 2 (a) shows the eigenfrequencies f of the spin waves as a function of the Bloch vector k. Panel (b) shows in direct comparison the dispersion relation of a spin wave in an infinite film for the two different internal fields H_1 and H_2. As it is seen the three lowest bands are nearly dispersion free and the corresponding frequencies can be only found in the dispersion relation in region 1 corresponding to the field H_1. Therefore modes from these bands

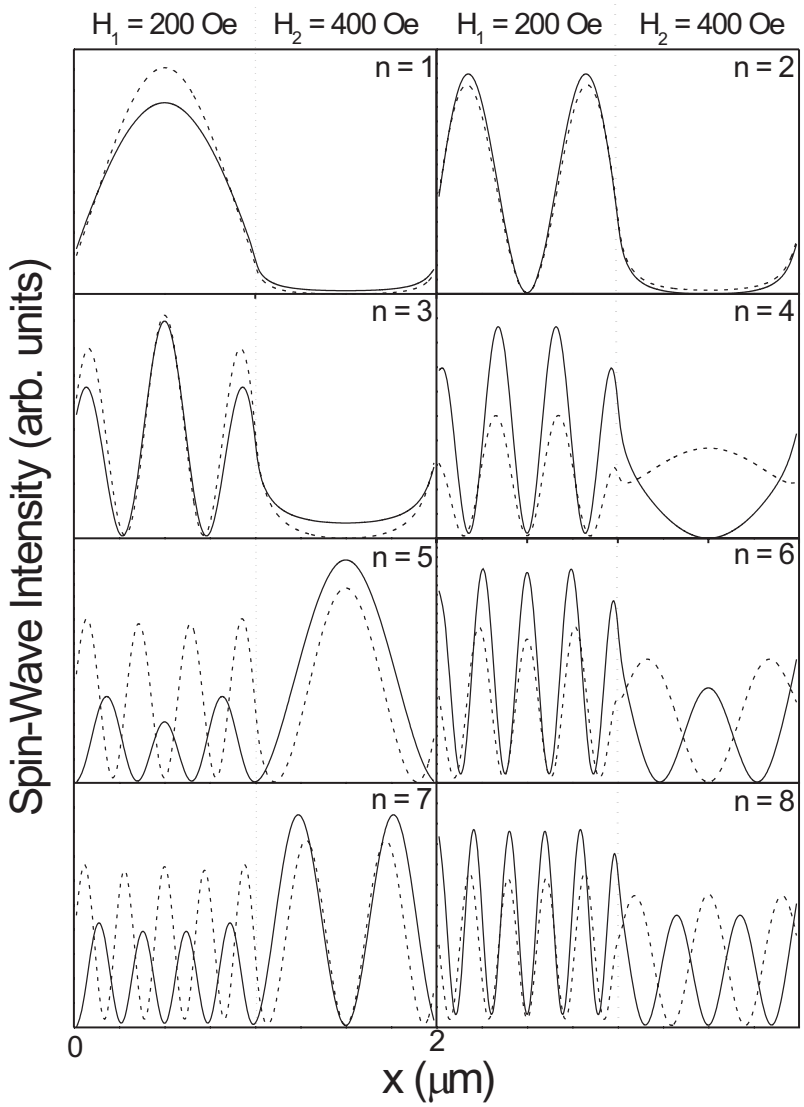

Fig. 3: Distribution of intensity $\tilde{m}_y^2$ for the spin-wave modes with Bloch vector $k = 0$ (solid line) and $k = \pi/T$ (dashed line).

will only have real wave vectors in region 1. The bands with $n \geq 4$ have a pronounced dependence on k. Modes from this bands have real wave vectors in both regions as their frequencies have points of intersection with the dispersion relations in both regions. So the 3 lowest modes correspond to quantized modes in region 1 with low internal field $H_1 < H_2$ whereas modes from the higher bands $n \geq 4$ are propagating waves in the whole film.

Figure 3 supports this conclusions. It shows the corresponding intensity distributions $\tilde{m}_y^2$ for $k = 0$ with a solid line and for $k = \pi/T$ with a dashed line. For the 3 lowest modes the wave has a sinusoidal character in region 1 whereas it decays exponentially in region 2. Furthermore the profiles do not significantly depend on the Bloch wave vector k. For the bands $n \geq 4$ the intensity distributions $\tilde{m}_y^2$ change significantly with k. This means that for the bands $n \geq 4$ the wave propagates through both regions. The observed band gaps also have been discussed in a preceding publication [3].

It should be mentioned that the quantized modes which are localized in region 1 are similar to the localized modes in a transversely magnetized stripe [1]: in both cases modes are spatially localized in a field well. Here, this well is created by a spatially modulated exchange bias field whereas it was created previously by an inhomogeneous internal field.

In conclusion, we have presented a method to calculate the spin-wave spectrum in an infinite film with a periodic perturbation. We have discussed explicitly the spectrum of a film with periodically modulated exchange bias field. We have shown that both localized and propagating modes exist in this system.

This work was supported by the EU-RTN ULTRASWITCH (HRPN-CT-2002-00318) and by the Deutsche Forschungsgemeinschaft. C.B. acknowledges support by the Studienstiftung des deutschen Volkes.

References

[1] C. Bayer, J. Jorzick, B. Hillebrands, S.O. Demokritov, A.N. Slavin, K. Guslienko, D. Berkov, N. Gorn, M.P. Kostylev, in: B. Hillebrands, A. Thiaville (Eds.), Spin Dynamics in Confined Magnetic Structures III, Spinger, in press.
[2] K. Potzger, L. Bischoff, M.O. Liedke, B. Hillebrands, M. Rickart, P.P. Freitas, J. McCord, J. Fassbender, IEEE Trans. Magn. in press.
[3] P.A. Kolodin, B. Hillebrands, J. Magn. and Magn. Mat. **161**, 199 (1996).

6.3 Spin wave logic

M.P. Kostylev, A.A. Serga, T. Schneider, B. Leven, and B. Hillebrands

The integration of computers into every day life requires smaller, more powerful but less power consuming processing units. Parallel data processing, faster interactions between logic functions and memories, and re-configurable logic functions are needed in particular for applications that require image processing. According to the International Technology Roadmap for Semiconductors [1], devices based on silicon-only technology will face serious obstacles hindering downscaling and power reduction within a few years. There exist, however, different concepts of logic devices, including optical ones [2], as well as recently suggested magnetic logic gates of different types [3]. In our work we propose the controllable propagation of spin waves in ferromagnetic films as another physical mechanism to implement logic operations.

Recently it was shown that Mach-Zehnder type spin-wave interferometers may be used for nonlinear processing of microwave signals [4, 5]. In the present work we use current-controlled interferometers in the linear regime of spin wave propagation to construct logic gates. A schematic diagram of a typical Mach-Zehnder interferometer is shown in Fig. 1a. It mainly consists of a splitter that divides the power of the applied wave pulses with the clock rate into two channels (called interferometer branches), two controllable phase shifters attached to the branches, and a mixer where the signals modified by the phase shifters interfere. Such a scheme is employed in a large number of optical devices [2] , including optical digital-to-analog and analog-to-digital converters. We propose that in analogy to this scheme a spin wave logic gate can be constructed, the logic inputs being the amplitudes of signals controlling phase shifts in the phase shifters (as indicated by the currents I_1 and I_2 in Fig. 1a) and the logic output being the amplitude of the mixer output signal. Depending on these control signals the scheme operates as NOT or XOR gate.

In principle all components of the scheme shown in Fig. 1a, including the splitter and mixer, may be implemented as a spin-wave device using a patterned ferromagnetic film on a single substrate. At first, to point out the functionality of a Mach-Zehnder type spin-wave logic gate, it is essential to investigate the most important component of the scheme, the controlled phase shifter (CPS). To implement it as a spin wave device we utilize the dependence of the carrier wave number of the spin wave pulses for a given carrier frequency ω_0 on the constant magnetic field applied to the ferromagnetic film. The fastest way to realize a tunable magnetic field is to vary the dc current flowing through a conductor which is attached to the film surface.

We fabricated prototypes of CPSs based on two different types of spin waves. We used long-wavelength dipolar-dominated spin waves propagating in in-plane magnetized ferrite films parallel or perpendicular to the direction of static magnetization. These waves are also known as “magnetostatic waves”. Spin waves which propagate in the film along the direction of the static magnetic field are called “backward volume magnetostatic spin waves” (BVMSW) due to their negative group velocity. Waves propagating perpendicular to the field are usually called “magnetostatic surface spin waves” (MSSW). In the first place MSSW and BVMSW differ by their dispersion laws [6]. Our results presented in the following demonstrate that both kinds of waves are suitable for implementation of logic gates.

First we discuss a device based on BVMSW propagation (Fig. 1b). The main component of the structure is an yttrium iron garnet (YIG) waveguide (1) (5 µm thick, 1.6 mm wide and 40 mm long). It is grown by liquid-phase epitaxy on a gadolinium-gallium garnet substrate. Microwave BVMSW

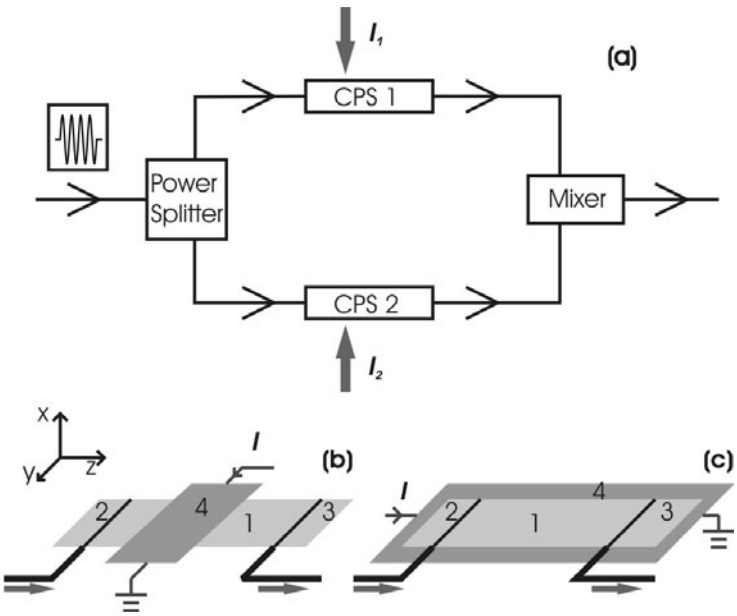

Fig. 1: (a) Schematic diagram of Mach-Zehnder interferometer. (b) Controlled phase shifter (CPS) based on backward volume magnetostatic spin wave (BVMSW) propagation. (c) CPS based on magnetostatic surface spin wave (MSSW) propagation. 1 - ferromagnetic film, 2 - input strip-line microwave transducer, 3 - output microwave transducer, 4 - control-current stripe conductor.

pulses with an initial carrier wavenumber k_0 corresponding to ω_0 are excited in the stripe by the input strip-line transducer (2) and propagate in z-direction. The second transducer (3), placed 8 mm apart from the input transducer (2), serves to detect the BVMSW signal and represents the CPS output. Both the homogeneous external magnetic field H and the static magnetization are oriented parallel to z.

As can be seen in Fig. 1b a copper stripe conductor (4) is mounted perpendicular to the YIG film on the bottom side of the substrate, which defines a distance of 0.5 mm between the conductor plane and the film surface. The stripe width w is 1 mm and its thickness is 0.06 mm. The conductor carries dc current pulses I synchronized in time with the microwave pulses. The current locally changes the constant magnetic field by creating an additional field profile $\delta H(z)$. Our goal is to create a weak profile $\delta H(z)$ with a localization length much larger than the BVMSW wavelength. Thus, we minimize the wave reflection from the inhomogeneity and maximize the additional accumulated phase shift $\Delta\phi$ related to $\delta H(z)$. This was achieved by placing the conductor on the back side of the substrate, far apart from the film surface. Depending on the direction of I, the total field is locally either enhanced or reduced, resulting, respectively, in an up- or down-shift of the local carrier wave number $k(z)$. A positive $\delta H(z)$ shifts the main BVMSW dispersion branch upwards in frequency. For a given carrier frequency ω_0 of the wave pulses this results in an up-shift of the local carrier wave number $k(z)$. If l is the localization length of $\delta H(z)$, $\Delta\phi$ is given by

$$\Delta\phi = \int_0^l [k(z) - k_0]dz \quad . \tag{1}$$

We have measured the CPS operational characteristics and in particular the additional BVMSW propagation losses ΔA inserted by the field inhomogeneity $\delta H(z)$ with a set-up consisting of a microwave generator, a switch to form electromagnetic microwave pulses applied to the CPS input,

and a microwave detector and an oscilloscope to observe the output pulses. To measure the phase shift $\Delta\phi$ we extended the setup adding a reference circuit that includes a directional coupler inserted between the switch output and the CPS input, and a T-connector between the CPS output and the detector. The microwave power from the second output of the directional coupler was fed through a variable phase shifter to the second input of the T-connector. We observed the interference signal of the two pulses, one transmitted through the CPS and the other transmitted through the reference circuit. To measure $\Delta\phi(I)$ we adjusted the phase inserted by the calibrated variable phase shifter to retrieve the amplitude of the interference signal corresponding to $I = 0$.

We investigated the spin-wave spectrum range $k_0 L \ll 1$, where the spin wave spatial damping is low. (Here L is the YIG stripe thickness.) We found that in the current range from 0 A to 2 A the $\Delta\phi(I)$ dependence for any k_0 is quite linear. Figure 2a shows examples of the dependence. The slope $\Delta\phi(I)/I$ is almost independent of k_0 (Fig. 2b), the latter being varied by changing H while keeping ω_0 constant at $\omega_0/(2\pi) = 7.125\,\mathrm{GHz}$. The measurements showed that $\Delta\phi = \pi$, the minimum value necessary for operation of a XOR interferometric logical gate, is easy to obtain. From the measurements of the current-induced insertion loss ΔA we found that for the largest current applied ($I = 3\,\mathrm{A}$) ΔA does not exceed 1 dB.

The current which is required to shift the CPS output phase by π is about 1 A, which represents a large value from the point of view of applications. To optimize the construction we made a theoretical calculation of $\Delta\phi$. From the approximate BVMSW dispersion law [7] we find that for $\delta H \ll H$

$$k(z) - k_0 = \frac{(\gamma H)^2 + \omega_0^2}{2\pi\gamma^2 M_S H L} \frac{\delta H(z)}{H} \quad , \tag{2}$$

where $4\pi M_S = 1750\,\mathrm{G}$ is the saturation magnetization of YIG and $\gamma = 2\pi \cdot 2.82\,\mathrm{MHz/Oe}$. Since for a stripe conductor the Oersted field $\delta H(z)$ is proportional to the linear current density I/w, the additional phase shift $\Delta\phi$ is linearly proportional to the current I. For a given current value the phase shift does not depend on the stripe width w, since the increase of $\Delta\phi$ due to the increase of the phase accumulation path l (see Eq. (1)), which in this case is approximately equal to the stripe width, is compensated by a decrease of $\Delta\phi$ due to the decrease of the current density. Thus in the BVMSW configuration there is no way to increase the slope $\Delta\phi(I)/I$ by using the simple stripe-conductor geometry. The natural way to increase the slope would be to place the YIG film into a solenoid, however such a geometry is hardly feasible in the frame of planar technology.

The second prototype utilizes the propagation of MSSW. In this case the constant magnetic field is applied in y-direction perpendicular to the stripe (Fig. 1c). Therefore, to create the additional field profile δH we use a stripe conductor parallel to the YIG stripe. Consequently, in this case, the magnitude δH is z-independent and the phase accumulation length l can be chosen to be arbitrary without decreasing the current density I/w. The dependence $\Delta\phi(I)$ is again linear:

$$\frac{\Delta\phi(I)}{\delta H(I)} = -\frac{l}{L} \frac{\gamma^2 (H + 2\pi M_S)}{\omega_0^2 - \gamma^2 H (H + 4\pi M_S)} \quad . \tag{3}$$

The CPS prototype based on MSSW propagation contains the same YIG stripe and transducer structure as in the case of BVMSW. The only difference is that the stripe conductor (width 2 mm) was placed with its long axis parallel to the YIG stripe. Our measurements showed (Fig. 2a) that for MSSW CPS, in order to achieve the required phase shift of π, a current of only about 0.3 A is necessary. Note that this current value is three times smaller than in the BVMSW CPS due to the (three times) larger slope $\Delta\phi(I)$ (Fig. 2b). Again, ΔA was found to be less than 1 dB, like in the BVMSW configuration.

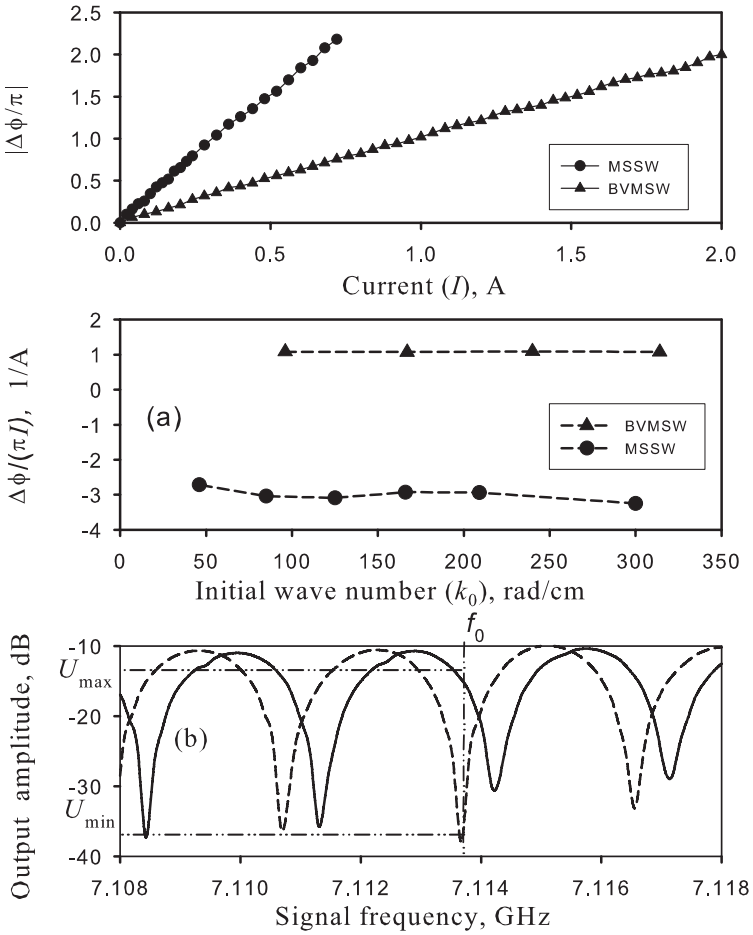

Fig. 2: (a) Absolute value of the additional phase shift vs. control current strength. Triangles: backward volume magnetostatic spin wave (BVMSW) phase shifter, initial wave number $k_0 = 90\,\mathrm{rad/cm}$; circles: magnetostatic surface spin wave (MSSW) phase shifter, $k_0 = 125\,\mathrm{rad/cm}$. (b) Additional phase shift per unit control-current strength as a function of k_0. Triangles: BVMSW, circles: MSSW. The lines are guides to the eye. (c) Interference amplitude as a function of frequency of the interferometer input signal. Solid line: no control current applied, dashed line: control current is 0.8 A.

Finally we demonstrate the feasibility of an interferometric NOT gate utilizing a CPS branch. For this purpose we use the same set-up as for the measurement of the additional phase shift $\Delta\phi$. Indeed the scheme represents a microwave interferometer, one branch being formed by a CPS, the other one by the reference circuit. The frequency dependence of the amplitude of the interferometer output signal in BVMSW configuration is shown in Fig. 2b. It was measured by applying a cw microwave signal to the interferometer input. As can be seen from the figure, the output signal can be switched from high to low by changing I for any specific frequency ω_0 (e.g. for $\omega_0/(2\pi) = f_0 = 7.1138\,\mathrm{GHz}$, as indicated in the figure), performing the NOT logic operation.

In conclusion, we experimentally demonstrated the possibility to implement the NOT logic gate by using the controllable propagation of spin waves. We also studied the performance of its main element - the current-controlled spin-wave phase shifter (CPS). Work is now in progress, where we intend to demonstrate the functionality of a spin wave XOR gate based on the same technology. The BVMSW XOR gate we are developing now differs from the implemented NOT gate only by the presence of a second spin wave CPS which is controlled in the same way, thus its functionality can be directly deduced from that of the NOT gate.

An obvious disadvantage of the fabricated CPSs is their macroscopic size. However, the size was entirely determined by the very simple fabrication methods. Utilizing a patterned permalloy film replacing the YIG stripe and a transducer type as introduced by Ref. [8], micrometer sized spin wave logic gates will be feasible taking advantage of a much smaller spin wave wavelength (several micrometers or even smaller than 1 µm) achievable in permalloy.

We acknowledge support by the Deutsche Froschungsgemeinschaft and the EU-STREP project MAGLOG.

References

[1] P. Gargini, W. Arden, J. Bruines, et al., Introduction to Highlights of the 2003 ITRS, Future Fab. Intl., **16**(18), (2004) [www.future-fab.com]; public.itrs.net.
[2] See e.g. K.J. Ebeling, *Integrated Optoelectronics*, Springer, Berlin-Heidelberg, (1993); A. Karim Mohammed, A.S. Abdul Awwall, *Optical computing: An introduction*, John Wiley, New York, (1992).
[3] See e.g. R.E. Cowburn, M.E. Welland, Science **284**, 289 (1999); D.A. Allwood, Gang Xiong, M.D. Cooke, C.C. Faulkner, D.A. Atkinson, N. Vernier, R.P. Cowburn, Science **287**, 1466 (2000); R. Richter, L. Bär, J. Wecker, G. Reiss, Appl. Phys. Lett. **80**, 1291 (2002).
[4] Y.K. Fetisov, C.E. Patton, IEEE Trans. Magn. **35** 1024 (1999).
[5] A.B. Ustinov, B.A. Kalinikos, Technical Physics Lett. **27**, 403 (2001).
[6] J. Eschbach, R. Damon, J. Phys. Chem. Solids **19**, 308 (1961).
[7] See e.g. S.O. Demokritov, A.A. Serga, A. André, V.E. Demidov, M.P. Kostylev, B. Hillebrands, A.N. Slavin, Phys. Rev. Lett. **93**, 047201 (2004).
[8] M. Bailleul, D. Olligs, C. Fermon, S.O. Demokritov, Europhys. Lett. **56**, 741 (2001).

6.4 Microwave assisted switching in $Ni_{81}Fe_{19}$ elements

H.T. Nembach, P. Martin Pimentel, S. Hermsdörfer, and B. Hillebrands[1]

Microwave assisted switching is a promising way to control the switching field in a magnetic switching process of small structured elements. Thirion et al. [1] first demonstrated the reduction of the switching field of single Cobalt nano-particles by applying short microwave pulses in a micro-SQUID experiment. For future industrial application it is of high importance to transfer this technique to patterned elements. A microwave field is expected to reduce the switching field in these elements even for the case in which the switching process is dominated by domain nucleation and growth. The magnetization vector oscillates with a large precession angle if the resonance condition is fulfilled. This reduces the effective energy barrier for domain nucleation, which otherwise cannot be crossed by thermal fluctuations alone.

We studied the quasi-static switching behavior of a $Ni_{81}Fe_{19}$ ellipsoid under the influence of a microwave field by magneto-optic Kerr effect magnetometry in longitudinal geometry. A picosecond diode laser with a wavelength of 407 nm and a pulse width of 73 ps is employed. The sample is placed on top of a impedance matched microwave antenna with a width of 430 µm. The magnetic material of the sample is facing the antenna to achieve a larger microwave field. The long axis of the ellipsoid is parallel to the quasi-static magnetic field generated by external coils, and the microwave field is oriented perpendicular to the quasi-static field in the plane of the element.

The scheme of the setup is shown in Fig. 1. An IFR 2032 signal generator with a frequency range of 10 kHz to 5.4 GHz is employed. The output signal is further amplified by 30 dB using an Aldetec microwave amplifier (0.5 – 2 GHz). The 10 MHz reference signal of the signal generator is used to synchronize the microwave field with the pulsed laser. The 10 MHz reference signal triggers a DG535 Stanford Research Systems Delay Generator, which sends a trigger signal with programmable delay to the pulsed laser.

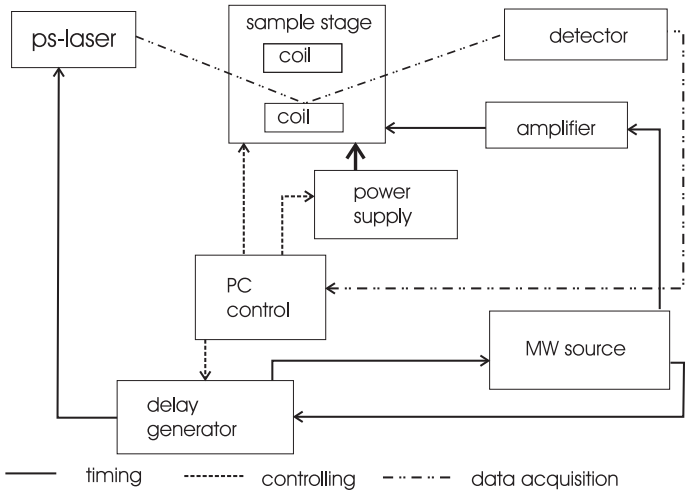

Fig. 1: Schematic diagram of the setup. Continuous lines show the flow of timing synchronization, the dash line the flow of controlling, and the dot-dash line the flow of the data acquisition.

[1] In collaboration with S.O. Demokritov, Institut für Angewandte Physik, Westfälische Wilhelms-Universität, Münster, Germany.

The element studied is an $Ni_{81}Fe_{19}$ ellipsoid with a size of $160 \times 80\,\mu m^2$. The ellipsoid was produced by UV-photo lithography on a glass substrate with a thickness of 100 µm.

The material is then deposited by molecular beam epitaxy (MBE). The thickness of the $Ni_{81}Fe_{19}$ layer is 10 nm. The Al capping layer to avoid oxidation is 2 nm thick. A magnetic field, which is applied during growth, induces an uniaxial anisotropy with the easy axis along the long axis of the ellipsoid. Time-domain ferromagnetic resonance experiments were done to characterize the sample. For a fixed microwave field in the range of 0.5 GHz to 2.6 GHz the oscillation of the magnetization is measured for different magnetic fields. The measurement for 2.6 GHz is made without the amplifier due to its limited frequency band. For each frequency the amplitude of the oscillations is determined as a function of the applied field. For frequencies above 1.1 GHz the obtained curve could be fitted using a Lorentzian line shape to determine the resonance field [2]. For lower frequencies of the microwave field the magnetic state of the ellipsoid becomes unstable and therefore no resonance field can be determined. The linewidth for 1.5 GHz is 15.9 Oe. The Kittel equation

$$\omega = \gamma\sqrt{(H_{\mathrm{stat}} + H_{\mathrm{uni}} + M_{\mathrm{s}}(N_{\mathrm{y}} - N_{\mathrm{x}}))(H_{\mathrm{stat}} + H_{\mathrm{uni}} + M_{\mathrm{s}}(N_{\mathrm{z}} - N_{\mathrm{x}}))} \quad , \tag{1}$$

with H_{uni} the uniaxial anisotropy field, can be simplified for $H_{\mathrm{stat}}, H_{\mathrm{uni}} \ll 4\pi M_{\mathrm{s}}$ to:

$$\omega = \gamma\sqrt{(H_{\mathrm{stat}} + H_{\mathrm{uni}} + M_s(N_{\mathrm{y}} - N_{\mathrm{x}}))(N_{\mathrm{z}} - N_{\mathrm{x}})M_{\mathrm{s}}} \quad . \tag{2}$$

This allows one to determine the saturation magnetization M_{s} =767.7 Oe from the slope of a linear fit of the squared frequency versus the static field. From the intersection of the fit with the *x*-axis the induced uniaxial anisotropy field $H_{\mathrm{uni}} = 12.7$ Oe is determined.

The switching behavior of the Permalloy element is studied by measuring hysteresis curves with an applied microwave field perpendicular to the quasi-static magnetic field. The frequency of the microwave field was varied in the range of 500 MHz to 2.0 GHz in steps of 100 MHz and the microwave power is increased from −5 dBm to 35 dBm for each frequency.

In Fig. 2 three hysteresis curves are shown, a curve without an applied microwave field, and two curves with a microwave frequency of 800 MHz and a power of 5 dBm and 35 dBm, respectively.

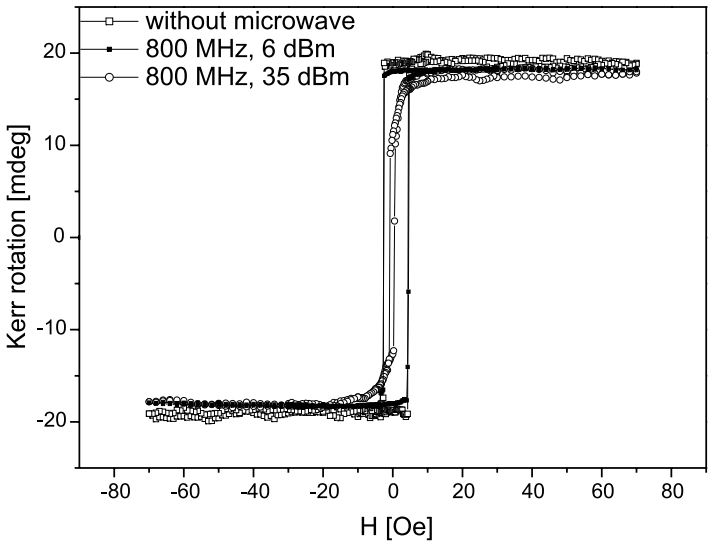

Fig. 2: The three shown hysteresis curves clearly demonstrate the reduction of the coercive field under the influence of a microwave field. The black curve was measured without a microwave field, the one with squares and the one with circles with a microwave frequency of 800 MHz and a power of 5 dBm and 35 dBm, respectively.

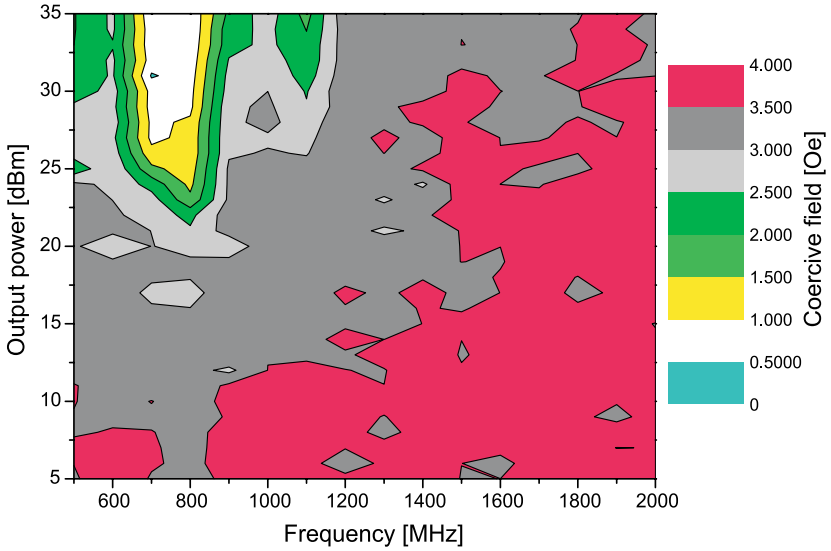

Fig. 3: The measured magnitude of the coercive field is shown for applied microwave fields in the range of 0.5 GHz to 2 GHz and a power between −5 dBm and 35 dBm. Clearly a strong reduction of the coercive field can be observed in the range between 600 MHz and 900 MHz

Clearly a reduction of the coercive field can be observed. In Fig. 3 the results of the switching experiment are summarized.

For microwave frequencies between 650 MHz and 900 MHz the strongest reduction of the coercive field is observed. To exclude the possibility that we observe a heat assisted switching process [3] due to the absorbed microwave power in the magnetic element measurements with variable duty-cycles were performed. Microwave pulses with a length of 106 ns and repetition rates between about 9.9 kHz and 909 kHz were applied. Three sets of measurements were made. For the first set the laser pulse was timed that it arrives directly before, for the second set during and for the last set directly after the microwave pulse. The microwave frequency was 1.0 GHz and the power was 30 dBm. The coercive field remained unchanged for all repetition rates and the different timing of the laser pulse. Therefore heating effects can be excluded as the reason for the reduction of the coercive field. In Fig. 4 three different hysteresis curves with the laser pulse applied before the microwave pulse are shown.

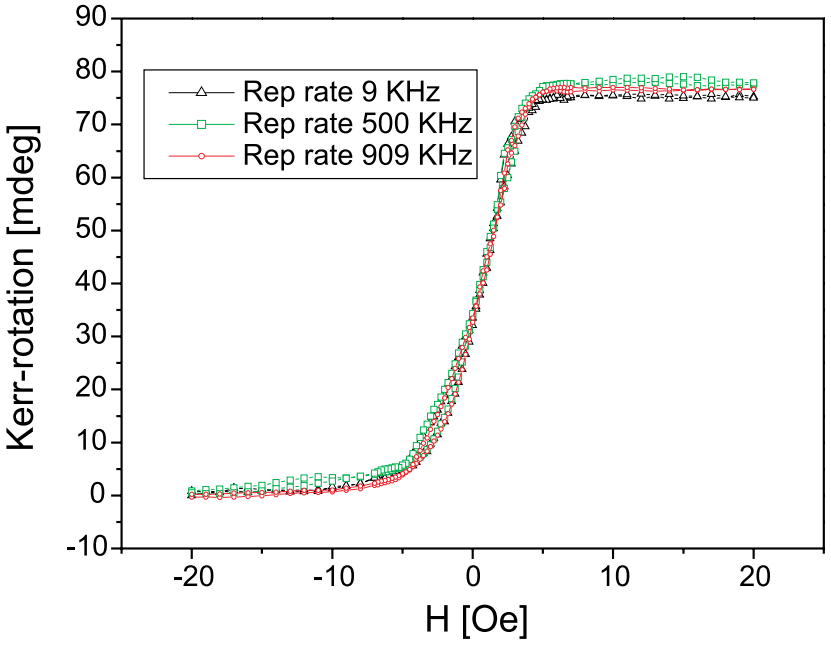

Fig. 4: Three hysteresis curves for different repetition rates are shown with the laser pulse timed before the 106 ns long microwave pulse. It is clearly seen that the coercive field remains unchanged.

The reduction of the coercive field under the influence of the microwave field can be explained by two different mechanisms. The most important one is the enhancement of domain nucleation by a microwave field. For the nucleation of a reversed domain an energy barrier has to be overcome. The height of this barrier is given by the domain wall energy. The precession of the magnetization lowers the effective height of the energy barrier and allows to overcome this barrier at smaller reversed fields. The resonance condition for a reversed magnetic field of 3 Oe is fulfilled for 900 MHz. The observed strong reduction of the coercive field between 700 MHz and 900 MHz is due to the fact that domains are favorably nucleated in areas with reduced internal fields, i.e. lower resonance frequency. The second, weaker mechanism is an enhanced growth of the reversed domain. This is due to the fundamental principle that every physical systems goes to the state with the lowest Gibb's free energy. The more microwave power is absorbed the higher becomes the entropy of the system and the lower the Gibb's free energy. Therefore a reversed domain, which is in resonance with the applied microwave field grows. This is the origin of the satellite for 1.1 GHz in Fig. 3. The reversed domain for an applied field of 3 Oe is in resonance with the microwave field.

In conclusion, we were able to demonstrate that the switching process of elements, which is dominated by domain nucleation and propagation, can be enhanced by applying a transversal microwave field.

This work is supported by the European Commission within the EU-RTN ULTRASWITCH (HPRN-CT-2002- 00318).

References

[1] C. Thirion, W. Wernsdorfer, D. Mailly Nature **2**, 524-7 (2003).
[2] B. Hillebrands, K. Ounadjela (Eds): Spin Dynamics in Confined Magnetic Structure II, Topics Appl. Phys. **87**, 27-59, Springer-Verlag Berlin Heidelberg (2003).
[3] A. Yamaguchi, S. Nasu, H. Tanigawa, T. Ono, K. Miyake, K. Mibu, T. Shinjo Appl. Phys. Lett. **86**, 012511 (2005).

6.5 All-optical probe of precessional magnetization dynamics in exchange biased bilayers

M.C. Weber, H.T. Nembach, and B. Hillebrands[1]

As data transfer rates increase in magnetic recording, the high frequency performance of related magnetic devices becomes increasingly important. Controlling magnetization dynamics requires the understanding and tuning of relaxation mechanisms, and reliable techniques are needed to observe such processes at high frequencies deep within the GHz regime.

Internal anisotropy pulse fields with rise times of the order of the exciting laser pulse duration can trigger coherent precessional dynamics in both ferromagnetic layers and exchange coupled bilayers [1–4]. Even fast spin reorientation processes in antiferromagnets have been excited [5]. Exploiting the possibility of real time spin precession measurements upon photoexcitation, the magnetic damping described by the phenomenological Gilbert damping parameter can be investigated. Recently, Silva et al. [6] have shown that nonlinear effects can play a crucial role in large angle precession dynamics. Even more recently, Nibarger et al. have demonstrated that both the small as well as the large angle free precession magnetization response to pulsed field excitations can be modelled with reasonable accuracy in terms of Landau-Lifshitz and Gilbert (LLG) damping [7]. At the same time, the good fits of LLG damping to large angle precession data indicate that there are no nonlinear damping effects present in these material systems. Many years ago, Patton et al. showed that the large angle precession response associated with domain wall motion in Permalloy films could also be modelled with the Landau-Lifshitz and Gilbert equation [8].

We address the dynamics of the exchange coupling in exchange bias systems with special emphasis on precessional magnetization dynamics due to intense picosecond laser excitations [9]. The optical approach allows for investigating the basic magnetization and relaxation dynamics in real time. The investigated magnetization dynamics is related to spin-lattice relaxation dynamics. An ideal test system for this purpose is an exchange bias bilayer system, since the exchange bias effect is known to depend strongly on temperature. Hence, the anisotropy in the system originating from the exchange bias effect can be switched on and off by a change in spin temperature. For recent reviews of the exchange bias effect see Ref. [10].

The investigated polycrystalline exchange bias samples have been prepared by UHV evaporation. As a growth template a 15 nm thick Cu buffer layer on top of a thermally oxidized Si substrate has been used. The bilayer itself consists of a 5 nm thick $Ni_{81}Fe_{19}$ (F) and a 10 nm thick $Fe_{50}Mn_{50}$ (AF) layer. The sample was covered with a 2 nm Cr cap layer. The sample was field-cooled to initialize exchange bias. For further details see Ref. [11]. The all-optical pump-probe experiments have been performed employing an amplified SESAM mode-locked Nd:YVO_4 laser oscillator [12] and pump power densities of about $0.3\,GW/cm^2$. Time resolution is achieved via a standard stroboscopic magneto-optical technique [4]. Hence, the probe beam is used to sense the induced changes of the magnetization of the F layer by means of the longitudinal magneto-optic Kerr effect.

Since the magnitude of the exchange bias field is inherently related to the temperature, the pump laser pulse is expected to serve as a local “heating” pulse influencing the exchange coupling across the F/AF interface [1, 3, 9]. Due to the excess energy of the spin system upon excitation, a pre-

[1] In collaboration with J. Fassbender, Institut für Ionenstrahlphysik und Materialforschung, Forschungszentrum Rossendorf, Dresden, Germany.

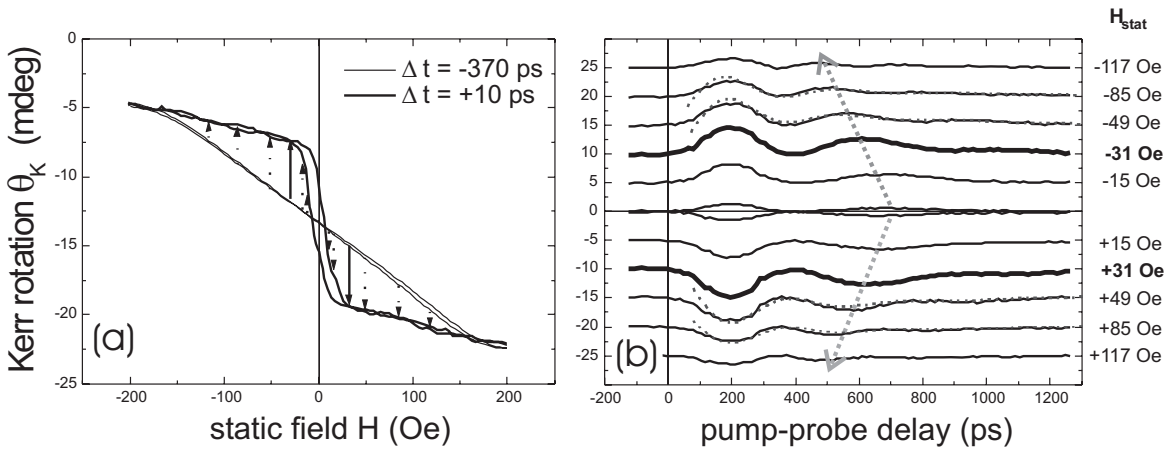

Fig. 1: (a) The anisotropy pulse field for the hard axis case. The dashed and full arrows indicate different magnitudes of the internal pulse field. The arrows display the magnitude and the onset of magnetization deflection. (b) Synopsis of the real time Kerr traces for applied field values as indicated in (a). The grey arrows highlight the field dependent oscillation period. Traces are vertically offset for clarity. The dashed lines (damped sinusoids) serve as guide to the eyes of the precessional dynamics.

cession of the magnetization of the ferromagnetic layer about the equilibrium orientation can be induced in both the easy axis (e.a.) and hard axis (h.a.) geometry [1, 9, 13]. Pump-probe measurements in the h.a. case reveal an additional important feature: The possibility not only to control the magnitude of the effective internal pulse field [3, 13] but to optically control the direction of the F layer magnetization deflection from the initial orientation. In Fig. 1a we exemplarily present transient reversal loops for the h.a. case with (delay 8 ps) and without (delay -370 ps) pump pulsed induced changes. The laser-induced transition from a typical h.a. reversal behavior to a nearly isotropic reversal behavior upon excitation can clearly be identified and can be interpreted as an effective internal pulse field acting on the F layer magnetization [3]. As suggested by the arrows in Fig. 1a, for negative applied field values, i.e., defining the initial state prior to the pump pulse arrival, the initial precessional deflection upon the internal pulse field should go “up”, whereas for positive applied fields the deflection should go “down”. Figure 1b summarizes the time-resolved Kerr measurements, providing clear evidence of optically controlled magnetization oscillations and, moreover, the possibility of controlling the initial deflection direction. A field-dependent oscillation period can be identified, as sketched by the grey dashed arrows in Fig. 1b which roughly follows a Kittel like behavior.

The possibility to control the strength of the internal pulse field in the h.a. geometry (see Fig. 1a) enables us to study the dependence of the effective damping on the angle of precession. The internal pulse field strength directly determines the initial magnetization deflection, and thus, the initial precessional cone angle. In the h.a. case the precessional cone angle should monotonously decrease for applied static fields larger than 31 Oe (see dashed arrows in Fig. 1a), i.e., the precessional motion for both small and large deflection angles can be studied. Assuming coherent rotation we can calculate the initial angle for the precessional response for each applied field value. Moreover, as described elsewhere [4], we can also deduce an effective damping for each recorded transient Kerr trace. Figure 2 summarizes the analysis of the dependence of the effective magnetic damping on the extracted precessional cone angle, which covers a range from 10 degree up to about 130 degree, e.g., small and intermediate angle as well as the onset of large angle precessional motion. Within the error bars the effective damping parameter stays constant, indicating that there are no or only minor nonlinear effects present in the measured intermediate angle range for the investigated bilayer system. A roughly 5% increase of the damping parameter is observed for the large angle

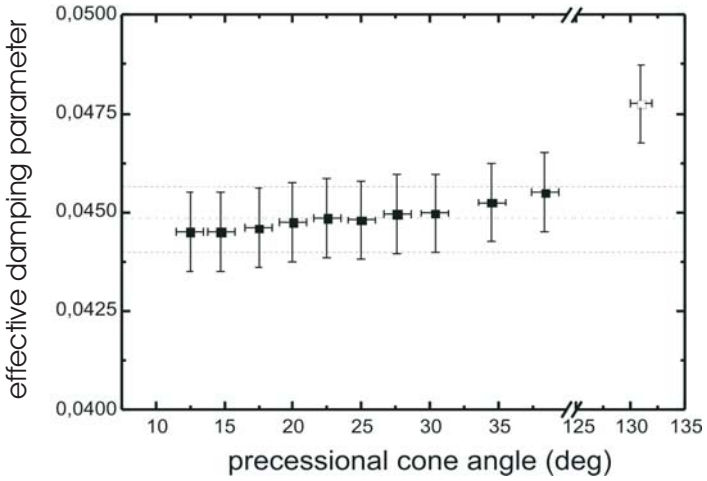

Fig. 2: Effective damping for the hard axis (full squares) and easy axis (open square) precession as a function of the precessional angle. Note the break in the abscissa.

e.a. precession compared to the values found in the h.a. geometry. Again, this minor increase suggests that both a small and a large angle precessional response to an internal pulse field excitation can be modelled with reasonable accuracy in terms of an effective Landau-Lifshitz and Gilbert damping. Presumably, nonlinear effects only play a crucial role in large angle precession or full switching events.

M.C.W. would like to acknowledge support by the Graduiertenkolleg 792 of the DFG. The work is supported by EU-RTN ULTRASWITCH (HPRN-CT-2002-00318) and EU-RTN NEXBIAS (HPRN-CT-2002-00296).

References

[1] G. Ju, A.V. Nurmikko, R.F.C. Farrow, R.F. Marks, M.J. Carey, B.A. Gurney, Phys. Rev. Lett. **82**, 3705 (1999).
[2] M. van Kampen, C. Jozsa, J.T. Kohlhepp, P. LeClair, L. Lagae, W.J.M. de Jonge, B. Koopmans, Phys. Rev. Lett. **88**, 227201 (2002).
[3] M.C. Weber, H.T. Nembach, J. Fassbender, J. Appl. Phys. **95**, 6613 (2004).
[4] M.C. Weber, H.T. Nembach, B. Hillebrands, J. Fassbender, J. Appl. Phys. **97**, 10A701 (2005).
[5] A.V. Kimel, A. Kirilyuk, A. Tsvetkov, R.V. Pisarev, Th. Rasing, Nature **429**, 850 (2004).
[6] T.J. Silva, P. Kabos, M.R. Pufall, Appl. Phys. Lett. **81**, 2205 (2002).
[7] J.P. Nibarger, R. Lopusnik, T.J. Silva, Appl. Phys. Lett. **82**, 2112 (2003).
[8] C.E. Patton, F.B. Humphrey, J. Appl. Phys. **37**, 4269 (1966).
[9] M.C. Weber, H.T. Nembach, S. Blomeier, B. Hillebrands, R. Kaltofen, J. Schumann, M.J. Carey, J. Fassbender, Euro. Phys. J. B **45**, 243 (2005).
[10] R.L. Stamps, J. Phys. D. **33**, R247 (2000); J. Nogués, I.K. Schuller, J. Magn. Magn. Mater. **192**, 203 (1999).
[11] A. Mougin, T. Mewes, M. Jung, D. Engel, A. Ehresmann, H. Schoranzer, J. Fassbender, B. Hillebrands, Phys. Rev. B **63**, R060409 (2001).
[12] www.lumera-laser.com
[13] M.C. Weber, H.T. Nembach, B. Hillebrands, J. Fassbender, Phys. Rev. B, submitted (2005) - cond-mat/0507475.

6.6 Laser induced precessional switching in exchange biased NiFe/FeMn bilayers

M.C. Weber and B. Hillebrands[1]

The optical control of magnetization dynamics is a key issue for future storage concepts such as heat assisted magnetic recording [1]. Moreover, a picosecond or even femtosecond control of the magnetization orientation allows for a real time investigation of ultrafast switching events. Laser pulse induced switching of the magnetization by short optical pulses has been shown in purely ferromagnetic films, e.g., in CoPt and GdFeCo systems by Guarisco et al. and Hohlfeld et al. [2,3]. However, the relaxation of the magnetization into a completely switched state upon ultrafast laser pulse excitation in these systems can last up to the nanosecond time scale.

On the picosecond time scale precessional spin dynamics promises a significant reduction of the switching time. The concept of precessional switching [4] of the magnetization vector within half a precession cycle upon transversal magnetic field pulses revealed switching times of about 205 ps [5]. Precessional motion of the magnetization has also been induced all-optically and observed in simple ferromagnets as well as exchange coupled bilayer systems [6, 7]. Internal anisotropy pulse fields triggered by the hot spin system upon photo-excitation with rise times of the order of the exciting laser pulses are responsible for the excitation of coherent precession of the magnetization vector [8], see also Chapter 6.5 in this Report. Exchange coupled bilayers comprising both a ferromagnetic and an adjacent antiferromagnetic layer represent an ideal test material system for optically induced magnetization dynamics due to their inherent spin temperature dependence [9].

An all-optical real-time technique, which is employed in our experiments to trace the optically induced spin dynamics, strongly relies on the concept of stroboscopic imaging. A well defined, i.e. reproducible, magnetization distribution prior to the photo-excitation is a prerequisite of such a time domain technique. However, a complete switching event represents a non-reversible process. Hence a well designed preset step prior to a pump-pulse triggered switching event is necessary to trace any time evolution. For this purpose we developed a special sample geometry and combined the well known field pulse assisted magnetization dynamics with an all-optical pump-probe experiment. The investigated exchange bias bilayer system consists of a 5 nm thick $Ni_{81}Fe_{19}$ (F) and a 10 nm thick $Fe_{50}Mn_{50}$ (AF) layer, MBE grown on a Si substrate and a 250 nm thick Cu buffer.

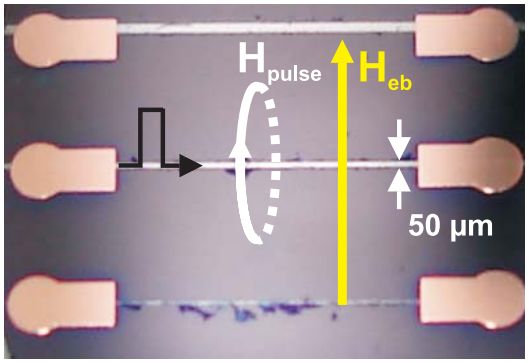

Fig. 1: NiFe/FeMn striplines. The exchange bias easy axis is indicated by the direction of the exchange bias field H_{eb}. The Cu buffer layer of the exchange bias stripline carries the current pulse creating a magnetic preset field pulse H_{pulse} perpendicular to the stripline axis. Shown are three striplines of varying width. Used in the experiments is the central, 50 µm wide stripline.

[1] In collaboration with J. Fassbender, Institut für Ionenstrahlphysik und Materialforschung, Forschungszentrum Rossendorf, Dresden, Germany; Nano+Bio Center TU Kaiserslautern, Germany.

Optical lithography and wet chemical etching have been used to pattern a 50 µm wide and about 3 mm long stripline into the film (see Fig. 1). A magnetic field cooling procedure was used to set the initial exchange bias direction as indicated in Fig. 1. In addition Cu bond pads have been evaporated through shadow masks which partially cover the exchange bias stripline system. The stripline system, which has a microwave transmission bandwidth of about 3 GHz, is connected to a DG 535 pulse generator via semi-rigid coaxial cables and bond contacts. The thick Cu buffer allows for a good electric transport of an 800 ns long current pulse which creates a magnetic field pulse of about 100 Oe perpendicular to the stripline axis and directly beneath the F/AF bilayer (see Fig. 1).

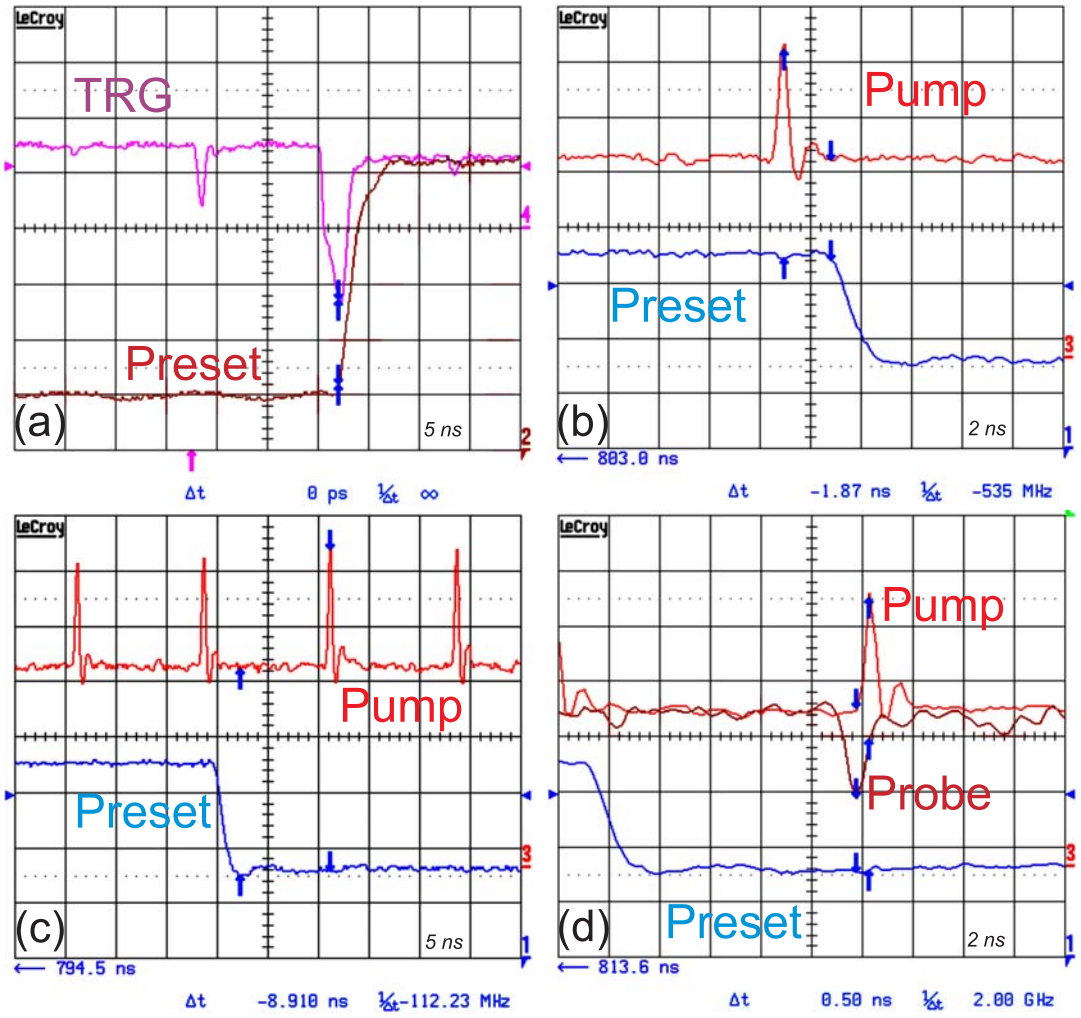

Fig. 2: Timing sequence of the all-optical field pulse assisted switching experiment recorded by a 4-channel LeCroy WavePro 7100A digital oscilloscope and fast photodiodes (τ_{rise} =200 ps). The small arrows represent the timing cursors of the oscilloscope. (a) Synchronization of the laser generated low jitter ($\sigma \leq 10$ ps) trigger signal (TRG) and the magnetic field pulse generated by the DG 535 pulse and delay generator which creates the preset field in the exchange bias stripline. (b) Synchronization of the 800 ns and 100 Oe preset field pulse through the 50 µm stripline and the pump laser pulse (repetition time 12.5 ns) thermally suppressing the exchange bias coupling. (c) Timing window of the preset pulse and the pump laser pulse which triggers the switching event itself by a hot F/AF interfacial spin gas. (d) Synchronization of the preset pulse, the pump pulse which induces spin dynamics in the NiFe/FeMn bilayer system and the weak probe pulse sensing the pump induced precessional dynamics, respectively. The probe laser pulse runs at a repetition time of 10 µs to prevent any crosstalk with the preset phase and is able to scan the time evolution starting from about 500 ps before the pump pulse inducing the switching dynamics.

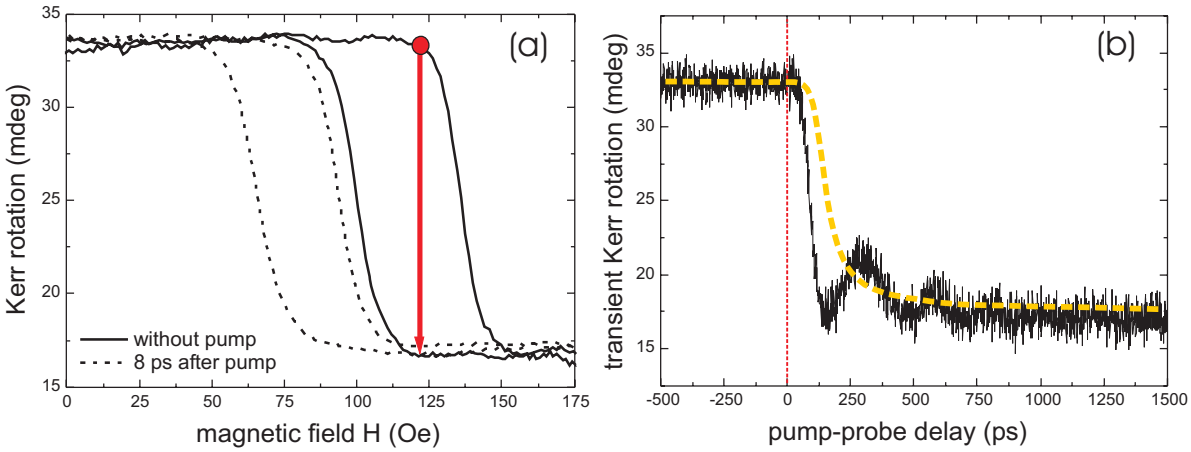

Fig. 3: All-optical, magnetic field assisted switching of the magnetization of the NiFe layer of the NiFe/FeMn exchange bias bilayer system. (a) Optimum working point for a maximum deflection away from the initial equilibrium orientation defined by the exchange bias effect. The possible maximum deflection of the magnetization at a field of about 123 Oe is highlighted by dynamic hysteresis loops recorded for both an absent pump pulse and for a pump-probe delay of 8 ps. The magnetization becomes bistable upon photo-excitation and allows for a direct observation of the induced precessional dynamics.(b) Ultrafast laser pulse induced precessional switching of the NiFe layer of the exchange biased stripline system. A strongly precessional relaxation into the switched state can clearly be resolved. Moreover, a switching time of about 500 ps can be deduced. A numerical solution of LLG-KP equation matching the experimental conditions is shown as well.

If one is able to thermally suppress the F/AF exchange coupling on the picosecond time scale, the external magnetic field pulse can serve as a magnetic preset field reproducibly setting the exchange bias equilibrium orientation prior to the optical pump-probe event. It has been shown that intense picosecond laser pulses of a 8 ps duration and a pulse energy of 15 nJ, focused to a spot size of about 35 µm in diameter, can reduce the exchange bias anisotropy significantly [9]. The pump-probe experiments have been performed with a standard picosecond pump-probe setup with a spatial resolution of about 30 µm. In order to successfully resolve any laser pulse induced switching dynamics of the NiFe/FeMn stripline system, one has to synchronize all the present signals, both the optical and the electrical ones. Figure 2 summarizes the timing sequence of all signals. Four signals have to be synchronized: A laser inherent electric low jitter trigger signal (TRG) triggers the preset field pulse (Fig. 2a). The optical pump pulses within the duration of the preset field pulse (Fig. 2b) enable us to preset the exchange bias field direction via the previously reported mechanism of the picosecond optical control of the F/AF exchange coupling [9]. After relaxation of the preset field the next optical pump pulse arriving on the F/AF stripline (Fig. 2c) can induce precessional magnetization dynamics due to the excess energy present at the F/AF interface upon photo-excitation [6]. The time delayed, properly synchronized weak optical probe pulse is able to trace the pump pulse induced magnetization dynamics of the NiFe layer of the exchange bias system (Fig. 2d). The probe pulse has been reduced in repetition rate by a pulse picker unit.

After properly optimizing all parameters, we could indeed observe laser-pulse induced precessional switching dynamics of the NiFe layer of the NiFe/FeMn exchange bias stripline in easy axis geometry. A summary is given in Fig. 3. The chosen initial condition (see Fig. 3a) prior to the pump pulse becomes bistable upon photo-excitation and, thus, allows for a large angle deflection away from the initial equilibrium orientation. The real time observation of the precessional character of the observed laser pulse induced switching can clearly be seen in Fig. 3b. Moreover, a switching time of about 500 ps can be deduced. The observation of a full switching event is fur-

ther supported by comparing the maximum transient Kerr amplitude with the quasi-static easy axis hysteresis loop prior to the pump pulse.

The observed ultrafast precessional switching in the NiFe/FeMn exchange biased bilayer system can be discussed within the framework of the Landau-Lifshitz and Gilbert equation (LLG). Ruigrok et al. suggested the so-called LLG-Klaasen-van-Peppen equation (LLG-KP) to model thermally assisted magnetization switching events [10]. The LLG-KP equation couples precessional dynamics with thermal fluctuations [11]. Hence, the laser pulse induced dynamics can be described by

$$\frac{1}{\beta H_k}\frac{dm}{dt} = (h+m)(1-m^2) - \frac{m}{C}, \tag{1}$$

with a dimensionless m representing the averaged magnetization of the F layer. $\beta = \alpha\gamma/1+\alpha^2$ relates to the effective damping, which has previously been deduced [8]. $h = H/H_k$ describes the ratio between the applied field and the anisotropy field, in our case $H_k = H_{\mathrm{eb}}$. The thermal stability factor $C = k_B T/KV$ can be incorporated taking a typical spin temperature increase [9] upon photo-excitation, typical activation volumes of granular magnetic media [12] and magneto-optically deduced exchange bias anisotropy constants into account. Figure 3b displays a numerical solution of the LLG-KP equation which matches the experimental parameters and yields a qualitative agreement with the experimental time domain data. Hence, there is clear evidence of laser pulse induced precessional switching in exchange coupled bilayers with temperatures involved far below the Curie temperatures of typical ferromagnets.

M.C.W. would like to acknowledge support by the Graduiertenkolleg 792 of the DFG. The work is supported by EU-RTN ULTRASWITCH (HPRN-CT-2002-00318) and EU-RTN NEXBIAS (HPRN-CT-2002-00296).

References

[1] D. Weller, A. Moser, IEEE Tans. Magn. **35**, 4423 (1999).
[2] D. Guarisco, R. Burgermeister, C. Stamm, F. Meier, Appl. Phys. Lett. **68**, 1729 (1996).
[3] J. Hohlfeld, Th. Gerrits, M. Bilderbeek, Th. Rhasin, H. Awanom, N. Ohta, Phys. Rev. B **68**, 012413 (2001).
[4] M. Bauer, J. Fassbender, R.L. Stamps, B. Hillebrands, Phys. Rev. B **61**, 3410 (2000).
[5] Th. Gerrits, H.A.M. van den Berg, J. Hohlfeld, L. Bär, Th. Rasing, Nature **418**, 509 (2002).
[6] G. Ju, A.V. Nurmikko, R.F.C. Farrow, R.F. Marks, M.J. Carey, B.A. Gurney, Phys. Rev. Lett. **82**, 3705 (1999).
[7] M. van Kampen, C. Jozsa, J.T. Kohlhepp, P. LeClair, L. Lagae, W.J.M. de Jonge, B. Koopmans, Phys. Rev. Lett. **88**, 227201 (2002).
[8] M.C. Weber, H. Nembach, B. Hillebrands, J. Fassbender, J. Appl. Phys. **97**, 10A701 (2005).
[9] M.C. Weber, H. Nembach, B. Hillebrands, J. Fassbender, IEEE Trans. Magn. **41**, 1089 (2005).
[10] J.J. Ruigrok, J. Magn. Soc. Japan **25**, 313 (2001).
[11] K.B. Klaasen, J.C.L. van Peppen, IEEE Trans. Magn. **37**, 1537 (2001).
[12] A.M. de Witte, K. O'Grady, G.N. Goverdale, R.W. Chantrell, J. Magn. Magn. Mater. **88**, 183 (1990).

6.7 Real time evidence of two-magnon relaxation in exchange coupled bilayers

M.C. Weber, H.T. Nembach, and B. Hillebrands[1]

There have been several types of experiments probing the fundamental speed limit of precessional magnetization and switching dynamics in magnetic thin film materials by application of subnanosecond magnetic field pulses. In a series of recent efforts, such field pulses are generated by various electronic and optoelectronic means in high-speed microwave compatible coplanar transmission lines [1, 2]. On the other hand, photoexcitation of a magnetic medium can create hot, non-equilibrium spins. Thus, the magnetic response is modulated at a microscopic level on a picosecond or even subpicosecond time scale [3]. It has been found that short laser pulses are capable of launching internal anisotropy pulse fields with rise times on the order of the exciting laser pulse duration, i.e., triggering coherent precessional dynamics in ferromagnetic layers and exchange coupled bilayers [4–6], see also Chapter 6.5 in this Report. This optical approach raises the prospect of investigating fundamental spin dynamics and spin damping phenomena in the time domain with the system driven by the absorbed photons. The physical mechanisms contributing to magnetic damping are still rather unclear or incomplete. Different extrinsic and intrinsic contributions, such as multi-magnon processes in general, in particular two-magnon-scattering and magnon-phonon relaxation mechanisms have been proposed and studied in detail recently [7].

As a specific material test system we have investigated an exchange biased bilayer system. For a recent review of the exchange bias effect see Ref. [8]. Exploiting the well known spin temperature dependence of the unidirectional exchange bias anisotropy, a transient internal field pulse with a picosecond rise time [9] is induced, triggering a precessional response of the ferromagnetic layer of the exchange coupled bilayer. The dependence of the effective magnetic damping on the exchange bias field magnitude is investigated. The interfacial exchange coupling might contribute as an additional damping channel, hence, exchange bias can effectively modify the relaxation of photoexcited spins.

The investigated polycrystalline exchange biased bilayers have been sputter deposited on glass substrates at Hitachi-GST. As a growth template a Ta/Cu buffer has been used. The exchange bias system itself consists of a 3 nm thin $Co_{90}Fe_{10}$ ferromagnetic (F) layer on top of an antiferromagnetic (AF) $Ir_{25}Mn_{75}$ layer. Samples with different IrMn thicknesses have been prepared. The samples are finally covered with a Ta cap layer to prevent oxidation. The time-resolved experiments have been performed stroboscopically with a standard pump-probe setup utilizing a picosecond mode-locked laser source. Details of the setup can be found elsewhere [9, 10]. Real time measurements of the magnetization precession have been carried out by keeping the applied static magnetic field constant and varying the pump-probe time delay continuously. The proportionality of the employed longitudinal Kerr effect to the in-plane magnetization component make the transient experiments sensitive to changes in the direction of the magnetization, e.g., due to coherent precessional motion.

Exchange bias bilayers with different thicknesses of the AF layer allow for a direct control of the magnitude of the exchange bias shift field H_{eb}. Easy axis Kerr magnetometry measurements reveal

[1] In collaboration with J. Fassbender, Institut für Ionenstrahlphysik und Materialforschung, Forschungszentrum Rossendorf, Dresden, Germany; M.J. Carey, Hitachi Global Storage Technologies, San Jose Research Center, San Jose, USA.

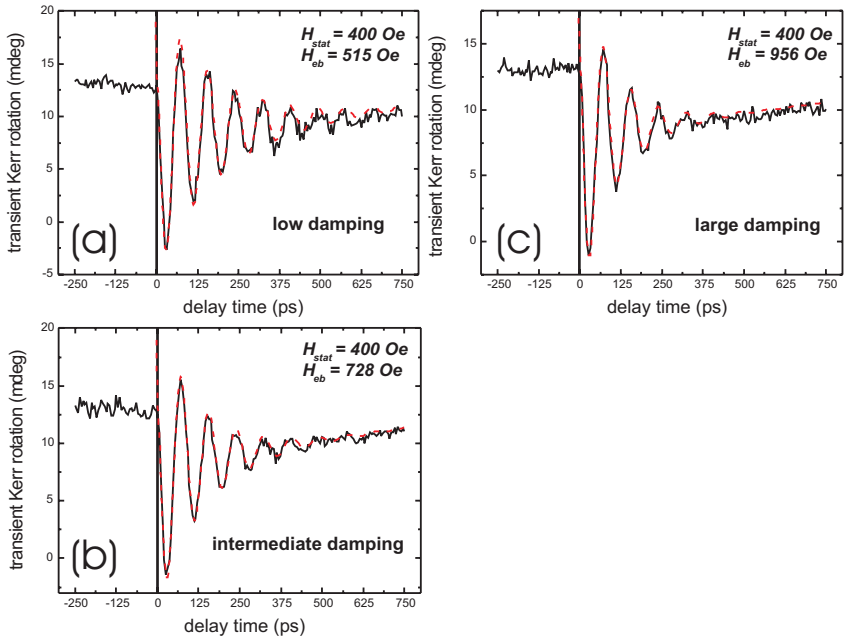

Fig. 1: Exchange bias field dependence of the photoinduced easy axis precession of the F layer magnetization ($H_{\mathrm{stat}} = 400\,\mathrm{Oe}$). (a) low, (b) intermediate and (c) large damping. The dashed lines show fits based on the Landau-Lifshitz and Gilbert model [11, 12] yielding effective decay rates.

that the exchange bias field can be tuned over a large range of values, thus, the dynamic properties of the bilayer system can be measured depending on the magnitude of the exchange bias field. Here, the exchange bias field dependence of the effective damping of the magnetization precession upon photoexcitation has been studied. Real time Kerr rotation traces as a function of pump-probe delay for different IrMn thicknesses have been recorded, which reveal coherent precessional dynamics with frequencies up to 12.2 GHz. The applied static field of 400 Oe was kept constant for all samples. Figure 1 exemplarily shows precession traces for three different exchange bias field magnitudes. It is evident that the decay rate is a function of the the exchange bias field. The effect damping parameter has been extracted from the decay rate of the precession traces using a simple approximation for the in-plane precession angle [11, 12]. The effective damping parameter is deduced for each IrMn thickness, i.e., for different exchange bias field values. Figure 2 summarizes the analysis and yields the exchange bias field dependence of the effective damping and relaxation rate. The effective Gilbert parameter clearly increases with the exchange bias field magnitude.

The photomodulation of the exchange bias field leads to a change of the equilibrium orientation of the F layer magnetization. A transient internal field is launched triggering precessional magnetization dynamics due to a torque following the initial “kick” on the F layer magnetization upon photoexcitation [5, 13]. The induced precession rings down according to a characteristic relaxation parameter. The increasing dependence of the Gilbert damping on the exchange bias field strength is consistent with results of the NiFe/NiO exchange bias system from Ju et al. [4]. During the coherent magnetization rotation part the magnetic energy of the ferromagnetic system might be dissipated through the interfacial exchange coupling between ferromagnetic and antiferromagnetic spins. The latter provide an additional channel of dissipation into the AF lattice system [12]. Since the measurements are performed at room temperature, thermal fluctuations are present in the polycrystalline bilayer system. If the spin fluctuations of the antiferromagnetic grains at the F/AF interface reach precessional frequencies of the F layer, there can be an energy dissipative coupling mediated via the interfacial exchange coupling [4].

Fluctuations of the effective internal field due to fluctuations of the coupling at the crucial F/AF interface can account for a linear increase of the effective damping with an increasing exchange bias field. Since the exchange bias field scales linearly with the F/AF coupling a stronger interfacial

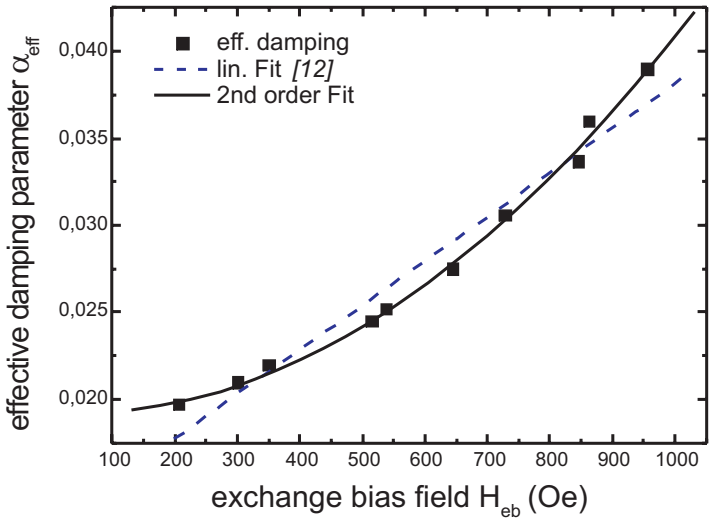

Fig. 2: Exchange bias field dependence of the extracted effective damping parameter of the photoexcited precession. The dashed line displays a simple model from Ref. [12]. The solid line reveals a fingerprint of two-magnon relaxation, i.e., $\alpha_{eff} \propto H_{eb}^2$.

exchange coupling increases the total energy dissipation, evidently quite dramatically, leading to the experimentally found increase of the effective damping.

Moreover, the data in Fig. 2 are well described by a second order fit (see solid line in Fig. 2). The deduced relaxation rate depends on the square of the exchange bias field magnitude, i.e., $\alpha_{eff} \propto H_{eb}^2$. This is a strong fingerprint of two-magnon scattering in exchange coupled bilayers [14,15]. Hence, there is real time evidence of two-magnon scattering involved in the spin damping processes of exchange coupled bilayers. Photoexcited coherent magnons can effectively scatter at local inhomogeneities due to fluctuations of the F/AF exchange coupling caused by interface roughness. Thus, local fluctuations of the interfacial exchange coupling, i.e., fluctuations of the exchange bias field, provide an extra means for dissipation compared to a single F layer. A possible contribution to the measured damping due to the granular microstructure of the polycrystalline exchange bias system in terms of dephasing cannot be neglected, but is small due to the controlled and very narrow grain size distribution.

M.C.W. would like to acknowledge support by the Graduiertenkolleg 792 of the DFG. The work is supported by EU-RTN ULTRASWITCH (HPRN-CT-2002-00318) and EU-RTN NEXBIAS (HPRN-CT-2002-00296).

References

[1] Th. Gerrits, H.A.M. van den Berg, J. Hohlfeld, L. Bär, Th. Rasing, Nature **418**, 509 (2002).
[2] H.W. Schumacher, C. Chappert, P. Crozat, R.C. Sousa, P.P. Freitas, J. Miltat, J. Fassbender, B. Hillebrands, Phys. Rev. Lett. **90**, 017201 (2003).
[3] E. Beaurepaire, J.-C. Merle, A. Daunois, J.-Y. Bigot, Phys. Rev. Lett. **76**, 4250 (1996).
[4] G. Ju, A.V. Nurmikko, R.F.C. Farrow, R.F. Marks, M.J. Carey, B.A. Gurney, Phys. Rev. Lett. **82**, 3705 (1999).
[5] M. van Kampen, C. Josza, J.T. Kohlhepp, P. LeClair, L. Lagae, W.J.M. de Jonge, B. Koopmans, Phys. Rev. Lett. **88**, 227201 (2002).
[6] M.C. Weber, H. Nembach, S. Blomeier, B. Hillebrands, R. Kaltofen, J. Schumann, M.J. Carey, J. Fassbender, Euro. Phys. J. B **45**, 243 (2005).
[7] D.L. Mills, S.M. Rezende, in *Spin Dynamics in Confined Magnetic Structures II*, edited by B. Hillebrands and K. Ounadjela (Springer, Berlin, 2003).
[8] R.L. Stamps, J. Phys. D. **33**, R247 (2000).
[9] M.C. Weber, H. Nembach, J. Fassbender, J. Appl. Phys. **95**, 6613 (2004).
[10] M.C. Weber, H. Nembach, B. Hillebrands, J. Fassbender, IEEE Trans. Magn. **41**, 1089 (2005).
[11] T.J. Silva, C.S. Lee, T.M. Crawford, C.T. Rogers, J. Appl. Phys. **85**, 7849 (1999).

[12] M.C. Weber, H. Nembach, B. Hillebrands, J. Fassbender, J. Appl. Phys. **97**, 10A701 (2005).
[13] M.C. Weber, H. Nembach, B. Hillebrands, J. Fassbender, Phys. Rev. B, submitted (2005) - cond-mat/0507475.
[14] S.M. Rezende, A. Azevedo, M.A. Luena, F.M. de Anguiar, Phys. Rev. B **63**, 214418 (2001).
[15] R. Arias, D.L. Mills, Phys. Rev. B **60**, 7395 (1999).

6.8 Spin-lattice relaxation phenomena in manganite $La_{0.7}Sr_{0.3}MnO_3$ thin films

M.C. Weber and B. Hillebrands[1]

Significant research effort has been focused on ultrafast magnetization and demagnetization dynamics in the recent years. An all-optical technique employing short laser pulses may be of interest, as field pulse assisted magnetization switching cannot be faster than a magnetization precession cycle [1], see Chapter 6.5. However, a special demagnetization mechanism is required - an optical pulse can barely change the magnetization directly. Ultrafast magnetization dynamics has been studied in ferromagnetic [2, 3] and various other material systems [4, 5]. On the other hand, colossal magnetoresistive manganites are promising candidates for ultrafast spin control due to coupled spin, charge, orbital and lattice degrees of freedom [6].

Perovskite manganites exhibit an insulator to metal transition usually related to a para-ferromagnetic phase transition at the Curie temperature. The origin of ferromagnetism is double-exchange interaction [7] yielding a strong correlation between magnetization and charge transport properties. Photoinduced effects for the ferromagnetic phase of manganites have been previously studied by conventional pump-probe spectroscopy [8–10]. However, the evaluated time scales for the demagnetization dynamics were based on changes in optical absorption. Thus, spin channels, such as spin-lattice relaxation, have not been discerned in the absorption changes. In the present work, magnetization dynamics in epitaxial $La_{0.7}Sr_{0.3}MnO_3$ (LSMO) films was investigated by time-resolved magneto-optics where the Kerr rotation was employed as a means of probe of magnetization [11]. Special emphasis was put on the determination of the spin-lattice relaxation time, a key quantity to answer the question about the fundamental speed limit of spin manipulation in this material. Ferromagnetic epitaxial perovskite LSMO films were grown in Göttingen on MgO(100) substrates by a metalorganic aerosol deposition technique [12, 13]. The time-resolved measurements have been performed employing a picosecond all-optical pump-probe setup [14]. A pulse picker reduces the repetition rate of the system to 1 MHz to avoid any dc lattice heating effects. In order to investigate spin dynamics in the time domain, a quasi-static hysteresis loop is sensed by a probe pulse with a fixed time delay to the excitation pulse. It then reflects the magnetic parameters, such as the spin temperature present for a given time delay.

First, the longitudinal moment of a 76 nm thick LSMO film as a function of temperature was measured in Göttingen in a SQUID magnetometer. Figure 1 summarizes the SQUID measurements for a temperature range from 4 to 375 K. The LSMO film exhibits a ferromagnetic-paramagnetic phase transition at a Curie temperature of $T_C = 357$ K. The inset of Fig. 1 shows the temperature dependence of the coercivity in the temperature range of interest. Next we addressed the question whether it is possible to induce a spin-lattice non-equilibrium close to the ferromagnetic-paramagnetic phase transition in thin LSMO via a short picosecond photoexcitation.

We deduced the time evolution of the Kerr amplitude at zero applied field of the recorded transient hysteresis loops (see inset Fig. 2a) for pump-probe delay times up to 4000 ps. The time evolution of the Kerr amplitude at zero applied field will be further denoted as the time evolution of the remanence, thus directly reflecting the ferromagnetic order as well as the spin temperature of the

[1] In collaboration with V. Moshnyaga and K. Samwer, I. Physikalisches Institut, Universität Göttingen, Göttingen, Germany.

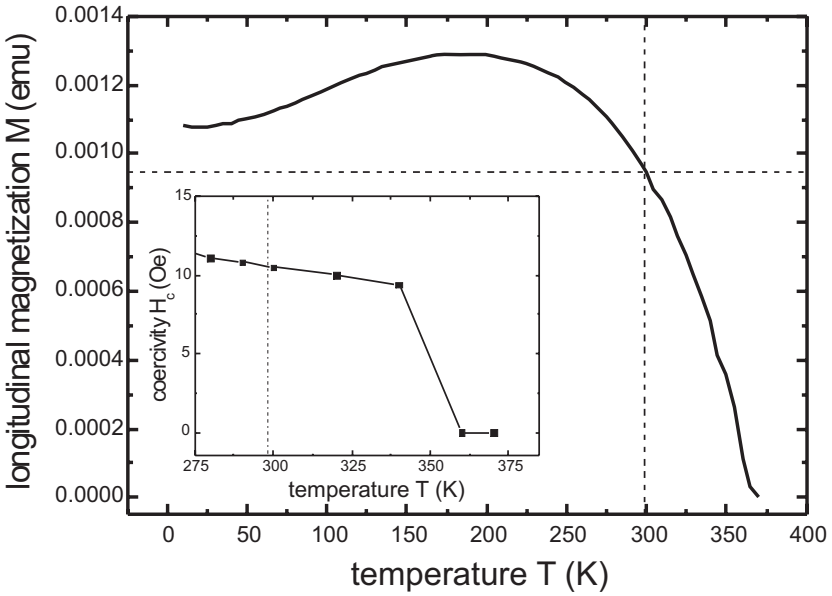

Fig. 1: Temperature dependence of the longitudinal magnetic moment of the 76 nm thin LSMO film, measured by SQUID. The dashed lines indicate room temperature and the room temperature moment, respectively. The inset shows the temperature dependence of the coercivity in the range of interest. A coercivity of about 11 Oe at room temperature indicates a good epitaxial film quality and the absence of structural pinholes.

LSMO film. The time evolution of the remanence exemplarily presented in Fig. 2 for a pump pulse energy of 27.5 nJ clearly indicates a collapse of the magnetic order within the excitation duration, followed by a spin and lattice thermalization based relaxation back to its initial value. The overall equilibrium relaxation dynamics can be well described by the time evolution of the lattice temperature (diffusive processes) [15]. If one zooms around zero delay, as shown in Fig. 2b, one can clearly see a strong deviation from the diffusive background after application of the pump pulse. A second order exponential recovery fit to the data (see solid line in Fig. 2b) reveals two different relaxation times $\tau_1 = 130$ ps and $\tau_2 = 550$ ps. Moreover, by subtracting the diffusive background (τ_2) from the measured data we can clearly resolve the transition between two distinct recovery regimes of the ferromagnetic order at $\tau_{sl} = 250$ ps (see inset of Fig. 2b).

The existence of two distinct relaxation regimes during the measured demagnetization and remagnetization process can be understood considering a strong spin-lattice non-equilibrium upon photoexcitation. Thermalization of the spin and phonon systems lasting from the low picosecond up to the nanosecond time scale dominate the measured time evolution of the remanence. An increase in spin temperature upon excitation is followed by a spin-lattice non-equilibrium and subsequently by spin-lattice thermalization mediated via spin-orbit coupling. However, spin-orbit coupling in perovskite manganites is small [11], which is consistent with the negligible magnetocrystalline anisotropy found in the investigated film. Thus, the weak spin-orbit coupling in LSMO accounts for the deviation from the diffusive background (see Fig. 2b) which can be attributed to spin-lattice relaxation dynamics [11].

The data analysis yields a spin-lattice relaxation time window from $\tau_1 = 130$ ps up to $\tau_{sl} = 250$ ps - an upper limit for the relaxation process. This spin-lattice time window is about a factor of 2-3 larger than values reported from Vaterlaus et al. [16] and Guarisco et al. [17] for typical ferromagnets and at least one order of magnitude larger than those reported for Ni [3], where spin-orbit coupling is large compared to LSMO. For pump-probe delay times larger than τ_{sl}, where spin and lattice temperatures are in equilibrium, heat diffusion processes dominate the recovery of the

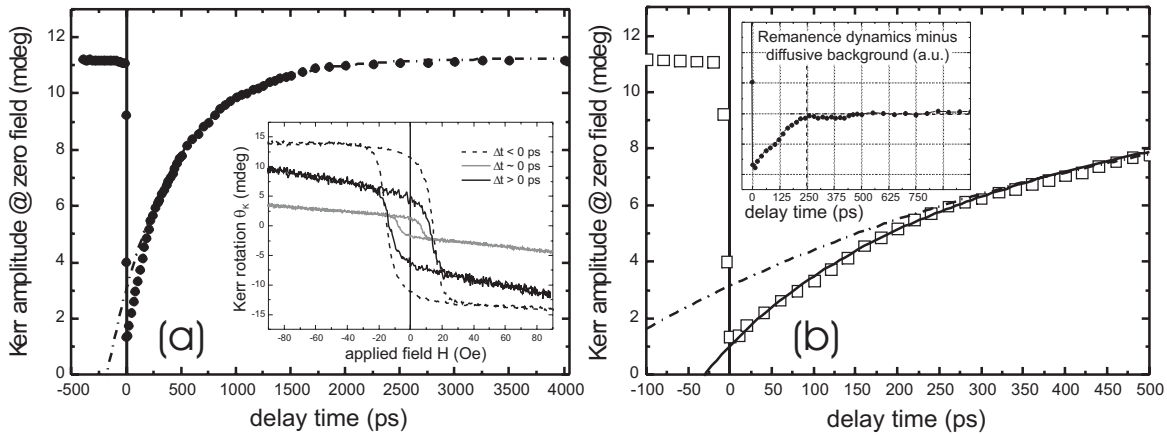

Fig. 2: (a) Time evolution of the remanence for a pump pulse energy of 27.5 nJ. The inset shows three hysteresis loops for a negative (<0), positive (>0) and zero pump-probe delay. (b) Enlarged section of (a) showing the spin-lattice thermalization regime. The solid line represents a second order exponential recovery ($\tau_1 = 130$ ps and $\tau_2 = 550$ ps). The inset shows a strong deviation from the diffusive background.

LSMO film. Comparing the time evolution of the spin temperature with the heat diffusion equation [15] one can determine consistently both the spin-lattice time and the heat diffusion properties of the LSMO film, which determine the ultimate speed of recovery of the ferromagnetic order. Taking into account the temperature dependence of the longitudinal magnetization from Fig. 1 and the time evolution of remanence from Fig. 2 one can calibrate the spin temperature evolution. Since the pump spot is much larger than the film thickness one can solve the heat flow equation assuming that heat diffusion perpendicular to the film surface dominates. Moreover, assuming that the pump pulse leads to a Gaussian temperature profile at τ_{sl} the spin temperature increase [14],

$$\Delta T\,(t \geq \tau_{sl}) = \frac{\lambda_0 \cdot \Delta T_{max}}{\sqrt{\pi \cdot D \cdot t \;+\; \lambda_0^2}} \qquad , \tag{1}$$

can be compared to the experimental spin temperature evolution with a thermal diffusion length λ_0 and the diffusivity D. Figure 3a shows the spin temperature evolution together with a fit to Eq. (1), which yields $\lambda_0 = 25$ nm and $D = 3.85 \cdot 10^{-6}\,\mathrm{m^2/s}$. Considering a composition weighted specific heat of $C = 1.2 \cdot 10^6\,\mathrm{J/m^3K}$ one can deduce a heat conductivity perpendicular to the film surface of $K = 4.7\,\mathrm{W/mK}$, which agrees well with recently published values [18]. However, it is considerably lower than in typical metals. Since Eq. (1) only fits for pump-probe delay times larger than 250 ps, this value corresponds to the spin-lattice relaxation time which is consistent with the results found for the time evolution of the ferromagnetic order. Again, a strong deviation from the diffusive relaxation can be identified for delays less than 250 ps. The deduced spin-lattice time window was found to be independent of the energy of the applied pump pulses (see Fig. 3b) which suggests the fundamental nature of the observed long spin-lattice relaxation time in LSMO thin films.

In summary, we have observed spin-lattice relaxation phenomena in thin epitaxial manganites by time-resolved magneto-optics. A nearly complete breakdown of the ferromagnetic order could be induced and observed on the picosecond time scale. A spin-lattice relaxation time window from 130 ps up to about 250 ps was deduced which is considerably slower compared to normal ferromagnets. The origin lies in the weak spin-orbit coupling present in perovskite manganites. A-site doping of thin LSMO as well as tuning of mechanical strain, thereby modifying the spin-

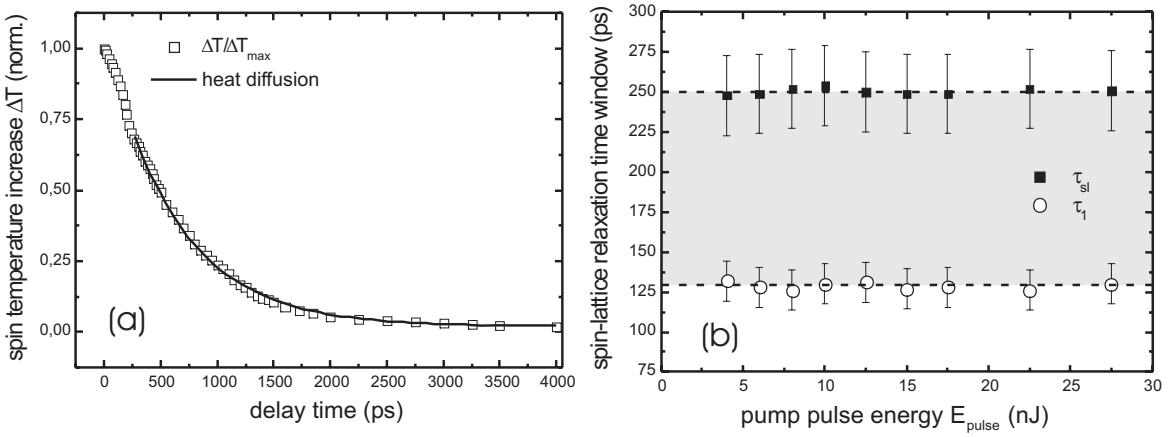

Fig. 3: (a) Time evolution of the spin temperature upon excitation with a fit to Eq. (1) yielding a spin-lattice relaxation time of about $\tau_{sl} = 250\,\text{ps}$. (b) Pump pulse energy dependence of the spin-lattice relaxation time window (τ_1, τ_{sl}), which stays constant within the experimental error.

orbit coupling, seem to be relevant to control the fundamental spin-lattice relaxation time of an photoexcited LSMO spin state. A clear separation of spin-lattice relaxation dynamics and diffusive heat flow upon photoexcitation could be observed.

M.C.W. would like to acknowledge support by the Graduiertenkolleg 792 of the DFG. The work is supported by EU-RTN ULTRASWITCH (HPRN-CT-2002-00318) and EU-RTN NEXBIAS (HPRN-CT-2002-00296).

References

[1] M. Bauer, R. Lopusnik, J. Fassbender, B. Hillebrands, Appl. Phys. Lett. **76**, 2758 (2000).
[2] E. Beaurepaire, J.-C. Merle, A. Daunois, J.-Y. Bigot, Phys. Rev. Lett. **76**, 4250 (1996).
[3] B. Koopmans, M. van Kampen, J.T. Kohlhepp, W.J.M. de Jonge, Phys. Rev. Lett. **85**, 844 (2000).
[4] J.M. Kikkawa, D.D. Awschalom, Phys. Rev. Lett. **80**, 4313 (1998).
[5] T. Kise, T. Ogasawara, M. Ashida, Y. Tomioka, M. Kuwata-Gonokami, Phys. Rev. Lett. **85**, 1986 (2000).
[6] Y. Tokura, Y. Tomioka, J. Magn. Magn. Mater. **200**, 1 (1999).
[7] C. Zener, Phys. Rev. **81**, 440 (1951); P.W. Anderson, H. Hasegawa, Phys. Rev. **100**, 675 (1955); P.-G. de Gennes, Phys. Rev. **118**, 141 (1960).
[8] K. Matsuda, A. Machida, Y. Moritomo, A. Nakamura, Phys. Rev. B **58**, 4203 (1998).
[9] A.I. Lobad, R.D. Averitt, C. Kwon, A.J. Taylor, Appl. Phys. Lett. **77**, 4025 (2000).
[10] M. Sasaki, G.R. Wu, W.X. Gao, H. Negishi, M. Inoue, G.C. Xiong, Phys. Rev. B **59**, 12425 (1999).
[11] T. Ogasawara, M. Matsubura, Y. Tomioka, M. Kutawa-Gonokami, H. Okamoto, Y. Tokura, Phys. Rev. B **68**, R180407 (2003).
[12] S.A. Köster, V. Moshnyaga, K. Samwer, O.I. Lebedev, G. van Tendeloo, O. Shapoval, A. Belenchuk, Appl. Phys. Lett. **81**, 1648 (2002).
[13] V. Moshnyaga, I. Khoroshun, A. Sidorenko, P. Petrenko, A. Weidinger, M. Zeiler, B. Rauschenbach, R. Tidecks, K. Samwer, Appl. Phys. Lett. **74**, 2842 (1999).
[14] M.C. Weber, H. Nembach, B. Hillebrans, J. Fassbender, IEEE Trans. Magn. **41**, 1089 (2005).
[15] J.H. Bechtel, J. Appl. Phys. **43**, 1585 (1975).
[16] A. Vaterlaus, T. Beutler, F. Meier, Phys. Rev. Lett. **67**, 3314 (1991).
[17] D. Guarisco, R. Burgermeister, C. Stamm, F. Meier, Appl. Phys. Lett. **68**, 1729 (1996).
[18] A. Salazar, A. Oleaga, D. Prabhakaran, Int. J. Thermophys. **25**, 1269 (2004).

6.9 Tunneling of spin waves through a mechanical gap in an yttrium iron garnet waveguide

A.A. Serga, M.P. Kostylev, T. Schneider, and B. Hillebrands[1]

We have shown recently that a region of a lowered magnetic field can act as a tunnel barrier for a propagating dipolar dominated spin wave [1]. The material system was a spin-wave waveguide made from a thin yttrium iron garnet (YIG) film. Here we report, that tunneling of spin waves may also take place through a narrow mechanical gap cut into the YIG waveguide.

The spin-wave waveguide was fabricated by chemical etching of a YIG film of 6 µm thickness with a width of 1.5 mm and a length of 10 mm. The mechanical gap was realized by a transverse slot of 20 µm width. The waveguide was magnetized along its longitudinal axis. Backward volume magnetostatic spin waves (BVMSW) with a carrier frequency of $\omega/2\pi = 7.125$ GHz were excited in the waveguide using a 25 µm wide microstrip antenna. The spin wave propagation was observed using the space- and time-resolved Brillouin light scattering (BLS) spectroscopy technique.

Figure 1 shows the experimental results for two different values of the magnetizing field: $H = 1835$ Oe and $H = 1846$ Oe. The data are normalized to the maximum value in each picture. The larger magnetic field corresponds to a larger carrier wavenumber of the spin wave packet incident on the gap.

As expected the main part of the waves is reflected from the gap and forms a standing wave. A small part of the wave energy tunnels through the gap and forms a propagating transmitted wave. One can see in Fig. 1 that the amplitude of the transmitted pulse is smaller for short carrier wavelengths and larger for long carrier wavelengths.

We also investigated the trapping of a BVMSW packet between two identical parallel gaps of 20 µm width with a separation of 1 mm. Figure 2 shows the results for a magnetic field strength of $H = 1839$ Oe. As before the data are normalized to the maximum value in each picture.

As Fig. 2 shows, a portion of the spin wave is trapped between the two gaps for more than 500 ns.

In a theoretical description the tunneling of a dipole-dominated long-wavelength spin wave through a region of width w with magnetic properties different from the rest of the film can be described by an integral equation commonly used in quantum mechanics to describe scattering of a probability wave from a potential well. If we neglect effects of the static demagnetization field at the edges of the gap, the effective potential shape of the mechanical gap is described well by a rectangular shape. Then the integral equation takes a very simple form:

$$m(z) = \delta\nu \int_0^w G_{\mathrm{exc}}(z-z')m(z)dz' + \exp(\mathrm{i}k_0 z) \quad . \tag{1}$$

Here z is the coordinate in the direction of spin wave propagation, k_0 is the wavenumber of the incident wave, m is the out-of-plane component of the dynamic magnetization of the wave, and G_{exc} is the Green's function of excitation of a spin-wave by a line source with infinitesimally small width in z-direction

$$G_{\mathrm{exc}}(x) = 2\pi\mathrm{i}\exp(\mathrm{i}k_0|x|) + \mathrm{Re}[\exp(\mathrm{i}k_0|x|)E_1(\mathrm{i}k_0|x|)] \quad , \tag{2}$$

[1] In collaboration with R.L. Stamps, the University of Western Australia, Perth, Australia.

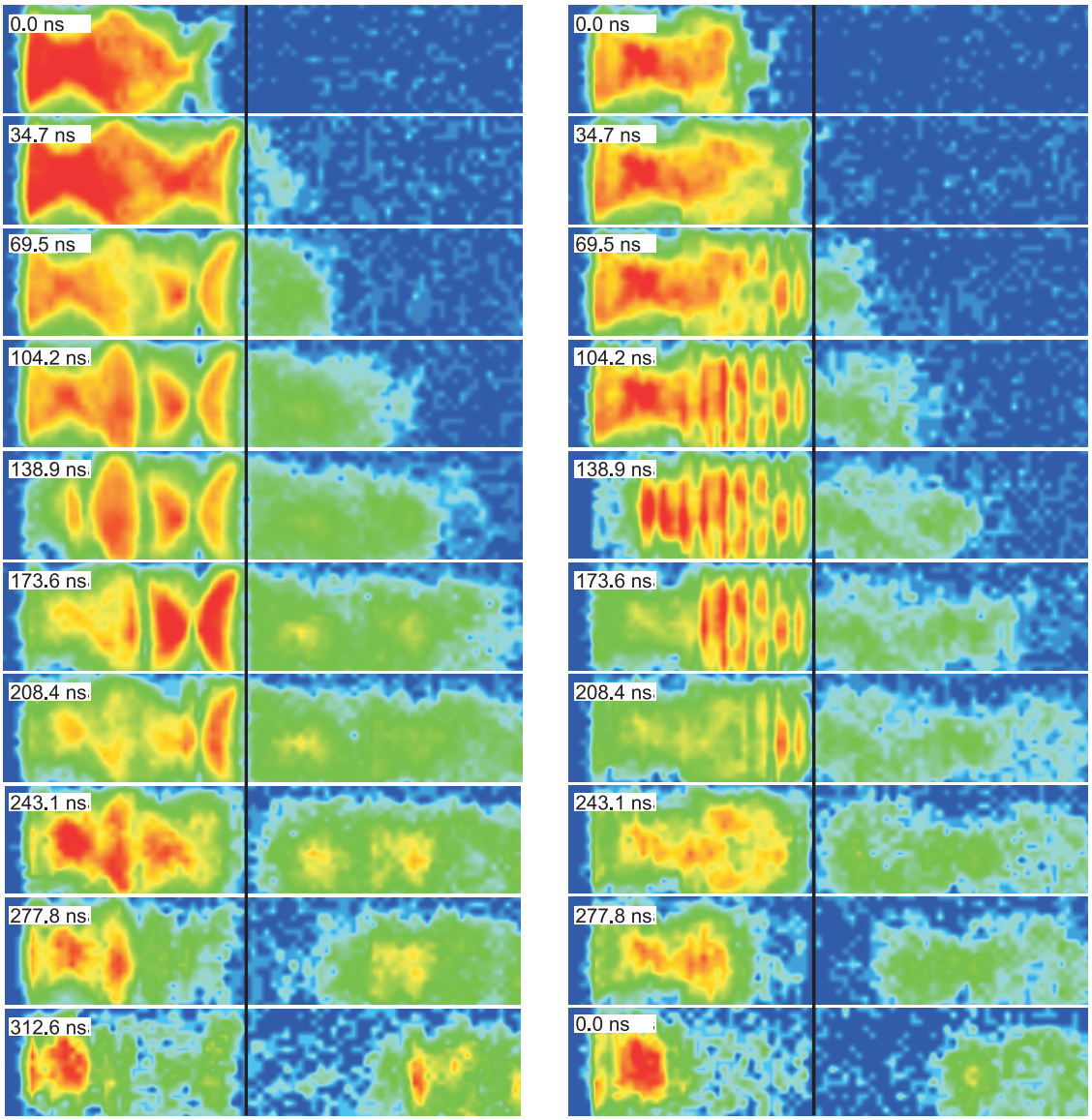

Fig. 1: Tunneling of a spin wave through a mechanical gap. The position of the gap is indicated by the black line. Left column: $H = 1835\,\mathrm{Oe}$, right column $H = 1846\,\mathrm{Oe}$.

where $E_1(x) = \int_x^\infty \frac{\exp(-t)}{t} dt$ denotes the exponential integral.

The height of the effective potential is $\delta\nu$. It is determined by the jump of the microwave magnetic permittivity at the boundaries of the rectangular-shaped barrier

$$\delta\nu = \kappa_w^{-1} - \kappa_0^{-1} \quad , \tag{3}$$

where κ_w is the value of the diagonal component of the microwave permittivity tensor inside the well (see, e.g., [2]), and κ_0 denotes its value outside. The diagonal component of the tensor is a function of the frequency of magnetization precession ω, the local static magnetic field H and the local saturation magnetization of the material M:

$$\kappa = \frac{MH}{H^2 - (\omega/\gamma)^2} \quad , \tag{4}$$

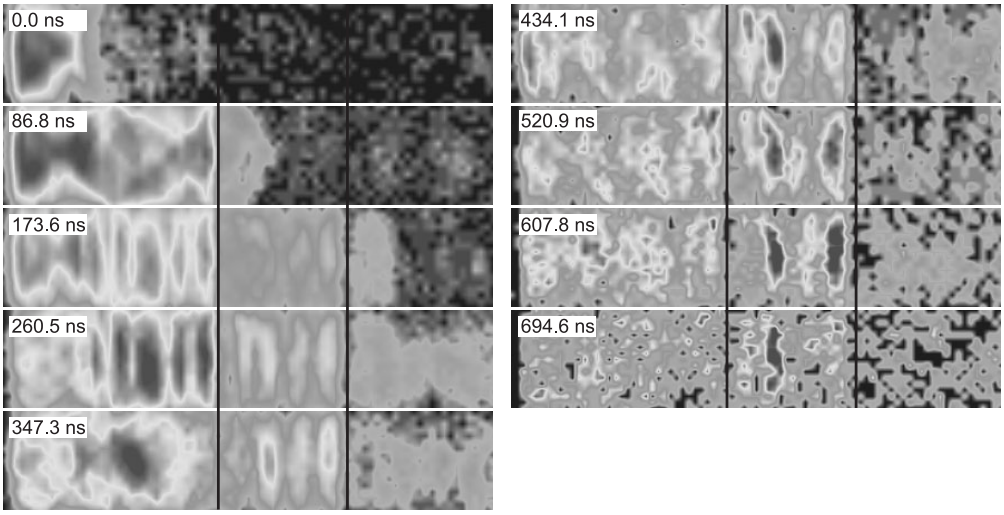

Fig. 2: Propagation of a spin wave through two mechanical gaps, indicated by the black lines. A portion of the spin wave is trapped between the two gaps for more than 500 ns. $H = 1839$ Oe.

where $\gamma/2\pi = 2.8$ MHz/Oe is the gyromagnetic ratio. The mechanical gap is a region with vanishing saturation magnetization, hence $\delta\nu = -\infty$. (The minus sign appears because a BVMSW exists in the frequency/static-field range, where $\omega/\gamma > H$ and hence the permittivity is negative.) Thus the tunneling of a spin wave trough a mechanical gap represents a tunneling through a potential well of infinite height. Tunneling of a dipolar-dominated spin-wave through a well of finite length and of infinite height is possible, because the physical mechanism which underlies the effect is the coupling of both the wave incident onto the barrier and the wave reflected back with the transmitted wave by their dipole fields. The dipole fields of waves in front of the gap are long range and can reach through the vacuum gap and excite a traveling wave on the other side of the barrier.

Eq. (1) has a simple solution for small carrier wavenumbers of the incident wave, i.e. $k_0 w \ll 1$:

$$m(z) = -f(k_0)\frac{\int_0^w G_{\mathrm{exc}}(z-z')dz'}{\int_0^w \int_0^w G_{\mathrm{exc}}(z-z')dz'dz} \quad . \tag{5}$$

Here

$$f(k_0) = 2\frac{\sin(k_0 w)}{k_0}\exp(\mathrm{i}k_0 w/2) \quad , \tag{6}$$

and all the integrals are calculated analytically. For an arbitrary value of wavenumber of the incident wave Eq. (1) can be easily solved numerically.

Since, while deriving Eq. (1), we assumed that the amplitude of the incident wave is equal to unity, the amplitude of the wave well behind the barrier (Eq. (5)) represents the transmission coefficient of the mechanical gap. The amplitude of the quantity $m(z) - \exp(\mathrm{i}k_0 z)$ well in front of the barrier is the reflection coefficient.

The results of our calculation of the transmission coefficient as a function of k_0 for two different gap widths are shown in Fig. 3. Results of the exact numerical solution of (Eq. (1)) and of the approximate calculation (Eq. (5)) are shown. As seen from the figure, the phase ϕ of the transmission coefficient varies practically linearly with k_0. The behavior of the amplitude T is more complicated and depends on the gap width. For the wider gap it quickly decreases with k_0, whereas for the narrower gap there is a range of small k_0, where T is nearly constant.

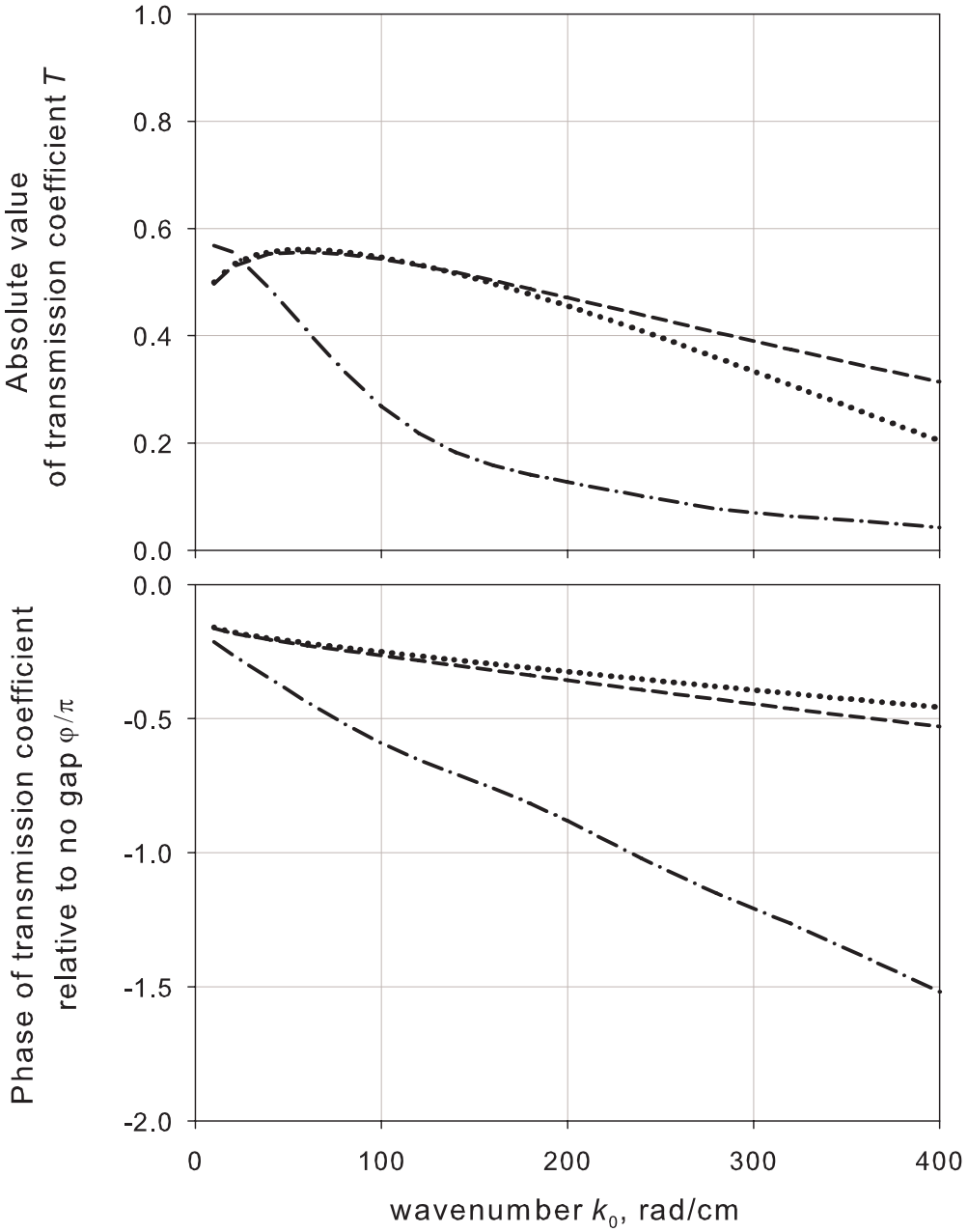

Fig. 3: Amplitude (upper panel) and phase (lower panel) of the transmission coefficient for mechanical gaps of different widths. Dashed line: $w = 20\,\mu m$, exact numerical calculation, dotted line: same width, approximate analytical calculation (5), dash-doted line: $w = 100\,\mu m$, exact numerical calculation. Film thickness is $6\,\mu m$.

It is well known, that, in order to transmit a pulse through a transmission line without distortion, two conditions must be fulfilled. The amplitude of the complex transmission coefficient in the operational frequency range must be frequency independent and the phase of the coefficient must vary linearly with the frequency. Once both conditions are fulfilled, the slope of $\phi(\omega)$ represents the delay time of the signal in the line $\tau = \partial\phi/\partial\omega$. The dispersion of BVMSW in the range $k_0 L \ll 1$, where L is the film thickness, is practically linear. The slope is the BVMSW group velocity in a homogeneous film:

$$V = \frac{\partial\omega}{\partial k} \approx -\gamma MHL/[4\sqrt{H(H+4\pi M)}] \quad . \tag{7}$$

Thus for BMSW tunneling $\tau = |\frac{\partial\phi}{V\partial k_0}|$. We estimated $\partial\phi(k_0)/\partial k_0$ for the experimental case $w = 20\,\mu\text{m}$, $L = 6\,\mu\text{m}$ from the result of the exact numerical calculation of the dependence (Fig. 3, dashed line). We found that $\partial\phi/\partial k = 0.0028\,\text{cm}$. The group velocity of the BVMSW mode outside the gap is $2.7 \cdot 10^6\,\text{cm/s}$, which gives the advance time of the signal tunneled through the gap compared to the time of propagation of BVMSW through the same distance in the film $|V|/w - \tau = 1\,\text{ns}$.

Thus, if the signal is carried by a long wavelength dipole-dominated BVMSW it should be possible to transmit it without large distortion though a prohibited zone with increased velocity of propagation. The experimental result in Fig. 1 shows that a BVMSW pulse can really maintain its shape while tunneling through the mechanical gap.

As an endnote to the theoretical discussion, since the theory described above allows one to calculate both the complex transmission and the reflection coefficients of the gap, it is apparently not difficult to construct a transfer matrix of the gap. Once this is done, the calculation of the unstable bound states in Fig. 2 is straightforward. This work is now in progress.

In conclusion, we have experimentally demonstrated the possibility of tunneling of dipole-dominated spin waves through a mechanical gap and of forming unstable “bound states” between two parallel gaps. Theoretically the phenomenon is described by an integral equation similar to the one commonly used for the description of scattering of the probability wave from a potential well.

Support by the Deutsche Forschungsgemeinschaft is gratefully acknowledged.

References

[1] S.O. Demokritov, A.A. Serga, A. André, V.E. Demidov, M.P. Kostylev, B. Hillebrands, Phys. Rev. Lett. **93**, 047201 (2004).
[2] A.G. Gurevich, G.A. Melkov, *Magnetization oscillations and waves, CRC Press.*

B. Nonlinear Wave Effects

6.10 Formation of quasi-solitons in transverse confined media

A.A. Serga, M.P. Kostylev, and B. Hillebrands[1]

We report on the observation of a new type of a stable, two-dimensional nonlinear spin wave packet propagating in a magnetic waveguide structure and suggest a theoretical description of our experimental findings. Stable two-dimensional spin wave packets, so-called spin wave bullets, were previously observed, however solely in long and wide samples of a thin ferrimagnetic film of yttrium-iron-garnet (YIG) [1–3], that were practically unbounded in both in-plane directions compared to the lateral size of the spin wave packets and the wavelength of the carrier spin wave. In a waveguide structure, where the transverse dimension is comparable to the wavelength, up to day only quasi one-dimensional nonlinear spin wave objects were observed, which are spin wave envelope solitons. Here a typical system is a narrow ($\simeq 1-2\,$mm) stripe of a YIG ferrite film [4,5]. Both for solitons and bullets the spreading in dispersion is compensated by the longitudinal nonlinear compression. Concerning the transverse dimension, solitons have a cosine-like amplitude distribution due to the lateral confinement in the waveguide, whereas bullets show a transverse nonlinear instability compensating pulse widening due to diffraction and leading to transverse confinement.

Here we report on the observation of a new stable spin wave packet propagating along a waveguide structure, for which both transversal instability and interaction with the side walls of the waveguide are important.

The experiments were carried out using a longitudinally magnetized long YIG film stripe of 2.5 mm width and 7 µm thickness. The magnetizing field was 1831 Oe. The spin waves were excited by a microwave magnetic field created with a microstrip antenna of 25 µm width placed across the stripe and driven by electromagnetic pulses of 20 ns duration at a carrier frequency of 7.125 GHz. As is well known the backward volume magnetostatic spin wave (BVMSW) [6] excited in the given experimental configuration is able to form both envelope solitons and bullets [4], depending on the geometry. The spatio-temporal behavior of the traveling BVMSW packets was investigated by means of space- and time-resolved Brillouin light scattering spectroscopy [7].

The obtained results are demonstrated in Fig. 1 where the spatial distributions of the intensity of the spin wave packets are shown for given moments of time. The spin wave packets propagate here from left to right and decay in the course of their propagation along the waveguide because of magnetic loss. The left set of diagrams corresponds to the linear case. The power of the driving electromagnetic wave is 20 mW. The right set of diagrams corresponding to the nonlinear case was collected for a driving power of 376 mW.

Differences between these two cases are clearly observed. First of all the linear spin wave packet is characterized by a cosine-like lateral profile while the cross section of the nonlinear pulse is sharply modified relative to the linear case and has a pronounced bell-like shape. Second, the intensity of the linear packet decays monotonically with time while the intensity of the nonlinear packet initially increases because of its strong transversal compression (see the second diagram from the top in Fig. 1).

[1] In collaboration with A.N. Slavin, Department of Physics, Oakland University, Rochester, Michigan, U.S.A. and S.O. Demokritov, Institut für Angewandte Physik, Westfälische Wilhelms-Universität, Münster, Germany.

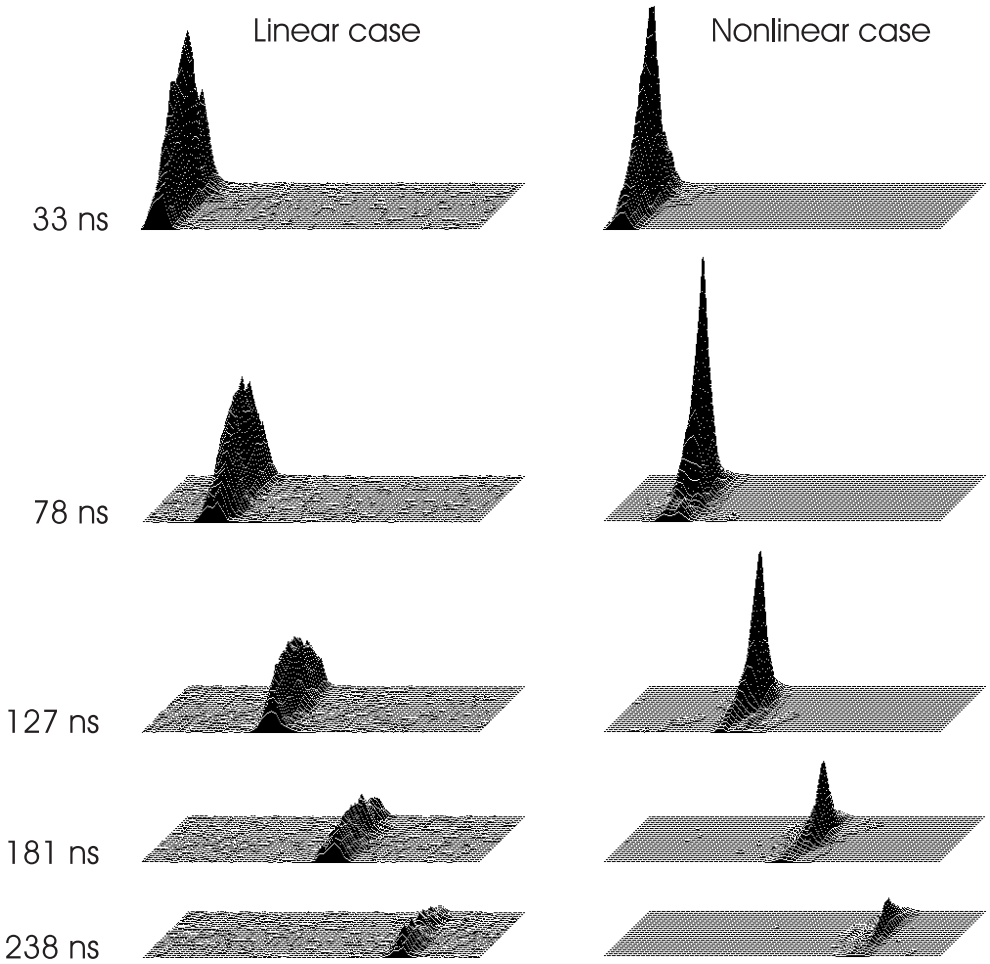

Fig. 1: Bullet formation in the transversally confined yttrium-iron-garnet film.

Both of these nonlinear features provide clear evidence for the development of a transversal instability and bullet formation. It is interesting that the bell-like cross-section shape survives even at the end of the propagation distance when the pulse intensity decreases more than ten times and the nonlinear contribution to the spin wave dynamics should considerably diminish.

In order to interpret the experimental result we have assumed that the development of nonlinear instabilities in a laterally confined medium is strongly modified by a quantization of the spin wave spectrum. That is why we have transformed the two-dimensional Nonlinear Schrödinger Equation traditionally used for the analysis of bullet dynamics [4] into a system of coupled equations for amplitudes of the spin wave width modes. The specific form of the discrete set of these orthogonal modes is defined by the actual boundary conditions at the lateral edges of the stripe. We developed a two-dimensional theory of linear spin-wave dynamics in magnetic stripes. As an important outcome we found that the Guslienko-Slavin's effective boundary condition [8] for dynamic magnetization at the stripe lateral edges, being initially derived for spin waves with vanishing longitudinal wavenumbers, is also valid in the case of propagating width modes with non-vanishing longitudinal wavenumbers. The effective boundary condition shows that the magnetization vector at the lateral stripe edges is highly pinned, that means that the amplitude of dynamic magnetization practically vanishes at the edges. For simplicity it is even possible to consider the stripe width modes to be totally pinned at the stripe lateral edges. As seen from Fig. 1 this conclusion is in a good agreement with the experiment.

The analysis of the system of nonlinear equations derived from the Nonlinear Schrödinger Equation shows that the formation of the two-dimensional waveform can be considered as an enrichment of the spectrum of the width modes. The partial waveforms carried by the modes have the same carrier frequencies equal to that of the initial signal and the carrier wave numbers which satisfy the dispersion relations for the modes. In the linear regime all the modes are orthogonal to each other and do not interact. In the nonlinear (high amplitude) regime the width modes become intercoupled by the four-wave nonlinear interaction, resulting in an intermodal energy transfer and the mode spectrum enrichment.

As the spin wave input antenna effectively generates only the lowest width mode, the initial waveform launched in the stripe is determined by it solely. Therefore to understand the underlaying physics of quasi-bullet formation it is necessary to consider the nonlinear interaction of higher-order width modes with it.

Our theoretical analysis shows that the interaction of the lowest width mode ($n = 1$) with higher-order modes is different for odd and even higher order modes. While interacting with even modes, the lowest width mode plays the role of the pumping wave. This parametrically transfers its energy to the higher width modes. The interaction is purely parametric and therefore a threshold process. It needs an initial signal to start the process. This signal usually is a thermally excited mode. Therefore the amplified waveform needs a large distance of propagation and a group velocity equal to the velocity of the lowest width mode in order to reach the soliton amplitude level. If there is a damping of the pumped wave, even modes will never reach an amplitude comparable with that of the lowest mode. As a result they can contribute to the nonlinear waveform profile only, if the amplitude of the initial waveform is far beyond the threshold of soliton formation.

Interaction of modes of the same type of symmetry are described by a parametric term as well as by an additional pseudo-linear (tri-linear) excitation term, playing the role of an external source of excitation. Such a pseudo-linear excitation is a threshold-free process. In contrast to parametric processes it does not need an initial amplitude value to start the the process. The pseudo-linear excitation is possible only due to the effective dipolar pinning of the magnetization at the stripe edges. If the spins were unpinned, the interaction of all the width modes would be purely parametric.

The purely parametric mechanism of developing a transversal instability is typical for the process of bullet formation from a plane-wave waveform in an unconfined medium, which distinguishes it from the process of soliton and bullet formation in the waveguide structures.

In contrast, the transverse instability of a wave packet in a confined medium starts as a pseudo-linear excitation of higher-order width modes. This mechanism ensures a rapid growth of the symmetric $n = 3$ mode up to the level where the parametric mechanism starts to work. After that the main mode together with the $n = 3$ mode are capable to rapidly generate a large set of yet higher modes through both pseudo-linear and parametric mechanisms.

Our theory shows that the efficiency of both nonlinear interaction mechanisms (parametric and tri-linear) strongly depends on the group velocity difference of modes and the initial length of the nonlinear pulse. In larger stripes the group velocities of modes are closer to each other. As a result the nonlinearly generated higher-order modes longer remain within the pump pulse. If the pulse is long enough, they reach significant amplitudes and a bullet-like waveform is formed. In narrower stripes the group velocity difference is larger, and consequently the nonlinearly generated high-order waveforms leave faster the pumping area. As a result, for the same pulse length, they do not reach significant amplitudes. The nonlinear steepening results in the transformation of the lowest mode into a soliton.

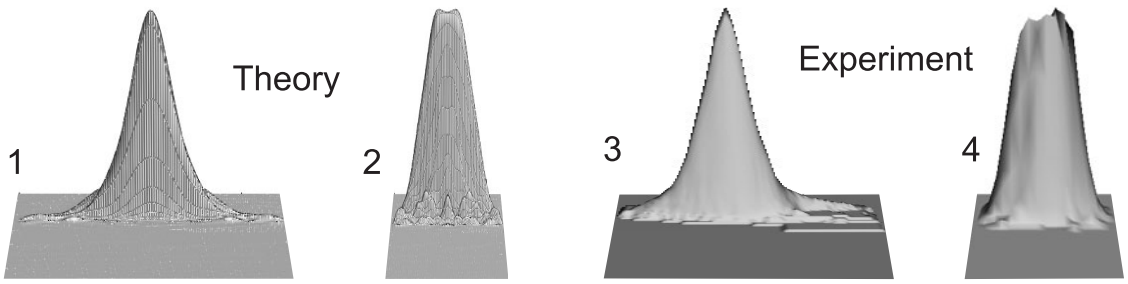

Fig. 2: Lateral shapes of the nonlinear spin wave packets. 1 and 2 – theoretical results calculated for the ferrite stripes of width of 2.5 mm and 1 mm, respectively. 3 and 4 – experimental profiles observed in YIG waveguides of width of 2.5 mm and 1.4 mm, respectively. 1 and 3 – bullets. 2 and 4 – solitons.

The results of our calculations of the lateral shapes of the nonlinear spin wave packets in wide (2.5 mm) and narrow (1 mm) ferrite stripes are shown in Fig. 2. The excellent correspondence with the experimental data provides good evidence for the validity of the developed theory.

Support by the Deutsche Forschungsgemeinschaft is gratefully acknowledged.

References

[1] O. Büttner, M. Bauer, S.O. Demokritov, B. Hillebrands, Yu.S. Kivshar, V. Grimalsky, Yu. Rapoport, A.N. Slavin, Phys. Rev. B **61**, 11576 (2000).
[2] A.A. Serga, B. Hillebrands, S.O. Demokritov, A.N. Slavin, Phys. Rev. Lett. **92**, 117203 (2004).
[3] A.A. Serga, B. Hillebrands, S.O. Demokritov, A.N. Slavin, P. Wierzbicki, V. Vasyuchka, O. Dzyapko, A. Chumak, Phys. Rev. Lett. **94**, 167202 (2005).
[4] A.N. Slavin, O. Büttner, M. Bauer, S.O. Demokritov, B. Hillebrands, M.P. Kostylev, B.A. Kalinikos, V. Grimalsky, Yu. Rapoport, Chaos **13**, 693 (2003).
[5] M. Chen, M.A. Tsankov, J.M. Nash, C.E. Patton, Phys. Rev. B **49**, 12773 (1994).
[6] F.R. Morgenthaler, Proceedings of the IEEE **76**, 138 (1988).
[7] S.O. Demokritov, B. Hillebrands, A.N. Slavin, Phys. Rep. **348**, 441 (2001).
[8] K.Y. Guslienko, S.O. Demokritov, B. Hillebrands, A.N. Slavin, Phys. Rev. B **66**, 132402 (2002).

6.11 Phase-sensitive pulse clipping in non-adiabatic spin-wave amplifier

A.A. Serga, M.P. Kostylev, T. Schneider, and B. Hillebrands[1]

The recently developed non-stationary parametric spin-wave amplifier [1] has already been proven to be a powerful instrument, both to process microwave signals and to investigate linear and nonlinear dynamics of spin wave excitations themselves. For example a high amplification gain of up to 30 dB, phase conjugation and time reversal of travelling spin wave pulses as well as amplification of spin wave solitons and bullets has been demonstrated [2, 3].

The operation of the amplifier underlies the first-order parametric interaction of a spatially localized electromagnetic pump field with a carrier spin wave of half of the pumping frequency. The length l_p of the pump field area determines the main features of the amplifier. Two distinct regimes of interaction are possible.

In the adiabatic case, where the pumping area is much larger than the spin-wave wavelength λ_s, the effective wave number of pumping is close to zero and the energy and momentum conservation laws have the form:

$$k_s + k_i = 2\pi/l_p \simeq 0 \quad , \tag{1-a}$$

$$\omega_s + \omega_i = \omega_p = 2\omega_s \quad . \tag{1-b}$$

Here ω_p is the pumping frequency, and ω_s and k_s are the frequency and the wavevector of the carrier spin wave, respectively. As evident from Eq. (1) an additional spin wave, the so called idle spin wave with frequency $\omega_i = \omega_s$ and wavevector $k_i = -k_s$ generated as a result of interaction between signal and pumping, is propagating in the opposite direction compared to the signal spin wave. Its phase

$$\phi_i = \phi_p - \phi_s + \pi/2 \tag{2}$$

depends both on the phase of the carrier spin wave ϕ_s and on the pump phase ϕ_p, so that an effective energy transfer from the pump electromagnetic field to both spin waves is always realized for any values of ϕ_s and ϕ_p [4]. As a result the amplitude of the output signal does not depend on the phase difference between the signal spin wave and the pumping field.

In the case of a non-adiabatic spin wave amplifier [5] the pump area length l_p is comparable to or even smaller than λ_s which causes a considerable spread of effective pumping wavenumber $0 < k_p < 2\pi/l_p$. As a result, the momentum conservation law Eq. (1-a) cannot be satisfied anymore exactly, and not only the contra-propagating idle wave, but also a strong co-propagating idle wave is created in this process. Now, interference between the co-propagating wave and the amplified signal carrier wave provides the possibility to control the amplitude of the output signal in a wide range by adjustment of the phase difference between ϕ_s and ϕ_p [6]. Thus, the non-adiabatic spin wave amplifier has the property of a phase filter. This useful feature has been already used and permitted us to address specific modes in a closed active spin-wave ring resonator [7], enabling the discovery of novel symmetry-breaking eigen excitations, such as so-called Möbius modes [8].

The parametric amplifier is usually operated in the non-stationary, i.e. in pulsed pump regime in order to use intensities of the pumping beyond the threshold for generation of the carrier spin wave. This allows for a high gain in the wave amplification process [2]. The short pumping time also prevents the generation of exchange dominated spin waves from the thermal level, which have a

[1] In collaboration with A.N. Slavin, Department of Physics,Oakland University, Rochester, Michigan, U.S.A..

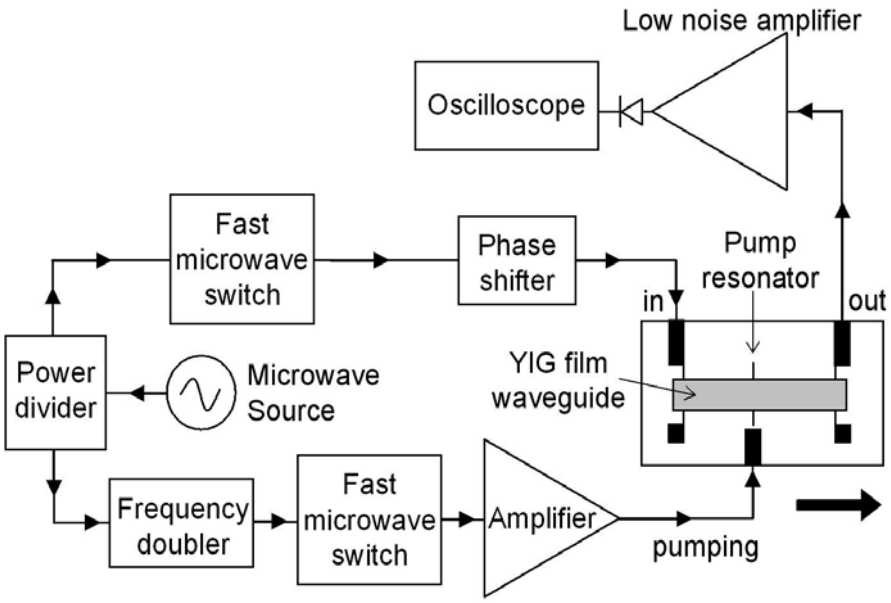

Fig. 1: Schematic diagram of the non-adiabatic spin wave amplifier.

lower threshold compared to the carrier wave. Otherwise these unwanted (parasitic) spin waves are able to disturb the amplification and even the propagation of the carrier spin wave [1, 2].

Here we report our findings, that in the case of non-adiabatic amplification a prolongation of the pump pulse may cause a phase sensitive damping of the tail part of the output signal. The cause for this surprising behavior lies in the phase sensitive gain factor and in a phase detuning effect due to excitation of parasitic spin waves as discussed in detail in the following.

A schematic diagram of the non-adiabatic spin wave amplifier is shown in Fig. 1. Two microstrip antennae of 25 µm width and separated by a distance of 8.5 mm are used for excitation and detection of the carrier spin wave which propagates from the input to the output antenna through a longitudinally magnetized ferrimagnetic spin wave waveguide of 7 µm thickness and of 1.5 mm width. As the material single crystal yttrium-iron garnet (YIG) was chosen due to the low microwave magnetic loss (ferromagnetic resonance linewidth 0.5 Oe, saturation magnetization 1750 G). An external magnetizing field of $H_0 = 1760$ Oe was applied along the waveguide. The pumping magnetic field oriented along the magnetizing field is created by a microstrip inductor of 25 µm width situated halfway between the antennae. In order to increase the intensity of the pumping field this inductor is designed as a half-wavelength resonator with a loaded quality factor of 25 at 13.7 GHz. Since the pumping wave is produced by doubling the frequency of the signal carrier wave it was easy to control the phase shift between these waves using a phase shifter in the signal branch of the microwave circuit (see Fig. 1). The fast microwave switches are used to form the signal and pump pulses.

A 1.3 µs long input pulses were sent to the input antenna with a repetition time of 10 µs. The input power of 10 mW was chosen to guarantee the linear regime of the spin wave propagation. The carrier frequency was 6.85 GHz. At this frequency the wavelength λ_s of the carrier spin wave is near 200 µm. The length l_p of the pumping area is determined by the width of the pump resonator and doesn't exceed 30 µm even taking into account the non-uniformity of the pumping field. Thus the non-adiabatic condition $l_p \ll \lambda_s$ was satisfied very well. The small value of l_p also assures that the amplifier will have a not too high gain and no nonlinear processes, which could potentially de-

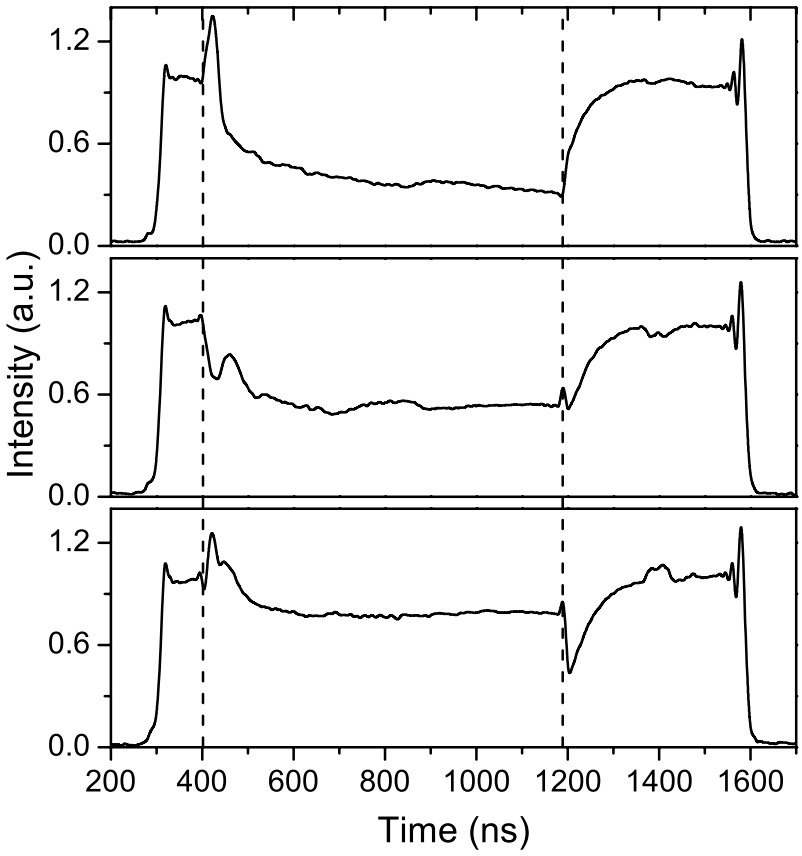

Fig. 2: Waveforms of the output signal for several phase differences between the carrier wave and pumping. The vertical dashed lines indicate the interval of action of the parametric pumping.

velop in the strong amplified spin wave packet, will disturb the experimental results. The pumping power was 8 W. The pumping duration was chosen to be shorter than the input pulse in order to investigate the behavior of the output pulse after the pumping is switched off. The obtained results are shown in Fig. 2. As it is seen a sharp peak is formed in the output signal just after application of the pumping as a result of the initial amplification and the following decay of the carrier spin wave. As the pumping is switched off the intensity of the output signal slowly restores to the initial value. These experiments were performed for an initial phase shift between the signal spin wave and the pumping of $\pi/2$. If the initial phase of the signal wave is changed we observe a reduction of the peak's intensity and even the formation of a dip. Please note that just after the pumping is switched off the intensity of the signal immediately breaks down and then slowly increases to the undisturbed level.

To answer the question about the nature of the described effects we investigated the amplifier by means of time-resolved Brillouin light scattering (BLS) spectroscopy [9]. The YIG sample was probed by coherent light with a wavelength of 532 nm in backward scattering geometry. The laser beam was focused onto the YIG film just above the microstrip pumping inductor. Thus we were able to register light which was inelastically scattered both by the travelling spin waves and by the standing spin wave modes concentrated in a small area around the inductor. A time analysis of separate spectral peaks of the scattered light enables us to observe the dynamics of the corresponding spin wave modes. The obtained results are shown in Fig. 3. The spectral peak near 7 GHz appears at the travelling spin wave frequency and demonstrates the time behavior of the corresponding wave that is very similar to the first waveform in Fig. 2. The peak near 5 GHz is a parasitic spin wave excited from the thermal level due to parametric pumping. It follows from that fact that, as seen from Fig. 3, it appears just after applying the pumping, and it decays from the

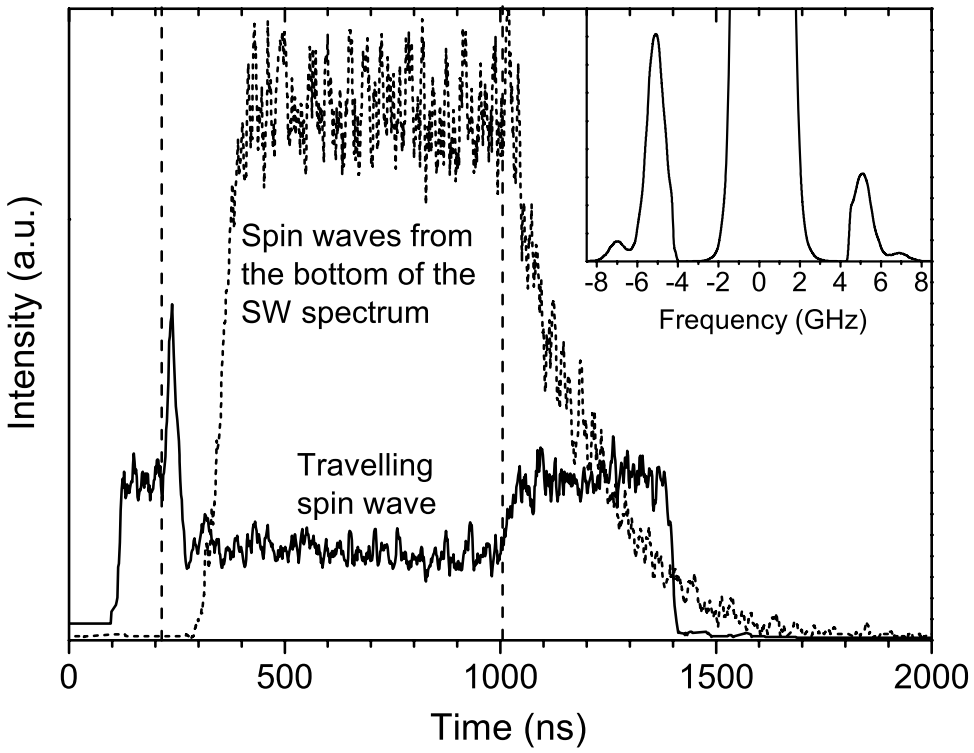

Fig. 3: Waveforms of the propagating spin wave pulse (solid line) and of the non-coherent spin waves near the bottom of the spin wave spectrum (dotted line) obtained by means of the time resolved Brillouin light scattering technique in the area of the pumping resonator. The inset shows the spectrum of the scattered light.

moment when the pumping is switched off. Surprisingly, this peak does not appear at half of the pumping frequency, as it should be in consequence of the energy conservation law Eq. (1-b), but at a significantly lower frequency, which is identified as the position of the bottom of the spin wave spectrum. The most probable mechanism is the so-called kinetic instability. In this mechanism the energy of an overheated group of spin waves with frequencies near half of the pumping frequency transmits to the bottom of the spin wave spectrum due to four-magnons conversion [10]. As this process develops only in the case of the pumping field of $15-20\,\mathrm{dB}$ above the threshold of the first-order parametric generation, it is evident that here we have a high density of the parametrically excited parasitic spin waves.

Let us suppose that the phase shift between the signal spin wave and the pumping was initially adjusted to have constructive interference between the signal wave and the co-propagating idle wave. Irrespective of the specific mechanism of excitation, the appearance of parasitic spin waves of sufficient high amplitude will reduce the static magnetization in the area of the pumping inductor and thus change the local wavenumber of the travelling spin wave:

$$\Delta k_\mathrm{s} = \frac{1}{v_\mathrm{gr}} \frac{2\pi\gamma H_0}{\sqrt{H_0\,(H_0+4\pi M)}} \Delta M \quad , \tag{3}$$

where $\gamma = 2\pi \cdot 2.8\,\mathrm{MHz/Oe}$ and v_gr is the group velocity of the carrier wave. As a result the phase ϕ_s of the signal wave undergoes a constrained shift by

$$\Delta\phi_\mathrm{s} = \int_0^{l_\mathrm{p}} \Delta k_\mathrm{s}\, dl \quad . \tag{4}$$

It is evident from Eq. (2) that a phase shift of the input signal wave by $\pi/2$ will lead to a phase shift between the signal and the idle wave by π. As soon as the phase shift $\Delta\phi_s$ reaches a value of $\pi/2$ the output signal, formed by the two waves which are now out of phase decreases, and the mode depression is observed (see Figs. 2, 3). A further increase of $\Delta\phi_s$ should cause a successive transition from destructive to constructive interference and therefore result in the formation of a train of amplified peaks. However, only one peak was observed unambiguously in our experiment. It is understood by the fact that the intensity of the parasitic spin waves increases and saturates rather fast (see Fig. 3), such that the second peak has not enough time to develop noticeably up to the moment when the static magnetization in the area of parametric interaction is stabilized. The estimations made using the approximate formulae (3, 4) show that to obtain a phase shift ϕ_s that is appreciably larger than $\pi/2$ it is necessary to assume that the total change of local magnetization caused by the parametric excitation of parasitic spin waves (excited near the bottom of the spin wave spectrum) exceeds $\Delta M = 50\,\mathrm{Oe}$. This calculation definitely overestimates the magnitude of ΔM, since the Eq. (3) is literally valid only for sufficiently small values of $\Delta k_s : \Delta k_s \ll k_s$.

In the case the phase of the signal wave is initially tuned to the condition of destructive interference, the growing phase shift $\Delta\phi_s$ causes a following transition to the constructive interference case and the intensity of the signal increases. However, at any case, the maximum intensity of the signal in this area will be lower than the intensity of the first amplified peak. It is the case because this part of the spin wave packet should overpass the disturbed area around the resonator. Here the travelling spin wave is partially reflected due to the non-uniform static magnetization and partially scattered by the fluctuations of the parasitic spin waves. After the pumping is switched off these additional losses are not compensated any more by the amplifier gain and the output signal jumps sharply down as it seen in Fig. 2. Its intensity slowly restores to the undisturbed level as the parasitic spin wave relaxes (see Fig. 2).

In conclusion, we have experimentally demonstrated that the adjustment of the phase difference between the carrier spin wave and the electromagnetic pumping in the non-adiabatic spin wave amplifier enables the control of the amplitude and the shape of the output signal on a wide scale. By means of phase sensitive amplification and clipping of the microwave pulses the amplifier is able to form the output pulses which are significantly shorter compared to both the pumping and the input signal. The phase mismatch of the travelling spin waves caused by the strong excitation of parasitic spin waves at the bottom of spin wave spectrum is found to be the origin of the phase-sensitive clipping.

Support by the Deutsche Forschungsgemeinschaft and by the Oakland University Foundation is gratefully acknowledged.

References

[1] A.V. Bagada, G.A. Melkov, A.A. Serga, A.N. Slavin, Phys. Rev. Lett. **79**, 2137 (1997).
[2] G.A. Melkov, A.A. Serga, A.N. Slavin, V.S. Tiberkevich, A.N. Oleinik, A.V. Bagada, JETP **89**, 1189 (1999).
[3] G.A. Melkov, A.A. Serga, V.S. Tiberkevich, A.N. Oliynyk, A.N. Slavin, Phys. Rev. Lett. **84**, 3438 (2000).
[4] W.H. Louisell, *Coupled Mode and Parametric Electronics* (Wiley, New York, 1960).
[5] G.A. Melkov, A.A. Serga, V.S. Tiberkevich, Yu.V. Kobljanskij, A.N. Slavin, Phys. Rev. E **63**, 066607 (2001).
[6] A.A. Serga, S.O. Demokritov, B. Hillebrands, Seong-Gi Min, J. Appl. Phys. **93**, 8585 (2003).
[7] A.A. Serga, M.P. Kostylev, B.A. Kalinikos, S.O. Demokritov, B. Hillebrands, H. Benner, JETP Lett. **77**, 300 (2003).
[8] S.O. Demokritov, A.A. Serga, V.E. Demidov, B. Hillebrands, M.P. Kostylev, B.A. Kalinikos, Nature **426**, 159 (2003).
[9] O. Büttner, M. Bauer, S.O. Demokritov, B. Hillebrands, Y.S. Kivshar, V. Grimalsky, Yu. Rapoport, A.N. Slavin, Phys. Rev. B **61**, 11576 (2000).
[10] V.S. Lutovinov, G.A. Melkov, A.Yu. Taranenko, V.B. Cherepanov, Sov. Phys.-JETP **95**, 760 (1989).

C. Magnetic Films and Surfaces

6.12 Magnetic patterning of interlayer exchange coupled Fe/Cr/Fe trilayers by Ga^+ ion irradiation

S. Blomeier, V.E. Demidov, P. Candeloro, and B. Hillebrands[1]

There is constant interest in the optimization of magnetic storage devices. One key parameter of such devices is the areal density of the bits which store the information in the form of magnetic single domain states. An increase of the areal density of a magnetic storage medium is usually achieved by a reduction of the bit size, which is limited by the superparamagnetic effect due to thermal fluctuations of the magnetic moments [1]. In conventional magnetic storage media a bit usually comprises at least about one hundred magnetically isolated nanoparticles for signal-to-noise reasons. Each of these nanoparticles must fulfill the severe condition of thermal stability.

In order to circumvent the problem of thermal stability one can generate "pre-written" magnetic bits that behave as single magnetic entities. Due to its increased magnetic volume the stability of the magnetic state of a pre-written bit against thermal fluctuations is drastically increased. However, standard lithographic patterning techniques removing material between the bits lead to variations in the height of the storage medium, typically of the order of $10-100\,\mathrm{nm}$. Such a topographic patterning is the source of two significant problems in magnetic recording technology. First, a variation in height leads to tribology problems in the near-contact recording scheme already used for conventional hard discs. Second, such height variations cause large variations in optical reflectivity, which are undesirable in the emerging near-field magneto-optical technologies. For these reasons it is a subject of contemporary research to develop methods which allow for magnetic patterning and, at the same time, avoid topographic patterning as much as possible.

Recently it was demonstrated that the interlayer exchange coupling between two ferromagnetic Fe layers separated by a thin Cr spacer layer can be modified by means of low-fluence ion irradiation [2, 3]. A model was established that ascribes the ion-induced modification of the interlayer exchange coupling to interfacial intermixing within the trilayer. This intermixing process results in a change of the effective interlayer thickness and in the creation of ferromagnetic pinholes within the interlayer [2]. Due to direct exchange through these pinholes, the antiferromagnetic coupling is weakened for low ion fluences and can be transformed into ferromagnetic coupling for sufficiently high ion fluences.

It was also shown that magnetic patterning due to local irradiation is possible with a lateral resolution better than 200 nm [3]. When compared to other magnetic patterning techniques (see, e.g. [4,5]) ion-induced patterning of exchange-coupled Fe/Cr/Fe trilayers has the significant advantage that it enables the fabrication of small ferromagnetic elements embedded into an environment with a zero net magnetic moment in remanence and a very low magnetic susceptibility, which is of interest for technical applications.

Within the scope of the work presented here, the patterning process was investigated in more detail. Epitaxial Fe 10 nm/Cr 0.7 nm/Fe 10 nm (001) trilayer systems were grown by electron beam evap-

[1] In collaboration with S.O. Demokritov, Institut für Angewandte Physik, Westfälische Wilhelms-Universität, Münster, Germany; B. Reuscher, A. Brodyanski, and M. Kopnarski, Institut für Oberflächen- und Schichtanalytik, Technische Universität Kaiserslautern, Kaiserslautern, Germany.

oration, using a molecular beam epitaxy system at a base pressure of $1 \cdot 10^{-10}$ mbar. A MgO(100) substrate, covered by a thin Fe seed layer of 1 nm thickness and a Ag buffer layer of 150 nm thickness was used as a growth template. The whole stack was covered by a 2 nm thick Cr cap layer to prevent the sample from oxidation. With the exception of the Fe seed layer and the Cr cap layer, which were grown at room temperature, the system was deposited at a temperature of 120 °C to improve the smoothness of the interfaces. In order to avoid interfacial intermixing due to diffusion, the first 2 nm of both the Ag buffer layer and the lower Fe layer were grown at room temperature. *In-situ* low energy electron diffraction studies of the Ag buffer layer and the upper Fe layer confirmed the high epitaxial quality of the deposited system.

One of the prepared systems was magnetically patterned by irradiation with 30 keV Ga^+ ions, using an FEI ALTURA 865 Dual Beam Focused Ion Beam (FIB) source. Several series of squares of $20 \times 20\,\mu m^2$ size were written onto the sample, using an ion beam with a diameter of 25 nm and a beam current of 300 pA. The edges of the squares were aligned parallel to the easy axes of the fourfold magnetic anisotropy of the Fe layers. Each square in a series was irradiated with a different ion fluence, ranging from $1.25 \cdot 10^{16}$ ions/cm^2 to $6.25 \cdot 10^{16}$ ions/cm^2. These values were chosen in consideration of preliminary experiments, which indicated that only within this fluence regime a complete transition from an antiferromagnetic to a ferromagnetic state of the irradiated areas can be achieved.

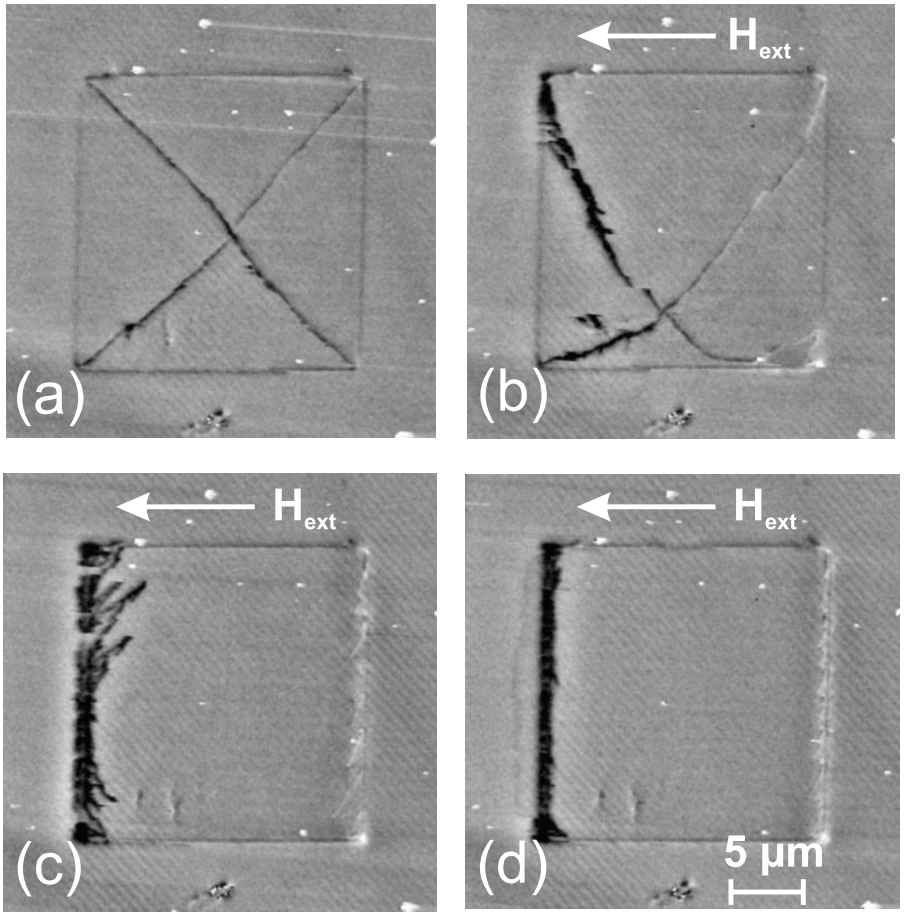

Fig. 1: Magnetic images of a square recorded by MFM, showing an area of $30 \times 30\,\mu m^2$. The square was irradiated with an ion fluence of $2.7 \cdot 10^{16}$ ions/cm^2. The white arrows indicate the direction of the externally applied field. The images correspond to field values of 0 Oe (a), 14 Oe (b), 27 Oe (c), and 41 Oe (d).

Patterning of the magnetic properties of the irradiated sample was investigated by magnetic force microscopy (MFM). The domain structure observed in the irradiated areas clearly indicates that the two Fe layers are coupled ferromagnetically in these areas, and the entire stack demonstrates strong ferromagnetic properties. Figure 1 displays several MFM images which were recorded from a square that was irradiated with a fluence of $2.7 \cdot 10^{16}\,\mathrm{ions/cm^2}$. A typical flux closure state can be observed in remanence (Fig. 1a). As an external field is applied, one of the domains grows at the expense of the others (Fig. 1b). At an external field of 27 Oe, the flux closure state vanishes, but some complicated domain walls are still remaining (Fig. 1c). This value is in agreement with the result of a simple estimation, which shows that a field of about 20 Oe is necessary to remove the flux closure domain structure of a $20 \times 20\,\mu\mathrm{m}^2$ Fe-square with a thickness of 20 nm. Finally, at an external field value of 41 Oe, the patterned element is in a saturated single-domain state (Fig. 1d). A similar behavior was observed for squares irradiated with different ion fluences, except for those which were irradiated with the highest ion fluence of $6.25 \cdot 10^{16}\,\mathrm{ions/cm^2}$. In this case, no ferromagnetic properties could be observed, which is probably caused by an oxidation of the Fe layers.

In order to gain information about the topography of the irradiated samples, atomic force microcopy (AFM) measurements were performed. Figure 2 shows the results of these measurements, displaying $4 \times 4\,\mu\mathrm{m}^2$ sections at the boundary of the squares. The left half in each image shows an irradiated area while the right half shows a non-irradiated area. Corresponding height profiles are given below each image. It is interesting to note that the dependence of the height of the irradiated area on the fluence is non-monotonic. In fact, as can be seen in Fig. 2, at low fluences the average height of the irradiated areas is increased in comparison with the height of the non-radiated area. On the other hand, the height of the irradiated areas is reduced for high ion fluences. For the intermediate fluence value of $2.7 \cdot 10^{16}\,\mathrm{ions/cm^2}$ the heights of the irradiated and non-irradiated areas remain roughly at the same level.

The observed non-monotonic dependence of the height on the fluence apparently originates from a competition of two different mechanisms. On the one hand, the irradiation of a material with keV

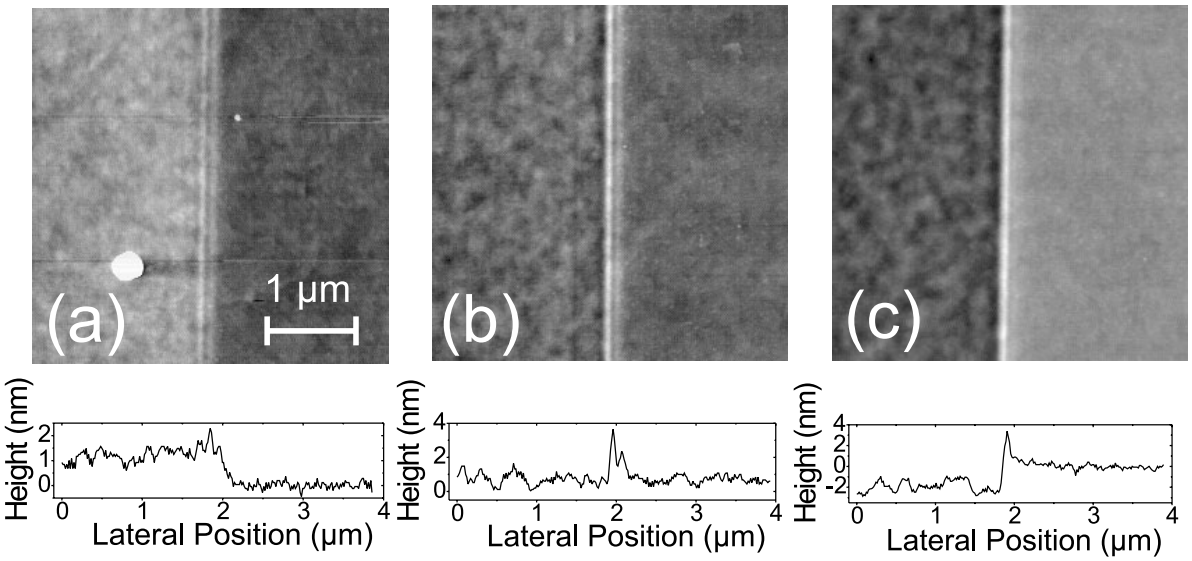

Fig. 2: Topographic images recorded by AFM showing a $4 \times 4\,\mu\mathrm{m}^2$ section at the boundary of squares irradiated with a fluence of (a) $1.25 \cdot 10^{16}\,\mathrm{ions/cm^2}$, (b) $2.7 \cdot 10^{16}\,\mathrm{ions/cm^2}$, and (c) $4.9 \cdot 10^{16}\,\mathrm{ions/cm^2}$. The left half in each image shows an irradiated area while the right half shows a non-irradiated area. Corresponding height profiles are given below each image.

ions is accompanied by sputtering, which causes a reduction in height of the irradiated areas. On the other hand, prior to irradiation the multilayer stack has a well-ordered epitaxial lattice, which has a high packing density. Upon irradiation, introduction of lattice defects as well as implantation of Ga^+ ions into the multilayer takes place and, correspondingly, structural rearrangement processes occur. As a result, the volume of the irradiated regions increases, which leads to an increase of the height of the stack, since the irradiated regions are laterally confined by the non-irradiated areas. Since the sputtering yield depends on the ion energy and the binding energy between atoms in the lattice, it increases with increasing fluence and decreasing quality of the lattice. At the same time, with decreasing quality of the lattice, the influence of the lattice defects on the density of the lattice should be flattened off. Thus, at smaller fluences the expansion due to the lattice defects prevails, while at higher fluences the sputtering process dominates. At a fluence of about $2.7 \cdot 10^{16}\,\mathrm{ions/cm^2}$ the effects of sputtering and expansion compensate each other, and the resulting height difference between the irradiated and non-irradiated areas vanishes.

Furthermore, in each of the profiles shown in Fig. 2 a peak at the boundary between the irradiated and non-irradiated areas is visible. This peak is most pronounced (in terms of absolute values) for the higher ion fluences. Its height ranges from $1.2 \pm 0.3\,\mathrm{nm}$ for the lowest fluence up to $3.5 \pm 0.5\,\mathrm{nm}$ for the highest fluence applied. Redeposition of sputtered material probably plays a role in the formation of this peak, and stray edge effects may also contribute to its existence. Such effects might originate from the exposure of the edge of the patterned elements to the tail of the ion beam, which is assumed to have a Gaussian profile with exponential tails. Additional experiments have shown that this effect can be minimized by a proper choice of the ion beam spot size.

In summary, magnetic and topographic properties of epitaxial, antiferromagnetically coupled Fe/Cr/Fe(001) trilayers magnetically patterned by 30 keV Ga^+ ion beams have been studied. It was shown that areas with strong ferromagnetic properties can be created at relatively low fluences of the order of $10^{16}\,\mathrm{ions/cm^2}$, and it was also demonstrated that a fluence range exists which allows for magnetic patterning of this system without any significant variation in the height of the bombarded surfaces. The results presented here strongly indicate that the irradiation of antiferromagnetically coupled trilayers with keV ions is a convenient tool to create magnetically patterned material systems with unique properties which are of technological interest. More details of this work can be found in [6].

This work was supported in part by the DFG and the EU-RTN NEXBIAS (HRPN-CT-2002-00296).

References

[1] R.L. White, J. Magn. Magn. Mater. **209**, 1 (2000).
[2] S.O. Demokritov, C. Bayer, S. Poppe, M. Rickart, J. Fassbender, B. Hillebrands, D.I. Kholin, N.M. Kreines, M.O. Liedke, Phys. Rev. Lett. **90**, 097201 (2003).
[3] V.E. Demidov, D.I. Kholin, S.O. Demokritov, B. Hillebrands, F. Wegelin, J. Marien, Appl. Phys. Lett. **84**, 2853 (2004).
[4] C. Chappert, H. Bernas, J. Ferré, V. Kottler, J.-P. Jamet, Y. Chen, E. Cambril, T. Devolder, F. Rousseaux, V. Mathet, H. Launois, Science **280**, 1919 (1998).
[5] A. Mougin, S. Poppe, J. Fassbender, B. Hillebrands, G. Faini, U. Ebels, M. Jung, D. Engel, A. Ehresmann, H. Schmoranzer, J. Appl. Phys. **89**, 6606 (2001).
[6] S. Blomeier, B. Hillebrands, V.E. Demidov, S.O. Demokritov, B. Reuscher, A. Brodyanski, M. Kopnarski, J. Appl. Phys. **98**, 1 (2005).

6.13 Determination of the exchange constant in the $Co_2Cr_{0.6}Fe_{0.4}Al$ Heusler alloy

D. Hoffmann and B. Hillebrands[1]

The development of new, highly efficient spintronic devices is an urgent issue in contemporary magnetic information storage and processing technology. One of the primary tasks is the development and integration of new materials with unique, specifically tailored magnetic properties. Of paramount importance are materials with high spin polarization, as they enable large magnetoresistance effects. It has been shown that the so-called Heusler alloys are a promising candidate for such applications. Because of their behavior like half-metallic ferromagnets [1] (HMF) Heusler alloys have been predicted to exhibit 100 % spin polarisation at the Fermi level. It must be pointed out that any symmetry breaking effects at surfaces or lattice mismatch between epitaxially grown films and substrate can lead to a significant decrease of the spin polarisation. The origin is subject to current investigations. In this context, it is an important issue to investigate the properties of thin Heusler alloy films, in particular the effects which lead to a decrease of the spin polarisation. For these reasons, we investigated the full Heusler alloy $Co_2Cr_{0.6}Fe_{0.4}Al$ in collaboration with the Johannes Gutenberg-Universität Mainz. Here we report our results on the determination of the exchange constant A in $Co_2Cr_{0.6}Fe_{0.4}Al$ by means of Brillouin light scattering spectroscopy (BLS).

All samples were prepared in Mainz by DC-magnetron sputtering from a stoichiometric $Co_2Cr_{0.6}Fe_{0.4}Al$ target. The first sample is a $L = 110\,\mathrm{nm}$ thick film. The saturation magnetization at room temperature was determined as $4\pi M_s = 6500\,\mathrm{G}$ by vibrating sample magnetometry (VSM).

Figure 1 shows a typical BLS spectrum for a transferred wave vector of $q = 1.67 \cdot 10^5\,\mathrm{cm}^{-1}$ in an applied field of $H_{\mathrm{appl}} = 334\,\mathrm{Oe}$. As it is seen, several peaks corresponding to spin-wave modes can

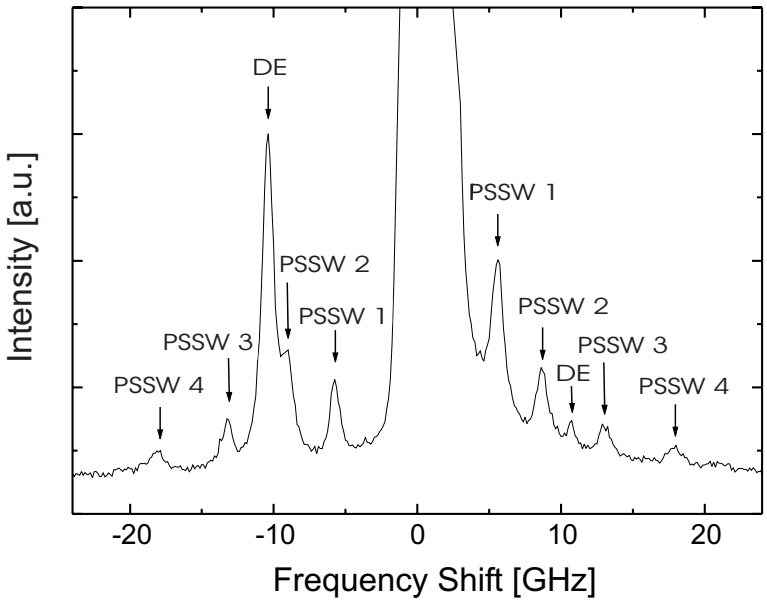

Fig. 1: Typical spectrum of a $L = 110\,\mathrm{nm}$ thick $Co_2Cr_{0.6}Fe_{0.4}Al$ Heusler alloy for a transferred wave vector of $q = 1.67 \cdot 10^5\,\mathrm{cm}^{-1}$ in an applied field of $H_{\mathrm{appl}} = 334\,\mathrm{Oe}$.

[1] in collaboration with G. Jakob and H. Adrian, Fachbereich Physik, Johannes Gutenberg-Universität Mainz.

be observed both in the Stokes and anti-Stokes regime. The magnetic origin of these peaks was confirmed by the observation that their frequencies change upon changing the applied field. Thus these peaks correspond to the Damon-Eshbach (DE) mode and so-called perpendicular standing spin waves (PSSW). The DE mode have the prominent feature that it is observed with different intensities in the Stokes and anti-Stokes regime. This can be understood by its exponential decay across the film thickness and its non-reciprocity.

By varying the transferred wave vector the dispersion relation can be obtained experimentally. It is shown in Fig. 2, the squares indicate PSSW modes. As it is seen the frequencies of the PSSW modes do not significantly depend on the transferred wave vector. This behaviour is well known and, outside the crossing regimes with the diploar modes, the frequencies of the PSSW modes can be approximately described by [2]

$$\nu_n(k_n) = \frac{|\gamma|}{2\pi}\left[\left(H + \frac{2A}{M_s}k_n^2\right)\left(H + 4\pi M_s + \frac{2A}{M_s}k_n^2\right)\right]^{\frac{1}{2}} \quad . \tag{1}$$

Here, k_n is the wave vector of the mode with number $n = 1, 2, 3, ...$ which is quantized across the film thickness. As the saturation magnetization M_s is known, the only remaining parameters are the exchange constant A and the Rado-Weertman Boundary conditions. These conditions determine whether the magnetization is pinned or unpinned at the two surfaces. It turns out that only unpinned boundary conditions are able to model the observed spectrum and so the quantized wave vectors are given by $k_n = n \cdot L/\pi$. The exchange constant was fitted as $A/2\pi {M_s}^2 = 4.3 \cdot 10^{-13}\,\mathrm{cm}^2$, i.e. $A = 7.2 \cdot 10^{-7}\,\mathrm{Oe}^2 \cdot \mathrm{cm}^2$. The resulting dispersions obtained with the equations from Kalinikos and Slavin [2] are shown in Fig. 2 as solid lines.

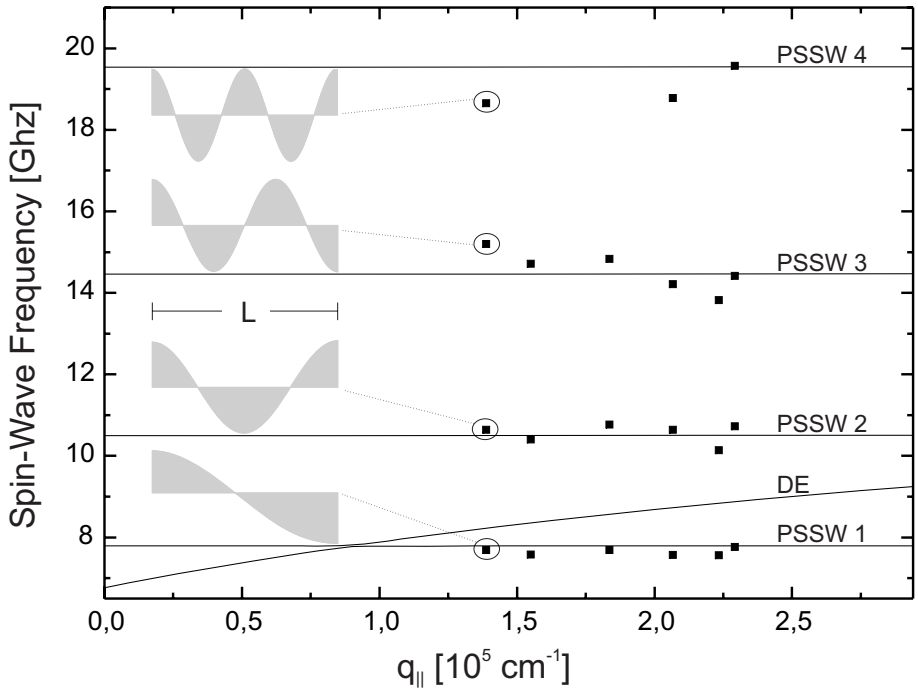

Fig. 2: Dispersion relation of a $L = 110\,\mathrm{nm}$ thick $Co_2Cr_{0.6}Fe_{0.4}Al$ Heusler alloy in an applied field of $H_{\mathrm{appl}} = 800\,\mathrm{Oe}$. The squares show the measured dispersion, the solid line the fit as described in the text. The insets show the corresponding mode profiles as a function of depth into the film.

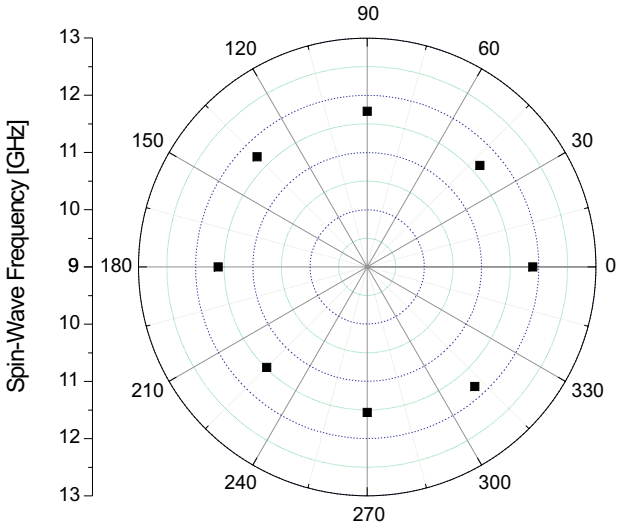

Fig. 3: Spin-wave frequencies of a $L = 41\,\mathrm{nm}$ thick $Co_2Cr_{0.6}Fe_{0.4}Al$ film as a function of the in-plane angle.

The second sample is a $L = 41\,\mathrm{nm}$ thick $Co_2Cr_{0.6}Fe_{0.4}Al$ film, which was grown at 573 K and post-annealed for 1 h at a temperature of 723 K. Figure 3 shows the frequency of the DE mode as a function of the in-plane angle. As it is seen no in-plane anisotropy can be found. This isotropy confirms that the sputtering process did not lead to an epitaxial growth. The $Co_2Cr_{0.6}Fe_{0.4}Al$ film predominantly crystalizes in a disordered $B2$ structure.

In conclusion we have determined the exchange constant of the thin film Heusler alloy $Co_2Cr_{0.6}Fe_{0.4}Al$ and confirmed that the sputtering process leads to a sample growth which does not produce anisotropies.

This work is supported by the Deutsche Forschungsgemeinschaft through the Forschergruppe 559 “Neue Materialien mit hoher Spinpolarisation”.

References

[1] R.A. de Groot, F.M. Mueller, P.G. van Engen, and K.H.J. Buschow, Phys. Rev. Lett. **50**, 2024 (1983).
[2] B.A. Kalinikos, A.N. Slavin, J. Phys. C **19**, 7013 (1986).

6.14 Domain structure during magnetization reversal of PtMn/Co exchange bias micro-patterned lines

M.O. Liedke and B. Hillebrands[1]

The results presented here have been partially obtained during and following a secondment of Maciej Oskar Liedke to the group of Prof. P.P. Freitas at INESC MN in Lisbon. A significant part of the measurements has been made at the FZ Rossendorf in Dresden.

In order to investigate the relation between shape anisotropy and unidirectional anisotropy in exchange biased microstructures, the magnetic domain configuration during magnetization reversal was studied as a function of the ratio between both anisotropy contributions. Due to a competition between the unidirectional anisotropy and the in-plane contribution of the shape anisotropy the domain structure is strongly affected. When the latter is smaller than all other anisotropy contributions the magnetic system brakes up into domains and eventually 360° domain walls show up. Generally 360° domain walls are observed in very thin films (less than 30 nm), where Néel walls occur and in which the Bloch line energy is significantly high [1]. In particular such a domain wall formation can be found close to inclusions or defects at the edges of a patterned structure due to interactions between the walls and the defects. Due to defects Bloch lines can be created within the Néel walls. The Bloch lines remain pinned, even if the walls generate a nonequlibrium configuration as a consequence. A 360° wall is formed, if a 180° wall sweeps through the film, passes a pinhole, and a Bloch line gets trapped. As a result inhomogeneities give rise to domain wall pinning and the formation of 360° walls [2]. The 360° domain wall structures were found to be stable up to high magnetic field values, and they can act as nucleation sites for the magnetization process [3].

We report on magnetic force microscopy (MFM) investigations of the PtMn/CoFe exchange bias system which is relevant for magnetic sensor applications. The formation of local domain structures or 360° domain walls can cause noise in read heads for disk drives and has to be avoided. The occurrence of 360° domain walls during magnetization reversal in spin-valve structures has been reported by Gillies et al. [4]. However, Pokhil et al. [5], who investigated topographically patterned PtMn/CoFe exchange bias bilayers, did neither observe a monodomain state nor 360° domain walls. This has been attributed to the relatively large in-plane exchange length which leads to large switching areas. These observations are consistent with our results of the as-prepared system prior to ion irradiation.

The samples were prepared in Lisbon by means of sputter deposition on glass substrates. After deposition the samples were annealed above the Néel temperature, T_N, and cooled down in the presence of a 2 kOe magnetic field. Due to the annealing procedure an unidirectional anisotropy was introduced in the system and a chemically ordered $L1_0$ phase was obtained in the antiferromagnetic PtMn layer. The bottom pinned microstructures were fabricated from a stack consisting of Ta 7 nm/PtMn 20 nm/CoFe 4 nm/Ta 4 nm. By means of optical lithography and physical etching several patterns with decreasing lateral sizes of either the elements or the spacing between the elements were prepared. The largest square was $50 \times 50\,\mu m^2$ and the smallest only $1\,\mu m^2$. The separating lines ranged from 2 µm to 10 µm in width. The spacing between the lines was chosen

[1] In collaboration with J. Fassbender, K. Potzger and A. H. Bothmer, Institut für Ionenstrahlphysik und Materialforschung, Forschungszentrum Rossendorf, Dresden, Germany; M. Rickart and P.P. Freitas, INESC MN, Lisbon, Portugal.

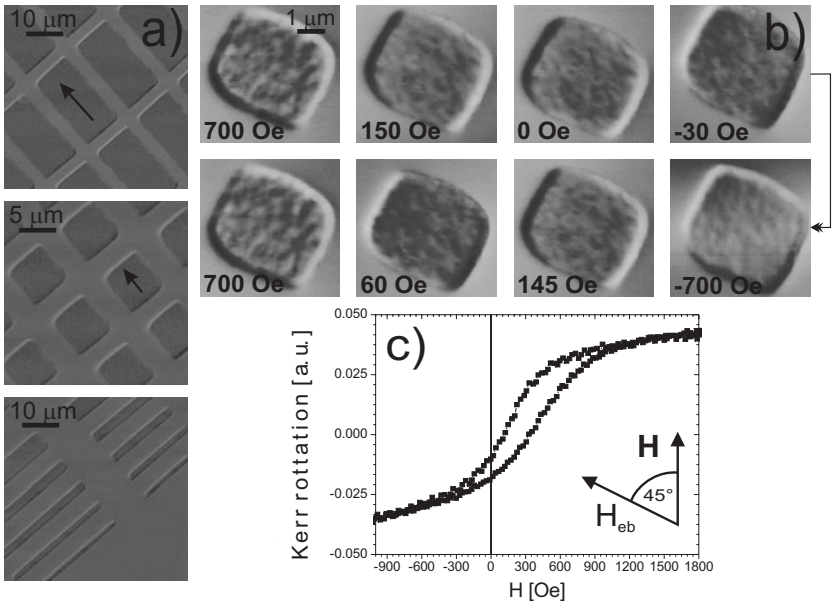

Fig. 1: a) Comparison of the MFM scans of the structures made by direct-write laser lithography. Black arrows indicate the magnetization direction. b) Several MFM images as a function of applied field. c) Typical hysteresis loop from an unpatterned film.

large enough to avoid magnetostatic interactions. The orientation of the stripes was either parallel or perpendicular to the unidirectional anisotropy. In order to modify the ratio between both anisotropy contributions the exchange bias field strength was reduced by means of 5 keV He^+ ion irradiation. After irradiation with a fluence of $7 \cdot 10^{15}$ ions $\cdot$ cm^{-2} the initial exchange bias field (~ 400 Oe) was reduced to about 200 Oe. The magnetization reversal processes were studied by means of magneto-optical Kerr effect (MOKE) magnetometry and magnetic force microscopy in an applied magnetic field. The domain structure was observed in tapping mode with a Co-Cr coated silicon pyramidal tip, magnetized initially in a perpendicular magnetic field. The lift height of the tip was around 80 nm above the surface during scanning.

The experiment consists of two parts. First, MOKE and MFM studies were performed on as-prepared samples and second, the system was irradiated with 5 keV He^+ ions and then reinvestigated. In general one can find a strong competition between different kinds of anisotropy contributions in patterned exchange biased media. Especially shape and unidirectional anisotropy play a crucial role [6]. Therefore, an initial investigation has been performed on a variety of different pattern shapes as presented in Fig. 1a. Since the coupling between PtMn and CoFe exhibits a strong exchange bias field (saturation field larger than 1 kOe), the as-prepared sample was measured in an magnetic field applied in-plane at an angle of 45° with respect to the exchange bias direction. The main purpose for that was to decrease the influence of the magnetic field on the scanning system of the MFM.

Several MFM images were taken from the structures in the remanent state (Fig. 1a). All images show a mono-domain state for all structures in zero magnetic field with the magnetization aligned with the exchange bias field direction. The shape of the structure does not influence the magnetization direction. For both configurations, the long axis of the stripes along and perpendicular to H_{eb}, a single domain behavior with a black and white magnetic contrast at the opposite edges is observed. Pokhil et al. [5] investigated a similar system (PtMn 10 nm/CoFe 10 nm, $2 \times 5\,\mu m^2$ rectangles; long axis along H_{eb}) by MFM. In contrast to our investigations no single-domain state

is observed in zero applied field. Figure 1 (a and b) shows MFM images of rectangles with similar dimensions to those investigated by Pokhil et al. In our case the magnetization reversal curve of the unpatterned film exhibits a remanence close to the saturation magnetization (Fig. 1c) in the geometry investigated. This is consistent with a mono-domain state. As a next step the sample was measured in an applied magnetic field. Several scans were taken by MFM at different applied magnetic fields (Fig. 1b). The magnetization reverses in a rotational process and therefore only monodomain states are observed. In some cases a small ripple contrast inside the patterns is observed. The switching takes place at about -20 Oe for the descending branch and at about 100 Oe for the ascending branch of the magnetic reversal loop, consistent with the magnetization reversal loop of the unpatterned film (Fig. 1c).

After ion irradiation a drastic change in the overall magnetization reversal behavior is observed. After a magnetic field sweep the initial monodomain magnetization state brakes up into small domains with 360° domain walls in between (see Fig. 2). The overall magnetization direction is pointing along the exchange bias direction (Fig. 2 - 900 Oe). Upon reduction of the applied magnetic field the number of 360° domain walls increases. The switching process proceeds via a domain wall motion process. In zero applied field the magnetization of the sample has already switched opposite to the initial magnetization direction. A contrast reversal at the edges of the structures is clearly observed. With the change of the sign of the magnetic field the number of domain walls decreases but they do not vanish completely up to large negative fields. They are more stable for the patterns with a smaller width since the domain walls can be pinned at the edges more effectively. For broader structures the distance between neighboring edges is too large and thus a circular shape of the walls occurs more often. Following the ascending branch no 360° domain walls are observed after saturation in a large negative field.

In Fig. 3 the growth processes, the movement and the mechanism of annihilation are illustrated. The magnetization vector in the center of the 360° domain wall (Fig. 3a) points H into the direction of the reversed domain, antiparallel to the applied magnetic field. When an opposite field is applied the 360° domain wall can break up into two 180° domain walls which move apart from each other (Fig. 3a). A new 360° wall is created if two 180° domain walls with the same chirality coincide at the same position after propagation. If the sense of rotation is opposite the two domain walls will vanish (Fig. 3b). Our interpretation is consistent with that proposed by Schäfer and Hubert [3]. In our investigations only 360° domain walls with the same chirality are found. This is due to the fact that domain walls with different chirality have canceled each other already in order to minimize

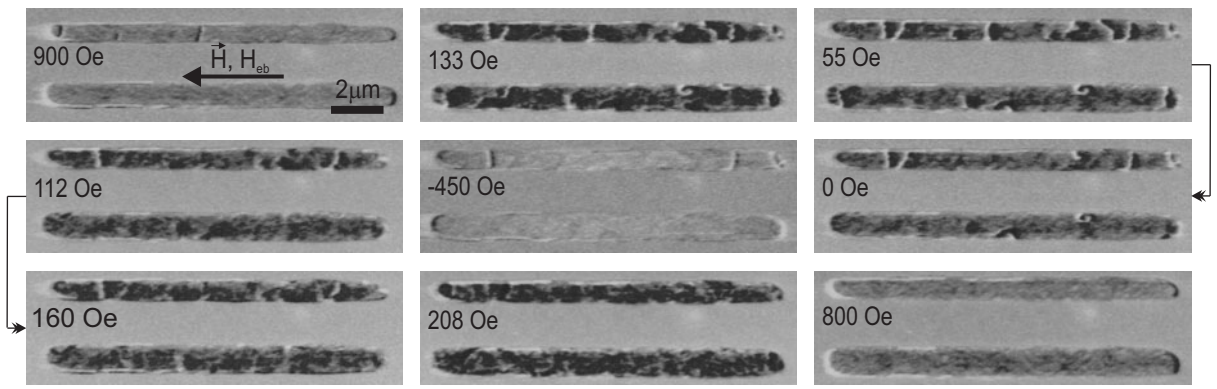

Fig. 2: Several MFM images for different applied magnetic fields for the 1.5 and 2 µm patterned lines. 360° domain walls are clearly visible.

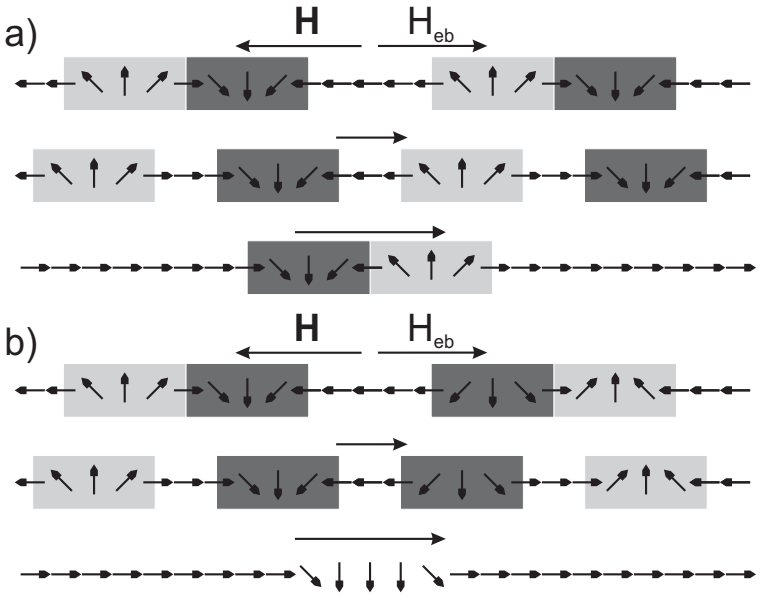

Fig. 3: Sketch of the evolution of a 360° domain wall: a) trapping process, b) annihilation.

the total energy of the system. Additionally the unidirectional pinning direction can play a role giving the contribution to the trapping process.

In summary, we investigated magnetic domain structures in exchange bias systems which were exposed to 5 keV He^+ ions. As a result the exchange coupling at the interface between the ferromagnetic and the antiferromagnetic layer was weakened. Only partially the magnetization reversal process was accomplished by rotation of the magnetization direction inside the domains in between 360° domain walls. Nearly coherent rotation was found in the case of the as-prepared sample, before irradiation. Additionally we found that the stability of 360° wall formations can be connected to the pinning direction of the antiferromagnetic layer.

This work was partially supported by the Deutsche Forschungsgemeinschaft. M. O. L. acknowledges the financial support from the EU-RTN NEXBIAS (HPRN-CT2002-00296).

References

[1] L.J. Heyderman, H. Niedoba, H.O. Gupta, I.B. Puchalska, J. Magn. Magn. Mater. **96**, 125 (1991).
[2] T. Schrefl, J. Fidler, M. Zehetmayer, J. Appl. Phys. **97**, 5517 (2000).
[3] R. Schäfer and A. Hubert, IEEE Trans. Magn. **29**, 2738 (1993).
[4] M.F. Gillies, J.N. Chapman, J.C.S. Kools, J. Appl. Phys. **78**, 5554 (1995).
[5] T. Pokhil, D. Song, E. Linville, J. Appl. Phys. **91**, 6887 (2002).
[6] S.H. Chung, A. Hoffmann, M. Grimsditch, Phys. Rev. B **71**, 214430-1 (2005).

6.15 Ion irradiation patterning of NiFe/FeMn exchange bias system

P. Candeloro, M.O. Liedke, S. Blomeier, P.A. Beck, H. Schultheiß, and B. Hillebrands[1]

The exchange bias effect, i.e. a shift of the hysteresis loop along the field axis, has been known for several decades [1], but recently it is attracting renewed interest due to its applications as pinning layer in magnetoresistive devices (giant magnetoresistance and magnetic tunnel junctions). When a ferromagnetic(F)/antiferromagnetic(AF) bilayer is deposited in an applied external field, or when it is cooled down through the Néel temperature in a field, the magnetization direction of the F layer affects the AF spin arrangement. The exchange interaction at the interface produces an internal field which shifts the hysteresis loop of the so-called exchange bias field, H_{eb}. In the past years several works [2, 3] have demonstrated that ion irradiation can induce an enhancement or a suppression of the exchange bias field, the final effect depending on mass, energy and fluence of the ions used. For example, in the case of $Ni_{81}Fe_{19}/Fe_{50}Mn_{50}$ exchange bilayers, 10 keV He ions irradiation produces an enhancement of H_{eb} when ion doses are smaller than $7.5 \cdot 10^{14}\,\mathrm{ions/cm^2}$, while suppression is observed for larger doses [3]; instead similar experiments with 30 keV Ga ions and fluences down to $0.5 \cdot 10^{14}\,\mathrm{ions/cm^2}$ have shown only a suppression of H_{eb} [4].

Recently ion irradiation has been proposed as a patterning tool for different magnetic systems [2, 5–7]. The increasing interest for this technique is due to the capability of tailoring the magnetic properties without affecting the sample topography. This allows one to preserve the medium planarity, which is an important parameter in industrial applications, for instance in hard-disk technology where the head-to-media spacing is at nanometer scale. On the other hand, the magnetization reversal process, which is as relevant as the sample topography, requires further investigations. In fact, in ion irradiated patterns, both irradiated and non-irradiated areas constitute the same continuous film and direct magnetic coupling is expected to occur at the boundary regions; at which extent this coupling affects hysteresis loops and domains structure evolution is still a poorly investigated topic. In this work we report on ion patterning of $Ni_{81}Fe_{19}/Fe_{50}Mn_{50}$ exchange bias bilayers, focusing our attention on Magneto-Optical Kerr Effect (MOKE) and Magnetic Force Microscopy (MFM) characterization.

A polycrystalline $Ni_{81}Fe_{19}/Fe_{50}Mn_{50}$ continuous film was grown in a UHV system, exploiting both e-gun and effusion-cell deposition. The sample stack, deposited on a silicon substrate, is Si/Cu 15 nm/$Ni_{81}Fe_{19}$ 5 nm/$Fe_{50}Mn_{50}$ 10 nm/Cr 2 nm, where Cu 15 nm is a buffer layer and

pattern	shape	width (µm)	spacing (µm)
a	squares	1.4	0.1
b	squares	1.5	1.5
c	stripes	1.4	0.1
d	stripes	1.5	0.5

Table 1: Geometrical parameters of each pattern, that is shape of the magnetic elements (squares or infinite stripes), lateral width of the elements and spacing. In all the patterns the spacing is the irradiated area, i.e. where the exchange bias is suppressed.

[1] In collaboration with J. Fassbender, Institut für Ionenstrahlphysik und Materialforschung, Forschungszentrum Rossendorf, Dresden, and B. Reuscher, Institut für Oberflächen und Schichtanalytik (IFOS), Kaiserslautern.

Cr 2 nm is a capping layer to prevent oxidation; the exchange bias field is then initialized through a field-cooling procedure. Subsequently a 30 keV Ga^+ Focus Ion Beam (FIB) facility at IFOS-Kaiserslautern was used to produce four different magnetic patterns (see Tab. 1): a) $1.4 \times 1.4\,\mu m^2$ squares with 0.1 µm spacing; b) $1.5 \times 1.5\,\mu m^2$ squares with 1.5 µm spacing; c) 1.4 µm wide stripes with 0.1 µm spacing; d) 1.5 µm wide stripes with 0.5 µm spacing. In all the patterns the irradiated area is the spacing between the elements and the ion dose was $(5-6) \cdot 10^{14}\,ions/cm^2$, which is known from previous studies [3] to ensure the suppression of H_{eb}. The patterns are exposed with squares sides and stripes parallel to the direction of the initializing field.

Figure 1 shows hysteresis loops measured by MOKE on both the continuous film and the patterned areas, the external field is applied parallel to the direction of the exchange bias field. While the continuous film exhibits a well defined loop with an exchange bias field $H_{eb} \approx 200\,Oe$, the hysteresis curves measured on the patterns present some features related to the irradiated geometries. First of all we notice that loops of patterns b and d (Fig. 1, bottom graphs) are clearly different from the continuous film loop, while for patterns a and c (Fig. 1, middle graphs) only slight differences are visible. More in detail, in curves b and d two different contributions can be identified, corresponding to the magnetization reversal process in irradiated and non-irradiated areas. As expected irradiated areas present nearly unbiased behavior with $H_{eb} \approx 50\,Oe$ and smaller coercivity, whereas the unpatterned areas are responsible for that part of the curve exhibiting larger H_{eb} and coercivity. It is worth noting that the percentage of unbiased magnetization corresponds to the fractional coverage of irradiated areas, that is 75% in pattern b and 25% in pattern d. Finally, unbiased and biased parts of both the curves are connected through a narrow but still open area of the hysteresis,

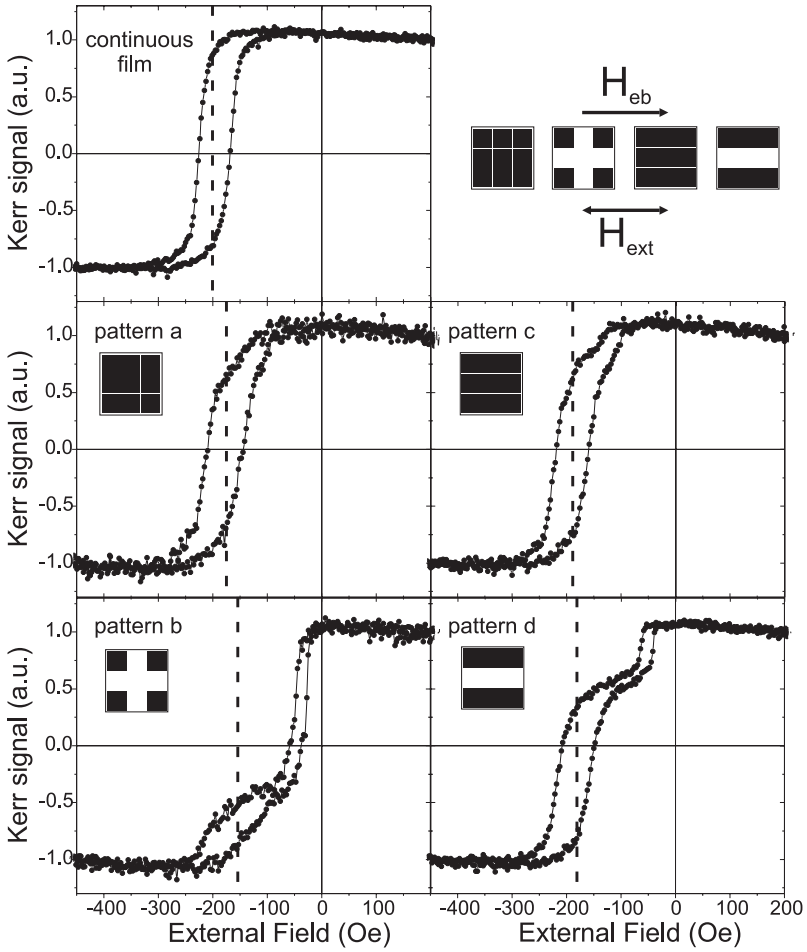

Fig. 1: Hysteresis loops measured by MOKE on the continuous film and the irradiated patterns; the drawing shows the orientations of exchange bias field and external field with respect to the irradiated structures. Among the loops of patterned areas we can easily distinguish patterns a and c (middle graphs) from patterns b and d (bottom graphs): the latter ones are clearly different from the continuous film loop and correspond to patterns with larger irradiated areas, while the former ones present only slight differences from the continuous film loop and correspond to smaller irradiated areas.The dashed lines indicate the value of H_{eb} for non-irradiated areas of each pattern.

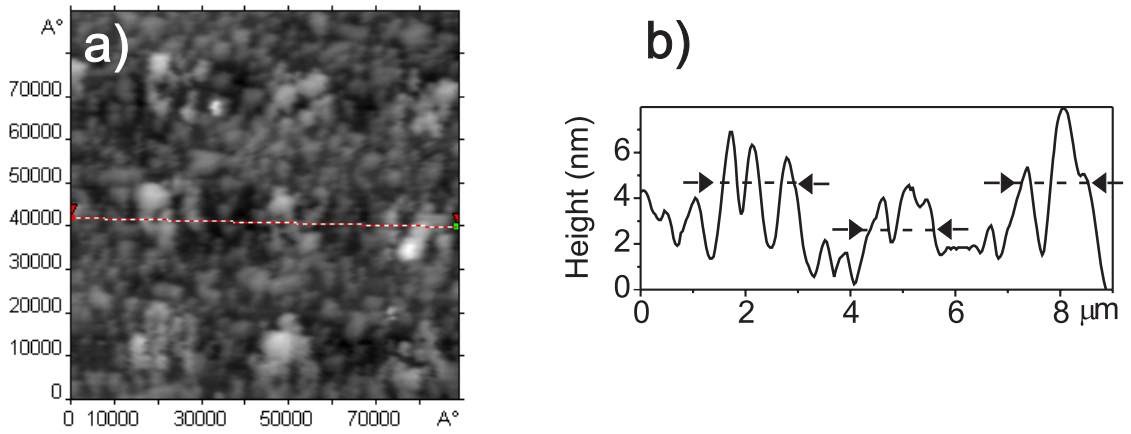

Fig. 2: Topography of pattern b measured by atomic force microscopy. (a) $9 \times 9\,\mu m^2$ AFM image. (b) Height profile measured along the line reported in (a); the arrows are indicating non-irradiated areas.

thus indicating that the reversal process in irradiated and non-irradiated regions is not proceeding independently; this coupling effect is more evident in curve b, in which the biased part is also bent towards smaller values of H_{eb}. The exchange coupling between irradiated and non-irradiated areas produces even more dramatic effects on the reversal process of patterns a and c. As shown in Fig. 1, the loops are almost completely biased and deviations from the continuous film hysteresis can be observed only in the lower part of the curves, which are slightly bent towards smaller H_{eb} values. This biased behavior indicates that the magnetization reversal in the small irradiated, unbiased areas is dominated by the exchange coupling with the larger biased regions. As a consequence the magnetic evolution of the biased areas governs the behavior of the whole magnetic film.

The magnetic behavior of pattern b during the magnetization reversal process was further investigated by means of MFM. For this purpose a multifunctional scanning probe microscope was used (Solver AFM-MFM produced by NT-MDT Co.). Figure 2 shows the sample topography in the region of pattern b. An evident surface roughness is present in both irradiated and non-irradiated areas (Fig. 2a), thus suggesting that the roughness is due to the deposition process rather than due to the ion patterning, as reported also elsewhere [8]. In Fig. 2b the height profile is shown, with arrows indicating the non-irradiated areas. As seen from the figure, ion patterning slightly smoothed the surface in the irradiated areas, producing also some steps near the boundaries. We can evaluate the steps height, i.e. the surface damage caused by irradiation, comparing the average levels of irradiated and non-irradiated regions. The result is ranging from 1 to 3 nm, corresponding to the thickness of the Cr capping layer and the first monolayers of the $Fe_{50}Mn_{50}$ antiferromagnet.

Figure 3b reports $9 \times 9\,\mu m^2$ MFM images of pattern b for different values of the external magnetic field. The external field is applied parallel to the exchange bias field direction (horizontal axis of the images) and it is increased from -400 Oe up to 0 Oe. Complete saturation is expected for a field of -400 Oe, but shadows of the square elements are still visible in Fig. 3-1; this is likely caused by topographical influences on the magnetic signal, due to the presence of the above mentioned steps. The following images clearly show that in the non-irradiated squares the magnetization reversal starts first with respect to the surrounding film: for external fields of -150 (Fig. 3-2) and -100 Oe (Fig. 3-3) it is evident that domain structures are nucleating inside the squares, while the film looks still uniform. For an external field of -50 Oe (Fig. 3-4) the reversal process is proceeding also in the non-biased regions, as demonstrated by the presence of different orientations for the magnetization (bright and dark regions), but the square elements are not yet saturated and a clear

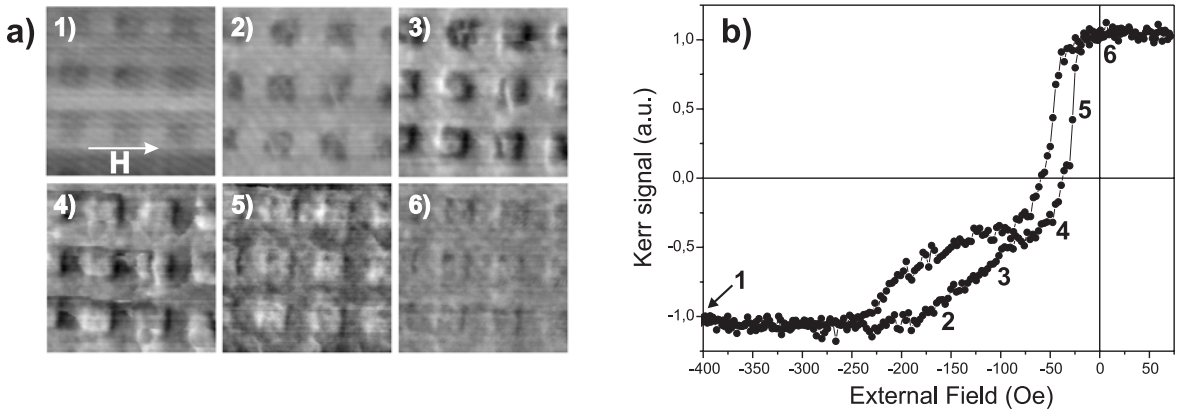

Fig. 3: MFM images of pattern b recorded along the increasing branch of the hysteresis loop. a): points of the hysteresis loop for which MFM images are recorded. b): $9 \times 9\,\mu m^2$ MFM images of pattern b for increasing values of external field: -400 Oe (1), -150 Oe (2), -100 Oe (3), -50 Oe(4) , -25 Oe (5), 0 Oe (6). The positive direction of the applied field is indicated by the arrow in image (1).

magnetic contrast is still present inside these biased areas. A further increasing of the external field up to -25 Oe (Fig. 3-5) and 0 Oe (Fig. 3-6) produces more uniform configurations, with an irregular domain structure homogeneously distributed over both the irradiated and non-irradiated areas. This weak magnetic contrast still visible at the saturation (0 Oe) indicates the presence of magnetic fluctuations due to the surface roughness as well as to the polycrystalline nature of the sample.

We want to focus the attention on the MFM image recorded for an external field of -50 Oe (Fig. 3-4). From the hysteresis loop (Fig. 1, pattern b) we see that -50 Oe is the field dividing the biased part of the curve from the unbiased one. Hence, the corresponding MFM image could be expected to show both the biased squares and the surrounding unbiased areas in a saturated state, but with opposite directions of the magnetization. Instead Fig. 3-4 shows a totally different scenario, with domain walls observable inside the squares and almost reversed regions (dark areas) developing from the squares borders into the surrounding film. This configuration is the result of direct exchange coupling between irradiated and non-irradiated regions: on one hand the reversal process inside the squares is promoting the magnetization reversal in the neighboring film; on the other hand the non-reversed film regions are stabilizing non-saturated configurations in the biased squares, well below the saturation field of the continuous exchange bias film.

The present results are in agreement with a previous study [9] developed on a similar magnetic pattern. In Ref. [9] ion irradiated $Ni_{81}Fe_{19}/Fe_{50}Mn_{50}$ unbiased $5 \times 5\,\mu m^2$ squares with 5 µm spacings were investigated by MOKE and MFM. The MFM images highlighted the presence of regions with lateral dimensions of $1-2$ µm, whose magnetic properties are affected by the direct exchange coupling between irradiated and non-irradiated areas. However MOKE hysteresis loops showed well separated contributions from the biased and unbiased regions, revealing that this magnetic coupling is not playing an important role in the reversal process. This disagreement with our present results is surely due to the different dimensions of the irradiated areas, 5 µm in Ref. [9] and 1.5 µm in the present case. As a conclusion, the exchange coupling between irradiated and non-irradiated areas produces a remarkable effect on the magnetization reversal process when the lateral size of irradiated elements approaches a characteristic coupling length; for $Ni_{81}Fe_{19}/Fe_{50}Mn_{50}$ exchange bias bilayers this coupling length is found to be approximately 1.5 µm, in agreement with the MFM observations reported in ref. [9].

This work is supported in part by the EU-RTN NEXBIAS (HPRN-CT-2002-00296).

References

[1] W.H. Meiklejohn, C.P. Bean, Phys. Rev. **102**, 1413 (1956).
[2] T. Mewes, R. Lopusnik, J. Fassbender, B. Hillebrands, M. Jung, D. Engel, A. Ehresmann, H. Schmoranzer, Appl. Phys. Lett. **76**, 1057 (2000).
[3] A. Mougin, T. Mewes, D. Engel, A. Ehresmann, H. Schmoranzer, J. Fassbender, B. Hillebrands, Phys. Rev. B **63**, 060409 (2001).
[4] S. Blomeier, D. McGrouther, R. O'Neill, S. McVitie, J.N. Chapman, M.C. Weber, B. Hillebrands, J. Fassbender, J. Magn. Magn. Mater. **290-291**, 731 (2005).
[5] C. Chappert, H. Bernas, J. Ferré , V. Kottler, J.P. Jamet, Y. Chen, E. Cambril, T. Devolder, F. Rousseaux, V. Mathet, H. Launois, Science **280**, 1919 (1998).
[6] V.E. Demidov, D.I. Kholin, S.O. Demokritov, B. Hillebrands, F. Wegelin, J. Marien, Appl. Phys. Lett. **84**, 2853 (2004).
[7] S. Blomeier, B. Hillebrands, V.E. Demidov, S.O. Demokritov, B. Reuscher, A. Brodyanski, M. Kopnarski, J. Appl. Phys., in press.
[8] S. Blomeier, D. McGrouther, S. McVitie, J.N. Chapman, M.C. Weber, B. Hillebrands, J. Fassbender, Eur. Phys. J. B **45**, 213 (2005).
[9] A. Mougin, S. Poppe, J. Fassbender, B. Hillebrands, G. Faini, U. Ebels, M. Jung, D. Engel, A. Ehresmann, H. Schmoranzer, J. Appl. Phys. **89**, 6606 (2001).

D. Transfer of Technology

6.16 Construction of a phase-sensitive, space and time resolved Brillouin light scattering spectroscopy setup

A.A. Serga, T. Schneider, and B. Hillebrands[1]

Recently we reported on the development and application of the space- and time-resolved Brillouin light scattering spectroscopy technique [1–3]. It is based on a multipass tandem Fabry-Pérot interferometer reported elsewhere [4]. This technique allows us to map the spin wave intensity distribution across the sample with space and time resolution of 30 µm and 1.8 ns, respectively. Thus the behavior of one- and two-dimensional spin wave packets, such as spin wave envelope solitons and bullets, can be accessed addressing issues such as free propagation, collision, parametric amplification and phase conjugation, see, e.g., [5–7]. However, for detection photon counting is used, which, in a conventional setup, allows only to measure a signal proportional to the *square* of the precession angle of the spin wave, i.e., proportional to the spin wave intensity. The phase of the spin wave was not accessible by this method so far. Here we report on the first implementation of phase sensitivity into Brillouin light scattering spectroscopy. This allows now for access to quantities such as the phase profile and the wave front of a spin wave packet.

In order to access phase information, interference between the signal picked up from the spin wave under investigation and a coherent reference signal can be used. For example, to study the phase of a spin wave signal in a conventional microwave setup using an output antenna for detection, the picked up signal is mixed with a coherent reference wave derived from a common microwave oscillator. The resulting interference patterns contain information both on the amplitude and on the phase of the signal. Measurements as a function of the phase shift of the reference signal allows for the separation between the amplitude and the phase of the signal. Reference [8] provides an example of this approach.

In case of Brillouin light scattering spectroscopy the light inelastically scattered from the spin waves contains information both on the amplitude and the phase of the spin wave. In order to access the phase information an interferometric approach has been chosen using a geometry as displayed in Fig. 1.

Designing an optical interferometer setup, mechanical and thermal stability is of paramount importance to yield reliable phase information. In principle, a Mach-Zehnder type approach could be chosen. Here the light from the laser is divided into two branches. The light in the first branch is focused down on the sample, and the light inelastically scattered from the spin waves is collected and frequency filtered by the tandem Fabry-Pérot interferometer. The light of the second interferometer branch is shifted in frequency by exactly the same amount using an optical frequency shifter. This can be achieved by using a common microwave oscillator to drive the antenna to generate the spin waves and the frequency shifter. Finally, both branches are brought to interference and the interference pattern is detected using the photomultiplier.

It is evident, that any fluctuations in one of the two interferometer branches will result in undesirably large errors of the detected phase. Thus we have developed a different interferometric

[1] In collaboration with S.O. Demokritov and V. Demidov, Institut für Angewandte Physik, Westfälische Wilhelms-Universität, Münster, Germany.

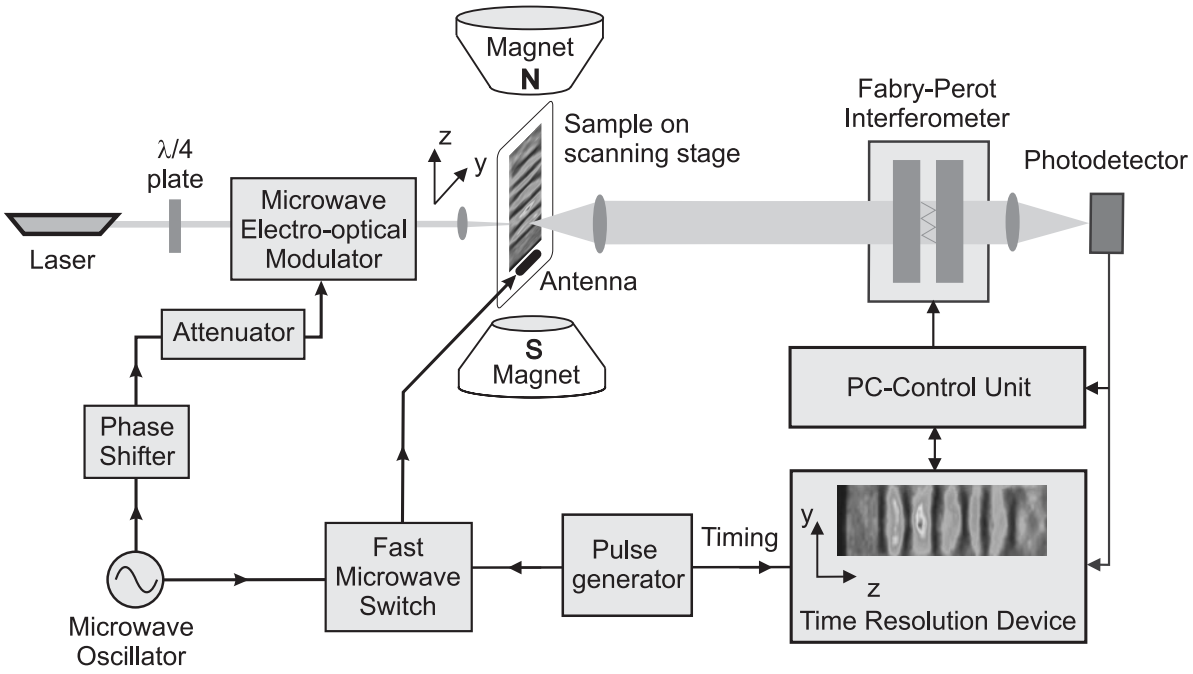

Fig. 1: Time- and space-resolved phase sensitive Brillouin light scatteringsetup.

approach which provides superior stability against vibrations, mechanical drift and thermal fluctuations.

We have solved the problem by spatially combining the optical reference and the signal beam along one single axis. The frequency shifted reference light is created here by means of phase modulation of the incident laser beam using an electro-optical resonance modulator, see Fig. 1. The modulation amplitude is chosen to be very small, such that the intensity of the frequency shifted light is of the same order as the intensity of the light inelastically scattered by the spin waves.

To achieve the necessary frequency shift, a microwave electro-optical resonance modulator based on a Lithium Niobate (LNB) single crystal placed in a microwave cavity was constructed. As this modulator is driven by the same microwave source that is used for the excitation of the spin waves coherency between the frequency shifted and the inelastically scattered light guaranteed.

As shown in Fig. 1 the signal from the microwave oscillator is first channelled through a phase shifter and attenuator. This allows one to tune the intensity and initial phase of the reference signal. To create the microwave pulses, the part of the signal used to excite the spin waves is passed through a fast switch, which is synchronized with the time resolution part of the time resolved Brillouin light scattering setup.

Light inelastically scattered from spin waves is rotated by 90° in polarization. In order to have interference with the light shifted in frequency by the electro-optical modulator, an optical $\lambda/4$ plate is used to convert the laser light into circularly polarized light before it enters the modulator.

Figure 2 demonstrates the first results obtained with the described setup. The spin wave pulses propagating in a film stripe of yttrium iron garnet (YIG) are shown here for a given moment of time. The width and thickness are 1.5 mm and 6 µm, respectively. The pulse duration is 200 µs, and the carrier frequency is 7.125 GHz. The measurements are performed for two different values of the magnetizing field $H = 1838$ Oe and $H = 1858$ Oe. The spin wave microstrip antenna is placed

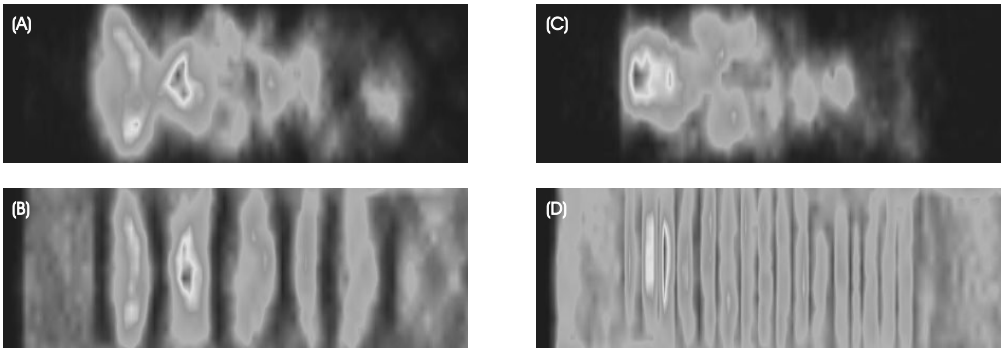

Fig. 2: Phase resolved measurements of spin wave pulses. The upper diagrams are obtained without the reference light and show the spin wave intensity distribution for a given time frame. The lower pictures show the corresponding phase maps. The pulse duration and the carrier frequency are 200 µs and 7.125 GHz, respectively. The applied field is (a)-(b) – $H = 1838$ Oe, (c)-(d) – $H = 1858$ Oe.

near the left side of the YIG stripe. The field is oriented parallel to the propagation direction, and thus a packet of backward volume magnetostatic spin waves (BVMSW) is excited. The results are represented in linear false-grey code. The upper figures, which are obtained without the reference light, show the distribution of the spin wave intensity. This intensity decays from left to right due to decay of the spin wave. The patterned structure of the packets is created by beating of spin wave modes in the YIG waveguide. The lower figures show the corresponding phase maps, i.e., for a given moment of time the square of the product of amplitude and phase factor. The observed regular oscillating structure corroborates the expected phase sensitivity. The phase fronts are clear visible. In full accordance with the known BVMSW's properties the observed wavelength decreases with an increase of the magnetizing field. The measured values of the wavelength corresponds well with the calculated one.

Support by the Deutsche Forschungsgemeinschaft is gratefully acknowledged.

References

[1] M. Bauer, O. Büttner, S.O. Demokritov, B. Hillebrands, V. Grimalsky, Yu. Rapoport, A.N. Slavin, Phys. Rev. Lett. **81**, 3769 (1998).
[2] S.O. Demokritov, B. Hillebrands, A.N. Slavin, Phys. Rep. **348**, 441 (2001).
[3] O. Büttner, M. Bauer, S.O. Demokritov, B. Hillebrands, Yu.S. Kivshar, V. Grimalsky, Yu. Rapoport, A.N. Slavin, Phys. Rev. B **61**, 11576 (2000).
[4] B. Hillebrands, Rev. Sci. Instr. **70**, 1589 (1999).
[5] A.A. Serga, B. Hillebrands, S.O. Demokritov, A.N. Slavin, Phys. Rev. Lett. **92**, 117203 (2004).
[6] A.N. Slavin, . Büttner, M. Bauer, S.O. Demokritov, B. Hillebrands, M.P. Kostylev, B.A. Kalinikos, V. Grimalsky, Yu. Rapoport, Chaos **13**, 693 (2003).
[7] A.A. Serga, B. Hillebrands, S.O. Demokritov, A.N. Slavin, P. Wierzbicki, V. Vasyuchka, O. Dzyapko, A. Chumak, Phys. Rev. Lett. **94**, 167202 (2005).
[8] S.O. Demokritov, A.A. Serga, V.E. Demidov, B. Hillebrands, M.P. Kostylev, B.A. Kalinikos, Nature **426**, 159 (2003).

6.17 3D coplanar waveguide design using organic isolation layers

P. Martín Pimentel, S. Hermsdörfer, H.T. Nembach, B. Leven, and B. Hillebrands[1]

Improvement of non-volatile data storage media like magnetic random access memories (MRAM) is of elementary importance for future data storage. For achieving ultrafast switching in the GHz range it is necessary to investigate single domain elements with a well defined Stoner-like magnetization reversal behavior. Recent publications [1, 2] report on ellipsoidally shaped synthetic antiferromagnet (SAF) elements used as the active switching part in MRAM cells. Switching was initiated by two orthogonally oriented, time delayed in-plane magnetic field pulses being aligned at an angle of $\pm 45^\circ$ with respect to the in-plane magnetic easy axis of the element. The main disadvantages of this concept are the low switching speed and the necessity for a pre-read step prior to the writing process. An improvement of the switching concept for precession-dominated switching of SAF elements could recently be demonstrated by simulations [3,4] allowing for ultrafast switching and a direct writing scheme without pre-read. To investigate this precession-dominated switching process experimentally by means of time-resolved magneto-optical Kerr effect microscopy, a double layer structure of high quality crossed coplanar waveguide (CPW) structures is required to apply the suggested two independent magnetic field pulses. For achieving ultrafast rise time field pulses, a bandwidth of the CPW in the GHz range is required. This report addresses the development and preparation of such CPW structures by using the photosensitive polymer Cyclotene 4024-40^{TM} (hereafter referred to as BCB, Dow Chemical) as electric insulation layer. This polymer guarantees for good electrical insulation (volume resistivity $\rho \simeq 1 \cdot 10^{19}\,\Omega$m [5]) as well as an extremely high surface planarization (about 90% [6, 7]), which is an essential requirement for the quality of the applied field pulses and for the magnetic properties of the SAF element. We demonstrate the fabrication of a BCB based CPW multilayer stack feasible for such applications.

The newly developed crossed CPW design consists of six different layers, three conducting lines, two BCB insulation layers and, on top, the magnetic thin film element. The setup is shown schematically in Fig. 1.

In this figure, the layer thickness as well as the width of the CPW lines are displayed to scale. The substrate is a B270 glass substrate (dielectric constant $\varepsilon = 7.0$). The first layer on top of the sub-

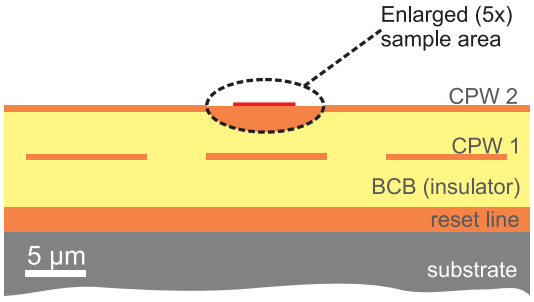

Fig. 1: Schematic cross section of the crossed CPW multilayer sample design. The film thicknesses and CPW dimensions are drawn to scale. The sample area has been enlarged by a scaling factor of five to demonstrate the position of the magnetic thin film element.

[1] In collaboration with S. Trellenkamp and S. Wolff from the Nano+Bio Center, Technische Universität Kaiserslautern, Germany.

strate is a microstructured Cu stripline, the so-called reset line produced either by using a shadow mask or by UV-photo lithography and lift-off. This reset line allows to reset the initial magnetization state of the investigated magnetic element. This is required for the stroboscopic measurement technique used for the investigation of the magnetization dynamics. The film thickness is 2 µm and the width of the reset line is 100 µm in the central constriction and 350 µm elsewhere. The central constriction of the reset line is used to increase the output Oersted field. The second layer, which is the first BCB insulation layer, is processed by UV photolithography and lift-off where the contacts of the reset line are uncovered areas at the ends for electrical contacting. The following first coplanar waveguide CPW 1 is oriented at an angle of $+45^\circ$ with respect to the reset line. The second BCB insulation layer also leaves open areas for electrical contacting of CPW 1 and the reset line. CPW 2 is then positioned on top of this second insulation layer and oriented at an angle of -45° with respect to the reset line, i.e., the coplanar waveguides are orthogonal to each other. The film thickness of the CPWs is 500 nm and the impedance is 50 Ω. Finally, on top of the whole setup, a magnetic thin film element is prepared in the central area of the CPW cross (see Fig. 2) by means of electron beam lithography and lift-off.

Fig. 2 shows an optical micrograph of the central structure region. The sampling area is $10 \times 10\,\mu m^2$, defined by the squared width of the central signal lines of the CPWs.

The micropatterning of the conduction lines (i.e., the reset line and CPWs) is carried out by UV-photo lithography using a negative lift-off process. The resist used is AZ 5214-E (Clariant). In order to pattern the reset line a pre-treatment with the adhesion promotor hexamethyldisilazane (HMDS) is required prior to the resist coating. After spin-coating the resist and several other steps including soft bake and UV-exposures, the resist is finally developed in AZ 400K (Clariant) and in deionized water. After depositing the Cu by electron beam evaporation the lift-off is carried out in acetone.

The signal processing of the CPWs is extremely sensitive to the planarity of the structure. Any edges due to underlined microstructure cause reflection losses and thus additional noise. This high degree of planarity cannot be achieved by standard insulators used so far and made it necessary to develope a multilayer BCB process which yields the highly insulating, structurable and planar films. Figure 3 shows a typical result achieved after processing. Shown is a secondary electron micrograph of the cross section of a BCB multilayer sample including a Cu CPW. The planarization of the CPW with the BCB is very good as no surface profile caused by the CPW can be observed. Furthermore, good adhesion between the different BCB layers is achieved as no interface can be

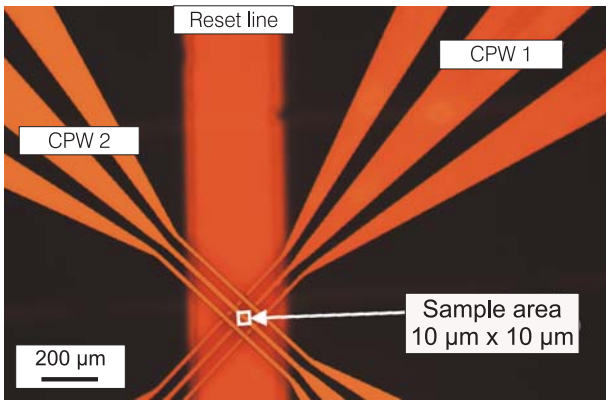

Fig. 2: Optical micrograph of the crossed CPW design (top view). The reset line and both CPWs are visible whereas the BCB insulation layers are transparent.

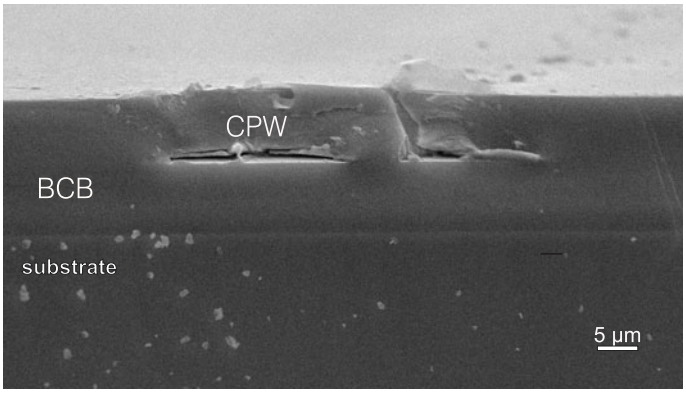

Fig. 3: SEM micrograph of the cross section of a CPW sandwiched between two successively processed BCB insulation layers.

detected between the two BCB layers. These qualities guarantee for good insulation and very good high frequency characteristics.

The elliptical magnetic thin film element (dimensions: $2 \times 1\,\mu m^2$) is prepared on top of CPW 2 by means of electron beam lithography, and oriented orthogonally to the reset line.

To demonstrate the quality of the device, the transmission characteristics of the CPWs is measured with the experimental setup shown in Fig. 4. The sample is mounted in the center on top of a post and contacted with special spring contacts providing three parallel arranged needle-contacts. These so-called picoprobes® (GGB Industries, Inc.) are fixed in holders with integrated *x*-, *y*- and *z*-positioning stages enabling an exact adjustment of the uncovered contacts ends of the CPWs.

The transmission characteristic is measured in the range of 200 MHz up to 15 GHz using a scalar network analyzer. According to the 3 dB criterion the bandwidth is larger than 10 GHz. These measurement prove the good quality of the CPWs and prove the waveguide design presented here is feasible for the measuring of ultrafast magnetization reversal processes as requested in [3, 4].

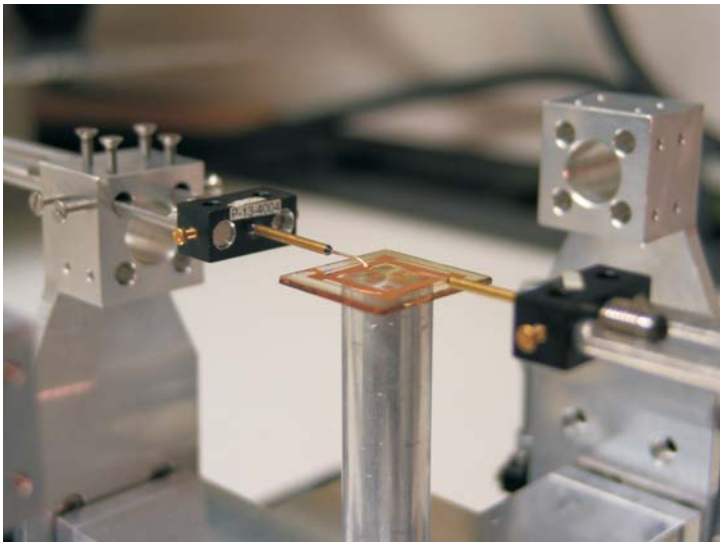

Fig. 4: Experimental setup to apply the high quality magnetic field pulses using so-called picoprobe® contacts. In the center the sample can be seen surrounded by the adjustable mountings of the picoprobe®. To provide a clear overview only two picoprobes® are mounted.

In conclusion, the applicability of polymer insulation layers in a 3D crossed CPW design for ultrafast magnetization measurements was demonstrated. It is possible to integrate BCB into a multilayer sample structure, which allows for high electrical insulation and high surface planarization. The micropatterned CPWs have a bandwidth larger than 10 GHz according to the 3 dB criterion which is of fundamental importance for the field pulse quality. This new technique has considerable potential for further application in the processing of 3D sample structures.

The authors thank Mireia Blanco Mantecón for support in structure design, Burkhard Stahlmecke and Günter Dumpich (University of Duisburg-Essen, Germany) for performing the electron beam lithography and Andreas Beck and Roland Mattheis (IPHT Jena, Germany) for the magnetic thin film deposition. The authors wish to thank Dow Chemical for supplying the Cyclotene 4024-40^{TM}.

Financial support by the European Commission within the EU-RTN ULTRASWITCH (HPRN-CT-2002-00318) and the EU-STREP project MAGLOG (FP6-510993) is gratefully acknowledged.

References

[1] B.N. Engel, J. Akerman, B. Butcher, R.W. Dave, M. Durlam, G. Grynkewich, J. Janesky, S.V. Pietambaram, N.D. Rizzo, J.M. Saughter, K. Smith, J.J. Sun, and S. Tehrani, Proceedings of the Joint MMM-Intermag 2004, Anaheim, CA, IEEE **41**, 132 (2005).
[2] L. Savtchenko et al., US Patent 6,545,906 B1, Apr. 8 (2003).
[3] Joo-Von Kim, T. Devolder, C. Chappert, Appl. Phys. Lett. **85**, 4094, (2004).
[4] H.T. Nembach, C. Bayer, H. Schultheiss, M.C. Weber, P. Martín Pimentel, P.A. Beck, B. Leven, B. Hillebrands, Appl. Phys. Lett. **87**, 142503, (2005).
[5] Processing Procedures for CYCLOTENE 4000 series Photo-BCB Resins, CYCLOTENE Advanced Electronic Resins, Dow Chemical, http://www.dow.com/cyclotene, Revised version: February 2005.
[6] T.A. Manial, R.H. Heistand, P. Garrou, Surf. Mount Int. Conf. Expo. Proc. **1**, 39 (1992).
[7] S. Wolff, A.R. Giehl, M. Renno, H. Fouckhardt, Appl. Physics B **73**, 623-627 (2001).
[8] B. Stahlmecke, Diploma Thesis, University of Duisburg, Germany (2001).

6.18 Mode-crossing in the spectrum of surface excitations in tungsten carbide films

T. Wittkowski, G. Distler, K. Jung, and B. Hillebrands[1]

Brillouin light scattering spectroscopy (BLS) of acoustic excitations in the GHz frequency range is an elegant method for the determination of the effective elastic constants of thin films [1, 2]. In general the properties of thin supported films of tungsten carbide depend quite markedly on the preparation conditions [3–5]. For the present study films were prepared by unbalanced rf magnetron sputtering of a WC target in an Ar atmosphere. In order to achieve optimized sample properties for the intended analysis with BLS these films were prepared in a steplike manner. This deposition technique led to different film thicknesses at different positions on the substrate. Such samples were prepared in a single deposition run thus ensuring the lateral uniformity of the films [3]. In order to determine the effective elastic constants and the mass density from the Brillouin investigations, the velocity dispersion of the sagittal modes - the only detectable acoustic modes in metallic tungsten carbide films - needs to be analyzed. Besides the relevant material properties, namely the respective stiffness constants and the mass density of the film and the substrate, the dispersion depends only on the dimensionless product of the parallel phonon wavevector, $q_{\parallel}$, and the film thickness d. Owing to the well known properties of the silicon substrate, the experimental data allow the extraction of the four effective elastic constants c_{ij} and the mass density of the films, ρ, by the classical method of a least squares fitting routine in which the minimization of

$$\chi^2 = \sum_{i=1}^{n} w_i \left(\nu_i^{(\mathrm{meas})} - \nu_i^{(\mathrm{calc})} \right)^2 \tag{1}$$

is performed. The phase velocities $\nu_i^{(\mathrm{meas})}$ are obtained from the experiment, the $\nu_i^{(\mathrm{calc})}$ are calculated by solving the equation of motion under the appropriate boundary conditions [6]. The weighting factors w_i were determined from the individual measurement errors of the n data points.

Besides the classical method of extraction of the elastic constants discussed above, two other theoretical methods are of relevance to the analysis of the BS results of the present experiments. These are the surface elastodynamic Green's function approach that provides the relative scattering efficiency of the surface ripple mechanism for opaque materials, and the recently developed Monte Carlo (MC) method for the extraction of the elastic constants.

The Green's function method is described in detail in Ref. [7] and hence a brief account is given. At temperatures T at room temperature and above, the scattering efficiency is proportional to

$$I(\omega) = A \frac{T}{\omega} \, Im \left\{ G_{33}(q_{\parallel}, x_3 = -d, \omega + i0) \right\} \tag{2}$$

where the pre-factor A depends on the properties of the medium, the scattering geometry and the frequency and polarization of the incident light. The Green's tensor component G_{33} is determined in terms of the partial waves that satisfy the boundary conditions at the free surface for a thin film of

[1] In collaboration with J.D. Comins, DST/NRF Centre of Excellence in Strong Materials and Materials Physics Research Institute, School of Physics, University of the Whitewatersrand, Johannesburg, Wits 2050, South Africa.

thickness d. The simulated spectra reproduce the discrete surface modes, as well as the continuum of excitations resulting from bulk mode displacements of the surface and within which pseudo-surface modes and damped resonances may have significant intensity. Accordingly the calculated spectra can be employed to fit experimental velocity dispersion curves (ν_i vs. $q_{\|}d$) directly as in the classical method. Alternatively, the results can be used as an adjunct to the classical methods discussed above in which only the discrete modes are considered and where spectral intensity information in the dispersion is lacking. As discussed further below, the intensities of the spectral features provided by the Green's function approach can be crucial in mode assignments.

The MC method applied to the extraction of the c_{ij} and ρ has been discussed and applied in Ref. [3]. Proceeding from the velocity dispersion curves (ν_i vs. $q_{\|}d$), new data sets in number equal to the data points used in the classical fitting procedure are generated by a random variation of quintuplets of the free parameters (c_{ij} and ρ). The weighted χ^2-sum for each parameter set is then computed from Eq. (1). The method determines the absolute and relative minima of an objective function, these being the minima in the χ^2-sum in a multidimensional space. In order to better visualize the results appropriate projections of the parameter space, which is five-dimensional in the present study, into two-dimensional subspaces can be made. The MC method requires only the experimental data as input and, as will be shown in the present context, it is not necessary to make mode assignments for the data points as is required in the classical fitting procedure.

This particular advantage of the MC procedure over the classical least squares fitting of the velocity dispersion is illustrated using the results from a stepped tungsten carbide film deposited with a kinetic energy of the Ar^+ ions of 136 eV. As noted before, the MC procedure does not require an assignment of the measured velocities to a particular mode order, being extremely important in cases where the mode order is ambiguous or appears to be unambiguous from examination of the experimental data only. Such a situation occurs in the film deposited with an ion energy of 136 eV as is shown in Fig. 1. The lower graph shows the measured points indicated by circles, squares, and triangles where each symbol corresponds to a particular thickness of the stepped film. It is noted that the data points of the apparent excitation with the highest velocity seem to form a continuous line thus suggesting that these data might be assigned to the 2^{nd} Sezawa mode. Any least squares fit requires a mode order assignment, in turn leading to the least squares solution. Should this mode assignment be incorrect the non-linear fitting routine will achieve a local minimum of the objective function but corresponding to the incorrect prior assumption. Such a situation is effectively avoided if, (a) the algorithm does not require a mode order assignment, and (b) the parameter search intervals are sufficiently large to ensure that the investigation of the objective function is not constrained in the vicinity of a local minimum.

The MC procedure is an algorithm of this type and it convincingly overcomes the above mentioned problem. Using the velocity data as the only experimental input without the need of a mode order assignment, the statistical analysis yields an initial set of the elastic constants and the mass density of the film corresponding to the minimum sum of squares. This solution when used to calculate the velocity dispersion now permitted an unambigous mode order assignment. Figure 2 shows selected results of the MC approach. It presents the projection of randomly varied parameter sets of the five-dimensional parameter space into the two-dimensional (c_{55}, ρ)-plane. Those parameter quintuplets that correspond to the minimum sum of squares are used as the initial set of values in the least squares fitting routine.

The final set of elastic constants was obtained in a subsequent least squares fitting routine which uses the correctly determined mode order assignments with the initial set of values as starting parameters (result shown as curves in the lower graph of Fig. 1). The large number of data points

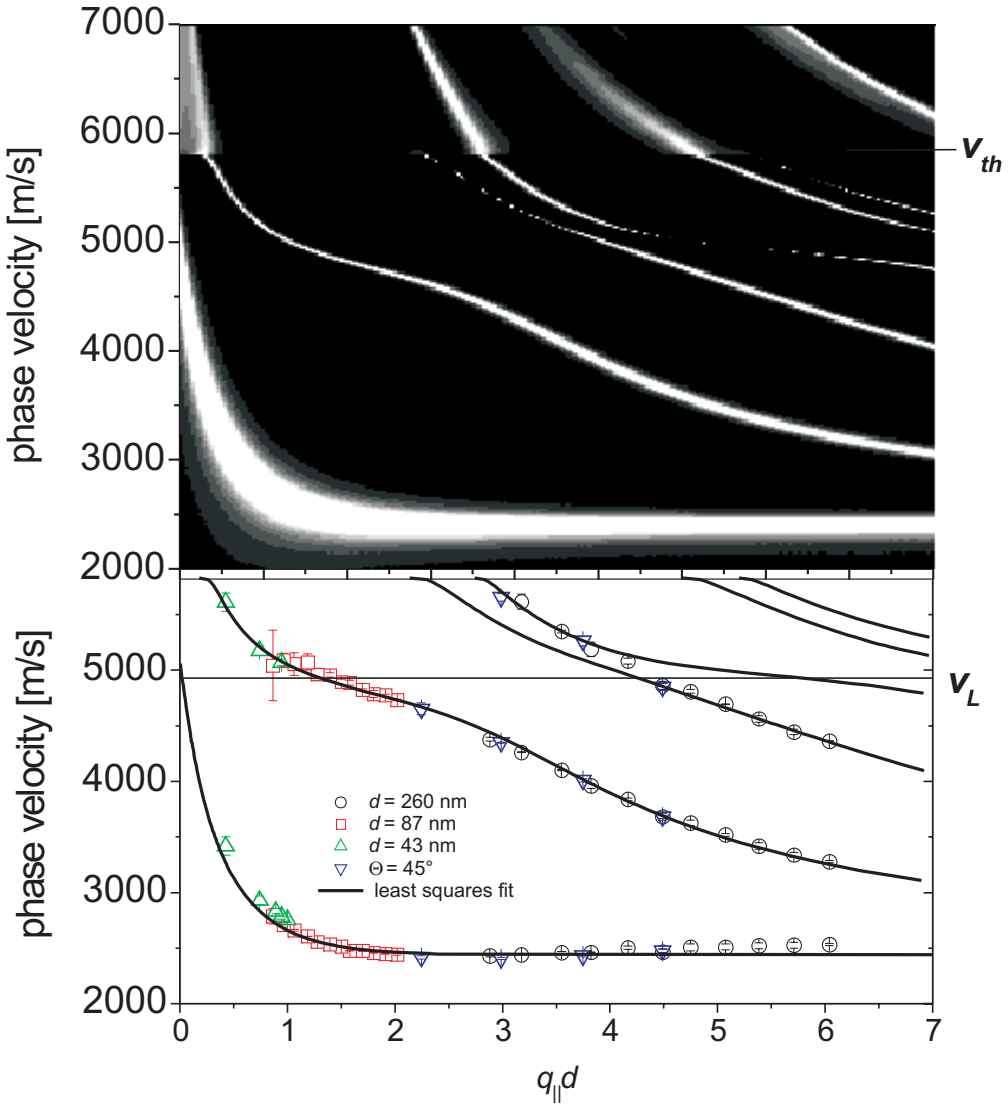

Fig. 1: Phase velocities as a function of the product of parallel phonon wavevector $q_{||}$ and film thickness d. Points in the lower graph indicate the measured velocities obtained from a tungsten carbide film with six steps of different thickness. Each symbol corresponds to a particular film thickness except for the down-triangles where the wavevector was kept constant. The lines show the velocity dispersion curves calculated from the least squares fit result $\rho = 16.8 \pm 0.2\,\mathrm{g/cm^3}$, $c_{11} = 409 \pm 10\,\mathrm{GPa}$, $c_{13} = 105 \pm 11\,\mathrm{GPa}$, $c_{33} = 399 \pm 17\,\mathrm{GPa}$, and $c_{55} = 111 \pm 2\,\mathrm{GPa}$. With these constants the scattered intensities were calculated by the Green's function method (upper graph). Bright curves correspond to a high scattered intensity, dark regions to a low intensity. Horizontal lines indicate the longitudinal sound velocity parallel to the film, v_L (lower graph) and the transverse wave threshold, v_{th} (upper graph). The overall agreement between the measured velocities and the calculated velocities and intensities is good. In particular the mode-crossing between the 2nd and 3rd Sezawa mode as predicted from the MC analysis is confirmed convincingly by the Green's function method.

(75), the four sagittal modes, and the distribution of measured velocities over a wide range of the dispersion curve leads to the reliable extraction of the four elastic constants and the mass density. A Green's function calculation of the scattered intensities using these data (upper graph of Fig. 1) provides clear confirmation of the correctness of the mode assignments. From the respective mode intensities, the data corresponding to the excitations of highest velocity must be assigned to the 2nd Sezawa mode for $q_{||}d > 4$ and to the 3rd Sezawa mode for $q_{||}d < 4$. This so-called mode-crossing is characterized by an abrupt change in scattering intensity in moving from the second to the third Sezawa mode where the respective Sezawa velocities are near the longitudinal sound

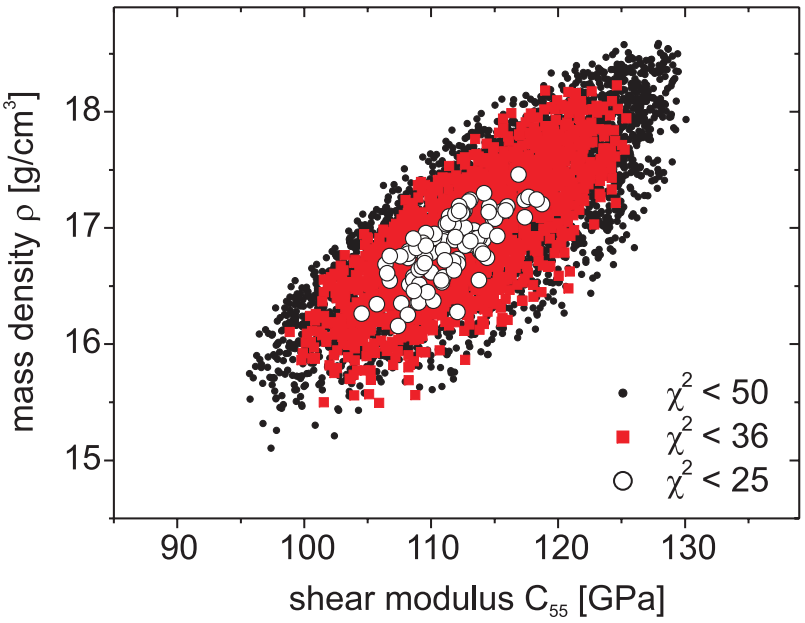

Fig. 2: Projection of randomly varied parameter sets of the five-dimensional parameter space into the two-dimensional (c_{55}, ρ)-plane as determined with the MC approach. Those parameter quintuplets that correspond to the minimum sum of squares make up the initial set of values in the subsequent least squares fitting routine. Calculating and plotting the dispersion with the initial set of values allows for an unambiguous assignment of the measured excitations to the correct mode order.

velocity parallel to the film, namely $v_L = 4931\,\mathrm{m/s}$.

It is also noted from Fig. 1 that there is a small deviation of the measured points from the calculated least squares velocity dispersion in certain regions, being most pronounced for the Rayleigh mode at $q_{||}d$ values greater than 5. Within the hexagonal model it is not possible to find a single set of elastic constants that would provide a better representation of the measurement. This lack of agreement results from the limitations of the effective elastic constant model which assumes the film properties to be independent of the film thickness. For the sample under investigation the high precision Brillouin measurements provide evidence that this film material slightly alters its microstructure as a function of the distance from the interface. The increase of the measured Rayleigh velocity in the limit of large $q_{||}d$ indicates a moderate shear stiffening of the film with increasing thickness. This effect was not present in the results obtained from tungsten carbide films deposited at the lower ion energies.

In summary it was shown how the combination of three techniques of analyzing surface excitations in thin supported films leads to the reliable and self-consistent determination of four independent film elastic constants and the mass density. In this way a mode-crossing which would have been very difficult to detect by other means was identified and could be handled properly. Finally the high precision experiment revealed limitations of the single layer hexagonal model for the investigated tungsten carbide film whose preparation is characterized by a high ion fluence and energy.

A comparative study of the elastic, compositional, and structural properties of tungsten carbide films as a function of their deposition parameters, also including the results presented in this article, are presently summarized for publication [5].

Financial support by the Deutsche Forschungsgemeinschaft is gratefully acknowledged.

References

[1] F. Nizzoli and J.R. Sandercock, in Dynamical Properties of Solids; Vol. **6**; The Modern Physics of Phonons: Transport, Surfaces and Simulations, edited by G.K. Horton and A.A. Maradudin (Elsevier, North Holland, Amsterdam, 1990), p. 281.

[2] J.D. Comins, in Handbook of Elastic Properties of Solids, Liquids, and Gases; Vol. **I**: Dynamic Methods for Measuring the Elastic Properties of Solids, edited by M. Levy, H.E. Bass, and R.R. Stern (Academic Press, 2001), p. Ch. 15, pp. 349-378.
[3] T. Wittkowski, G. Distler, K. Jung, B. Hillebrands, and J.D. Comins, Phys. Rev. B **69**, 205401-9 (2004).
[4] T. Wittkowski, G. Distler, K. Jung, B. Hillebrands, and J.D. Comins, Appl. Phys. Lett. **84**, 5356 (2004).
[5] T. Wittkowski, G. Distler, K. Jung, B. Hillebrands, and J.D. Comins, *Structural and Chemical Phase Transition in Tungsten Carbide Films Evidenced by Analysis of Their Stiffness Tensors*, to be submitted to J. Appl. Phys.
[6] G.W. Farnell and E.L. Adler, in Physical Acoustics; Vol. **9**, edited by W.P. Mason and R.N. Thurston (Academic Press, New York, 1972), p. 35-127.
[7] X. Zhang, J.D. Comins, A.G. Every, P.R. Stoddart, W. Pang, and T.E. Derry, Phys. Rev. B **58**, 13677 (1998).

6.19 Application of nanotechnology for manufacturing trephines with diamond-like cutting edges

L. Kleinen and B. Hillebrands[1]

Many diseases cause opacities to appear in the cornea, the normally transparent structures in the front of the eye. If the vision becomes blurred it is possible to remove the cloudy central part of the cornea and replace it with a corneal transplant (Fig. 1, right). During this keratoplasty the donor and recipient cornea are commonly prepared either by single-use or reusable metal trephines [1]. A trephine is a surgical instrument with a cylindrical blade used for cutting out a round piece of the cornea (trepanation) (Fig. 1, left). An alternative solution to this mechanical trepanation is the contactless trepanation with excimer or femtosecond laser systems which is more complicated and expensive and therefore less widespread. With 100,000 operations worldwide per year keratoplasties are the most frequently performed tissue transplantations [2]. In Germany up to 5,000 keratoplasties are performed annually [3] - most of them mechanically with trephines.

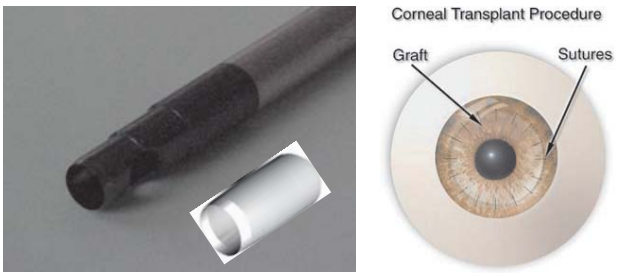

Fig. 1: Left: Photograph of a partly coated trephine and a schematized drawing of the trephine. Right: Drawing of the eye with a grafted cornea transplant (from http://www.eyemdlink.com).

Due to the surgical techniques as well as the configuration of metal trephine cutting edges irregular corneal surfaces may be induced. These lead to postoperative astigmatism. Contemporary manufacturing processes do enable the production of minimal cutting edge diameters ($0.4\,\mu m - 1\,\mu m$), however, this results in a reduced mechanical stability of such delicate cutting edges. It has been observed that the cutting edges of metal blades are immediately bent upon the first contact with tissue (Fig. 2, left). As a result, the cutting forces applied increase and the wound configuration is

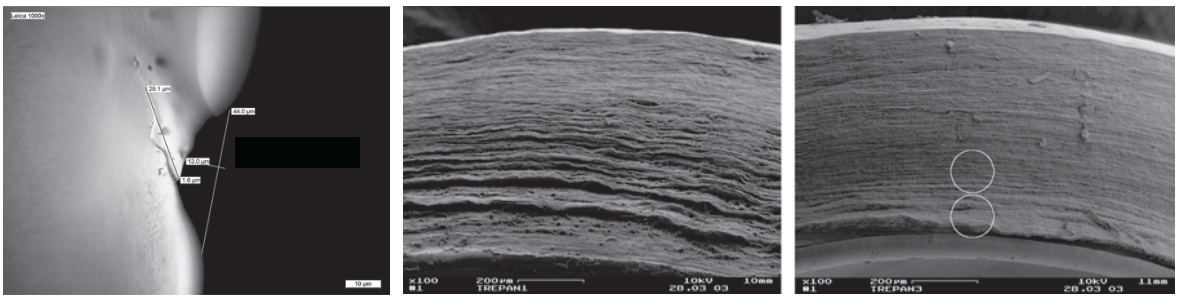

Fig. 2: Left: Damaged cutting edge of a single-use trephine. Middle: Irregular surface of a cornea cut with an untreated trephine. Right: Smooth surface of a cornea cut with a nanotechnologically refined trephine.

[1] In collaboration with H. Busch and U. Grabowy, NTTF GmbH Rheinbreitbach, and C. Lingenfelder, S. Kupferschmid and C.W. Spraul, Universitäts-Augenklinik Ulm.

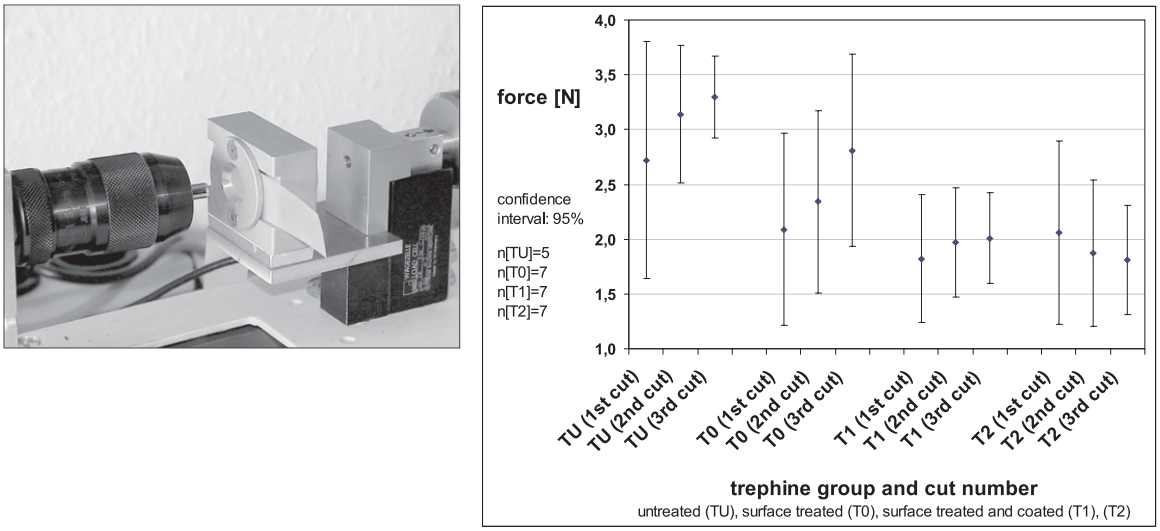

Fig. 3: Left: Measuring setup to quantify the forces when cutting a polyurethane foil (cornea model). Right: Results of the cutting force measurements. With each trephine from each group three cuts were performed. The nanotechnological refined trephines T0 (surface treated, sharpened, smoothed) and T1 and T2 (same as T0 but additionally coated with two different diamond-like thin carbon films) show a significant reduction in the cutting forces compared to the untreated ones T0.

negatively affected. Due to the complex geometry of trephine cutting edges, no diamond trephines are currently available. We are investigating the cutting performance of conventional trephines that were modified using nanotechnology [4].

Different metal trephines were characterized using a scanning electron microscope (SEM). The diameter of each cutting edge was measured. Pig corneas were studied histologically after trepanation. Selected trephines were *ion-forged* in a modified PVD (physical vapor deposition) reactor using highly accelerated ions which were concentrated by magnetic fields at low temperature. During this process the cutting edges of the blades were additionally sharpened and the surface of the trephines were smoothed and subsequently coated with a thin diamond-like wear protection film. The consecutive processing steps were controlled by SEM analysis of the cutting edge diameters. Randomly chosen areas of treated trephines were analyzed. After processing the trephines, pig corneas were cut and analyzed by histological and SEM examination. Additionally, the relevant mechanical cutting parameters of untreated as well as treated trephines were measured when penetrating into a polyurethane (PU) foil (Fig. 3, right).

Preliminary microscopic analysis already reveals differences in the quality of the cutting edges. The nanotechnological modification of the cutting edges does not result in larger diameters (Fig. 4). Compared with the initial cutting edges, the optical analysis of the modified trephine cutting edges reveals subjectively smoother surfaces.

The force measurements show reduction in the cutting forces for the treated trephines as compared to the untreated ones. The graph on the left side of Fig. 3 shows the average maximum measured force required to penetrate the PU foil. Four groups of trephines were tested. With each trephine three cuts were performed. On average the untreated trephines of the group TU showed an increase in the the applied force from 2.72 N for the first cut to 3.3 N for the third cut. The forces for all groups except the fourth (T2) increased with the number of cuts. Trephines with treated but uncoated surfaces of group T0 required significantly smaller (2.09 N to 2.81 N) forces to penetrate the PU foil. Trephines of groups T1 and T2 received an additional coating with different diamond-

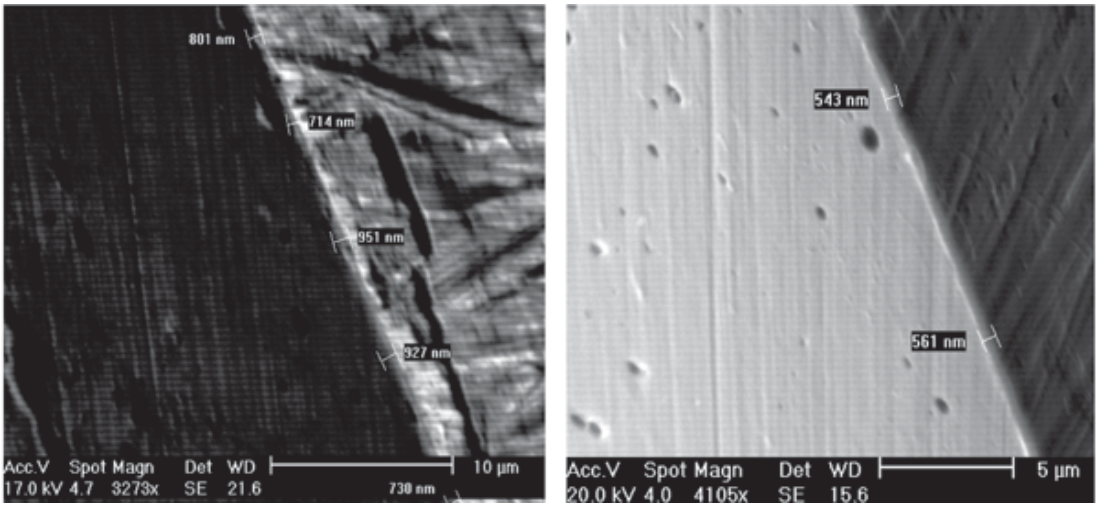

Fig. 4: SEM pictures of a reusable trephine's cutting edge. Left: the diameter of the uncoated blade (between 950 and 715 nm) and rough surface of the trephines sides are visible. Right: reduced diameter (550 nm) of the blade after nanotechnological treatment (sharpening, smoothing and coating of the blade).

like thin carbon films. For those trephines the forces for PU membrane penetration were again reduced to values between 1.82 N and 2.01 N for group T1 and 2.06 N to 1.81 N for group T2. Due to the different coating the forces used with trephines of group T2 decreased with each performed cut as opposed to all other groups.

The SEM analyses show a subjectively smoother surface for the corneas treated with the modified trephines, see Fig. 2, right. Histology reveals that the surfaces of the treated cornea do not exhibit a smooth and unidirectional structure (Fig. 5). This divergence became larger when untreated trephines were used. The untreated trephines caused divergencies between 30° and 40° with respect to the main cutting direction on the Descemet membrane side of the cornea and between 0° and 35° on the epithelial side. With the treated trephines the angles decreases on both sides of the cornea. We measured angles between 0° and 19° on the Descemet side and between 8° and 11° on the epithelial side of the cornea.

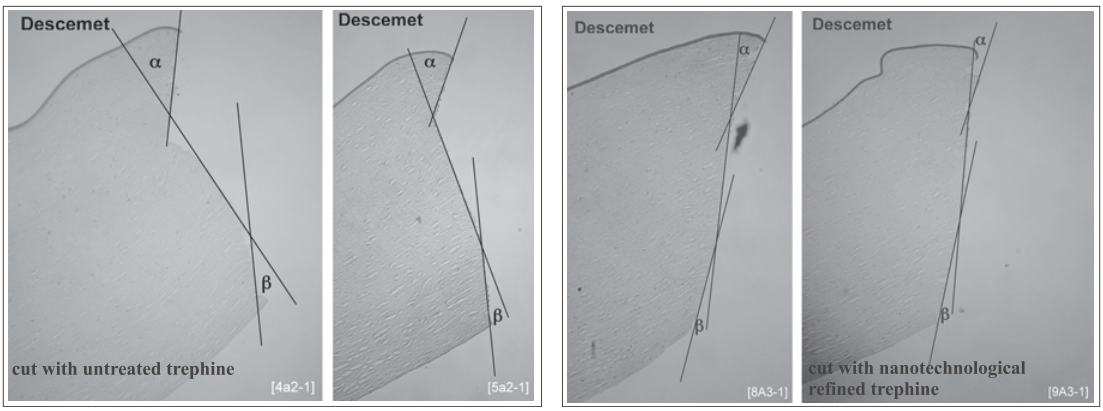

Fig. 5: The cut performance of the trephines is histologically determined by measuring the Descemet- (α) and endothelial- (β) shortening. The light microscopical pictures show sections through trepanated pig cornea. The smaller (α) and β) the better the cut performance of the trephine and the easier the grafting of the cornea transplant [5]. The untreated trephines cause larger angles than the nanotechnological refined trephines.

The results of the mechanical characterization of the treated trephines enable the development of harder and longer-lasting surfaces. Whereas uncoated trephines show a Rockwell hardness of 55 HRC (approximately 600 HV) the coated surfaces show a Vickers hardness of 1100 $HV_{.05}$.

The newly developed *ion-forging* of trephines in combination with nanostructured carbon coatings yield complex cutting edges of higher stability with diamond-like properties. This study shows that the performance quality of laser trepanation cannot be attained; however, the use of nanotechnology can further improve manual trephine techniques.

Financial support by the country Rheinland-Pfalz is gratefully acknowledged.

References

[1] U.G. Jähne, Diss., Univ. Halle (2004).
[2] A. Reis, T. Reinhard, R. Sundmacher, C. Braunstein, E. Godehardt , Br J Ophthalmol **82**, 700-703, (1998).
[3] R. Sundmacher, T. Reinhard, Der Ophthalmologe **98**, 273-276 (2001).
[4] C. Lingenfelder, S. Kupferschmid, U. Grabowy, L. Kleinen, C.W. Spraul, Klin Monatsbl Augenheilkd **222**, 709-716 (2005).
[5] J. Moisseiev, AM Intra-Ocular Implant Soc J **11**, 138-141, (1985).

Chapter 7: Publications

Most publications can be downloaded from http://www.physik.uni-kl.de/hillebrands.

7.1 published

1. *Surface acoustic waves for the characterization of BN-coated fibres observed by Brillouin light scattering*
   T. Wittkowski, K. Jung, B. Hillebrands, S. Stoeckel, K. Weise, G. Marx
   Anal. Bioanal. Chem. **379**, 594 (2004).

2. *The use of guided surface acoustic resonances in the determination of the thin film elastic tensor*
   T. Wittkowski, G. Distler, K. Jung, B. Hillebrands, J.D. Comins
   Appl. Phys. Lett. **84**, 5356 (2004).

3. *Brillouin light scattering spectroscopy*
   B. Hillebrands
   in: Novel techniques for characterizing magnetic materials, Yimey Zhu, editor,
   Kluwer Academic Press (2005).

4. *Magnetismus*
   B. Hillebrands, S. Blügel
   in: Bergmann-Schäfer, Experimentalphysik Band 6 (Festkörper)
   de Gruyters Verlag (2005).

5. *Modification of the magnetic properties of exchange coupled NiFe/FeMn films by Ga^+ ion irradiation*
   S. Blomeier, D. McGrouther, R. O'Neill, S. McVitie, J.N. Chapman, M.C. Weber,
   B. Hillebrands, J. Fassbender
   J. Magn. Magn. Mater. **290-291**, 731 (2005).

6. *Ion beam smoothing with low energy argon ions and reduction of Néel "orange peel" coupling in magnetic tunnel junctions*
   P.A. Beck, B.F.P. Roos, S.O. Demokritov, B. Hillebrands
   J. Magn. Magn. Mater. **290-291**, 1108 (2005).

7. *All-optical probe of magnetization dynamics in exchange biased bilayers on the picosecond timescale*
   M.C. Weber, H. Nembach, S. Blomeier, B. Hillebrands, R. Kaltofen, J. Schumann, M.J. Carey, J. Fassbender
   European Physical Journal B **45**, 243 (2005).

8. *Spin-wave excitations in finite rectangular elements*
   C. Bayer, J. Jorzick, B. Hillebrands, S.O. Demokritov, R. Kouba, R. Bozinoski, A.N. Slavin, K. Guslienko, D. Berkov, N. Gorn, M.P. Kostylev
   Phys. Rev. B **72**, 064427 (2005).

9. *Spin-wave eigenmodes of permalloy squares with closure domain structure*
K. Perzlmaier, M. Buess, C.H. Back, V.E. Demidov, B. Hillebrands, S.O. Demokritov
Phys. Rev. Lett. **94**, 057202 (2005).

10. *Structural analysis of ion irradiated polycrystalline NiFe/FeMn exchange bias systems*
S. Blomeier, D. McGrouther, S. McVitie, J.N. Chapman, M.C. Weber, B. Hillebrands, J. Fassbender
European Physical Journal B. **45**, 213 (2005).

11. *Real time temperature dynamics in exchanged biased bilayers upon laser excitation*
M.C. Weber, H. Nembach, B. Hillebrands, J. Fassbender
IEEE Trans. Magn. **41**, 1089 (2005).

12. *Ultrafast direct writing schemes for SAF MRAM cells in crossed-wire architecture with bipolar and unipolar field pulses*
H.T. Nembach, C. Bayer, M.C. Weber, P. Martin Pimentel, P.A. Beck, B. Leven, B. Hillebrands
Appl. Phys. Lett. **87**, 142503 (2005).

13. *Two-dimensional patterns of spin-wave radiation by rectangular spin-valve elements*
V.E. Demidov, S.O. Demokritov, B. Hillebrands, M. Laufenberg, P.P. Freitas
J. Appl. Phys. **97**, 10A717 (2005).

14. *Modified Gilbert damping due to exchange bias in NiFe/FeMn bilayers*
M.C. Weber, H. Nembach, B. Hillebrands, J. Fassbender
J. Appl. Phys. **97**, 10A701 (2005).

15. *Fe(001) on vicinal Au(001): Correlation of topography and magnetic surface anisotropy*
M. Rickart, T. Mewes, S.O. Demokritov, B. Hillebrands, M. Scheib
J. Phys. D: Appl. Phys. **38**, 1047 (2005).

16. *Evaluation of the quality of Permalloy gratings by diffracted magneto-optical spectroscopy*
R. Antos, J. Mistrik, T. Yamaguchi, S. Visnovsky, S.O. Demokritov, B. Hillebrands
Optics Express **13**, 4651 (2005).

17. *Evidence of native oxides on the capping and substrate of Permalloy gratings by magneto-optical spectroscopy in the zeroth and first diffraction orders*
R. Antos, J. Mistrik, T. Yamaguchi, S. Visnovsky, S.O. Demokritov, B. Hillebrands
Appl. Phys. lett. **86**, 231101 (2005).

18. *Process dependence of transport properties in phase-separated Pr0.7Pb0.3MnO3 single crystals*
R.W. Li, X. Zhou, B.G. Shen, B. Hillebrands
Phys. rev. B **71**, 092407 (2005).

19. *Analysis of the NiFe/FeMn exchange bias system with a varying Cu spacer thickness and position for partial decoupling*
M.O. Liedke, H.T. Nembach, B. Hillebrands, J. Fassbender
J. Magn. Magn. Mater. **290-291**, 588 (2005).

20. *Parametric generation of forward and phase-conjugated spin-wave bullets in magnetic films*
A.A. Serga, B. Hillebrands, S.O. Demokritov, A.N. Slavin, P. Wierzbicki, V. Vasyuchka, O. Dzyapko, A. Chumak
Phys. Rev. Lett. **94**, 167202 (2005).

21. *Spin-wave logical gates*
M.P. Kostylev, A.A. Serga, T. Schneider, B. Leven, B. Hillebrands
Appl. Phys. Lett. **87**, 142503 (2005).

22. *Phase shift of spin waves traveling through a 180° Bloch domain wall*
C. Bayer, H. Schultheiß, B. Hillebrands, R.L. Stamps
IEEE Trans. Magn. **41**, 10 (2005).

7.2 in press

1. *Magnetic patterning of Fe/Cr/Fe(001) trilayers by Ga+ ion irradiation*
S. Blomeier, B. Hillebrands, V.E. Demidov, S.O. Demokritov, B. Reuscher, A. Brodyanski, M. Kopnarski
J. Appl. Phys., in press.

2. *Spin-lattice relaxation phenomena in manganite LSMO thin films*
M.C. Weber, B. Hillebrands, V. Moshnyaga, K. Samwer
Europhys. Lett., in press.

3. *Real time evidence of two-magnon scattering in exchange coupled bilayers*
M.C. Weber, H.T. Nembach, B. Hillebrands, M.J. Carey, J. Fassbender
J. Appl. Phys., in press.

7.3 submitted

1. *All-optical probe of precessional magnetization dynamics in exchange biased NiFe/FeMn bilayers*
M.C. Weber, H.T. Nembach, B. Hillebrands, J. Fassbender
submitted to Phys. Rev. B.

Chapter 8: Conferences, Workshops, Schools, Seminars

(shown in chronological order with the speaker named)

8.1 Conferences

8.1.1 Invited talks

B. Hillebrands:
Tunneling of spin waves through a magnetic field inhomogeneity
Intermag Conference 2005, Nagoya, Japan, April 2005

A. Serga:
Storage and recovery of spin-wave signals in ferrites
Vth International Young Scientists Conference on Applied Physics, Kiew, Ukraine, June 2005

B. Hillebrands:
Propagation, tunneling and phase shift of spin waves at a magnetic field inhomogeneity
European Conference on Physics of Magnetism 2005, Posnan, Poland, June 2005

B. Hillebrands:
Spin dynamics in magnetic nanostructures
International Conference on Nanomaterials, Tamil Nadu, India, July 2005

B. Hillebrands:
Propagation and tunneling of spin waves through a magnetic field inhomogeneity
AVS 52nd International Symposium, Boston, U.S.A., October/November 2005

8.1.2 Contributed talks and posters

1 contribution:	EU-RTN NEXBIAS Projekttreffen, Technische Universität Kaiserslautern, Germany, February 2005
4 contributions:	EU-RTN ULTRASWITCH Projekttreffen, Erlangen, Germany, February 2005
11 contributions:	DPG-Frühjahrstagung Berlin, Germany, March 2005
2 contributions:	EU-STREP MAGLOG Projekttreffen, Bielefeld, Germany, March 2005
4 contributions:	Intermag Conference 2005, Nagoya, Japan, April 2005
1 contribution:	EU-RTN ULTRASWITCH Projekttreffen, Lisbon, Portugal, October 2005
2 contribution:	EU-RTN NEXBIAS Projekttreffen, Lisbon, Portugal, October 2005

8.2 Workshops

8.2.1 Invited talks

B. Hillebrands:
Quantized spin waves and spin wave propagation in inhomogeneously magnetized structures
1st meeting of NEDO International joint research, Homburg, Germany,
July 2005

8.2.2 Contributed talks and posters

V. Demidov:
Two dimensional patterns of spin-wave radiation by magnetic micro-rectangles
49th Annual Conference on Magnetism and Magnetic Materials, Jacksonville, USA, November 2004

S. Hermsdörfer:
Microwave assisted switching in $Ni_{81}Fe_{19}$ elements
"PhD- and Diploma students workshop" of the DFG SPP 1133 "Ultrafast magnetization processes", Göttingen, Germany, October 2005

H. Schultheiß:
Brillouin light scattering microscopy studies of mesoscopic magnetic rings
"PhD- and Diploma students workshop" of the DFG SPP 1133 "Ultrafast magnetization processes", Göttingen, Germany, October 2005

8.3 Invited colloquia and seminars

B. Leven:
Resistance behavior and magnetization reversal analysis of individual Co nanowires
Technische Universität Kaiserslautern, Germany, May 2005

B. Leven:
Magnetic nanostructures - From domain wall magnetoresistance to spin-wave logic
Technische Universität Kaiserslautern, Germany, June 2005

C. Bayer:
Spin-wave excitations in finite rectangular elements
Universität Hamburg, Germany, June 2005

8.4 IEEE-Magnetics Society Distinguished Lectures

In 2005 B. Hillebrands served for the IEEE-Magnetics Society as a Distinguished Lecturer to promote the science of magnetism as well as the goals of the Society. Annually the Society selects three Distinguished Lecturers.

The lecture was entitled: *Dynamics in magnetic micro- and nanostructures*.

The Lecture was given on invitation from local Chapters of the Magnetics Society and on invitation from universities and research laboratories.

List of Lectures:

11.04.2005	Kyoto University, Kyoto, Japan
14.04.2005	Tohoku University, Sendai, Japan
20.04.2005	IOP Headquarter, London, United Kingdom
17.05.2005	Santa Clara Valley Chapter, Komag, CA, USA
18.05.2005	Berkeley Laboratory, CA, USA
19.05.2005	Stanford University, CA, USA
20.05.2005	Hitachi Almaden, CA, USA
31.05.2005	University of York, United Kingdom
02.06.2005	Oxford University, United Kingdom
22.06.2005	Krakov University, Poland
23.06.2005	Poland Chapter, Czestochowa University, Poland
09.09.2005	Argonne National Laboratory, USA
12.09.2005	Simon Frazer University, Vancouver, Canada
14.09.2005	University of Colorado at Colorado Springs, CO, USA
15.09.2005	Bolder Chapter, NIST, Boulder, CO, USA
19.09.2005	Colorado State University, Fort Collins, CO USA
21.09.2005	MIT, Boston, MA, USA
21.09.2005	Massachusetts Chapter, MAXTOR, Shrewsbury, MA, USA
22.09.2005	Washington Chapter, George Washington University, Washington DC, USA
23.09.2005	NIST, Gaithersburg, MD, USA
26.09.2005	Seagate, Bloomington, MN, USA
26.09.2005	Minnesota Chapter, Minneapolis, MN, USA
27.09.2005	The Ohio State University, Columbus, OH, USA
29.09.2005	Pennsylvania Chapter, Seagate, Pittsburgh, PA, USA
30.09.2005	Carnegie Mellon University, PA, USA
28.10.2005	University of Alabama, Tuscaloosa, AL, USA

8.5 Contributions to other meetings

P.A. Beck:
Oberflächenglättung durch niederenergetischen Ionenbeschuss
BMBF Treffen Singulus, Kahl, Germany, November 2004

D. Hoffmann:
Brillouin light scattering spectroscopy on materials with high spin polarization: anisotropy, anisotropy dispersion and exchange constant
2nd International Symposium on New Materials with High Spin Polarization, February 2005

P.A. Beck:
Oberflächenmodifikation mittels ECWR-Quelle
BMBF Abschlusstreffen Singulus, Kahl, Germany, April 2005

Appendix: Impressions from 2005

Group Excursion

Glantal-Bahn

Summer 2005

Burkard Hillebrands IEEE Distinguished Lecturer Tour 2005

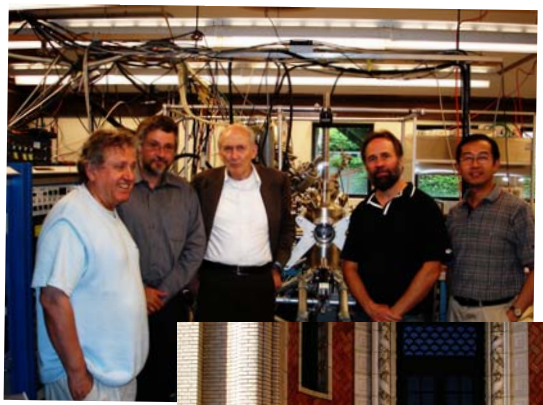

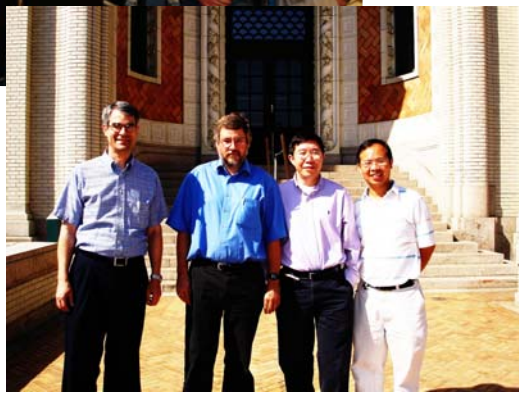

Finally: